AD NUMBER
ADB025624
LIMITATION CHANGES
TO: **Approved for public release; distribution is unlimited.**
FROM: **Distribution authorized to U.S. Gov't. agencies only; Test and Evaluation; 20 MAR 1978. Other requests shall be referred to Rome Air Development Center, Attn: ESM, Hanscom AFB, MA 01731.**
AUTHORITY
RADC ltr, 11 Mar 1982

AD B025624

AUTHORITY: RADC USAF
ltr, 14 MAR 82

RADC-TR-77-368 ✓
Final Technical Report
October 1977

(2)

AD B025624

RESEARCH ON MATERIALS FOR HIGH POWER LASER WINDOWS

Massachusetts Institute of Technology
Center for Materials Science and Engineering

Distribution limited to U.S. Government Agencies only; test and evaluation. Other requests for this document must be referred to RADC/ESM, Hanscom AFB, MA 01731.

20 MAR 1978

DDC
MAR 20 1978
E

FILE COPY

Sponsored by Defense Advanced Research Projects Agency (DOD) ARPA Order No. 2055

ROME AIR DEVELOPMENT CENTER
AIR FORCE SYSTEMS COMMAND
GRIFFISS AIR FORCE BASE, NEW YORK 13441

ARPA Order Number

2055

Contract Number

F19628-75-C-0191

Program Code Number

3 D 10

Principal Investigator

H. K. Bowen
(617) 253-6892

Name of Contractor

Massachusetts Institute
of Technology

RADC/ESM Project Scientist

Harold Posen
(617) 861-3532

Effective Date of Contract

1 June 1975

Contract Expiration Date

31 May 1977

Unclassified
SECURITY CLASSIFICATION OF THIS PAGE (When Date Entered)

(19) **REPORT DOCUMENTATION PAGE**

READ INSTRUCTIONS
BEFORE COMPLETING FORM

1. REPORT NUMBER
(18) RADC-TR-77-368 ✓

2. GOVT ACCESSION NO.

3. RECIPIENT'S CATALOG NUMBER

4. TITLE (and Subtitle)
(6) Research on Materials for High Power Laser Windows.

(9) 5. TYPE OF REPORT & PERIOD COVERED
Final Technical rept.
1 June [redacted]975 - 31 May 1977

6. PERFORMING ORG. REPORT NUMBER

7. AUTHOR(s)
(10) H. K. Bowen, R. M. Cannon, F. A. McClintock, J. B. Vander Sande

8. CONTRACT OR GRANT NUMBER(s)
(15) F19628-75-C-0191
ARPA Order-2055

9. PERFORMING ORGANIZATION NAME AND ADDRESS
Massachusetts Institute of Technology
Division of Sponsored Research
77 Mass. Ave., Camb., Mass. 02139

10. PROGRAM ELEMENT, PROJECT, TASK AREA & WORK UNIT NUMBERS
ARPA Order No. 2055
61101E 562003-08

11. CONTROLLING OFFICE NAME AND ADDRESS
Defense Advanced Research Project Agency
1400 Wilson Blvd.
Arlington, VA. 22209

(11) 12. REPORT DATE
Octe[redacted]77

13. NUMBER OF PAGES
192

14. MONITORING AGENCY NAME & ADDRESS (if different from Controlling Office)
Deputy for Electronic Technology (RADC/ESM)
Hanscom AFB, Mass. 01731

Monitor, Harold Posen/ESM

15. SECURITY CLASS. (of this report)
Unclassified (12) 194P.

15a. DECLASSIFICATION/DOWNGRADING SCHEDULE

16. DISTRIBUTION STATEMENT (of this Report)
Distribution limited to U.S. Government Agencies only; test and evaluation. Other requests for this document must be referred to RADC/ESM, Hanscom AFB, MA 01731. 20 MAR 1978

17. DISTRIBUTION STATEMENT (of the abstract entered in Block 20, if different from Report)
(16) 5620 (17) 03

18. SUPPLEMENTARY NOTES
Research was sponsored by Defense Advanced Research Projects Agency

ARPA Order No. 2055

19. KEY WORDS (Continue on reverse side if necessary and identify by block number)

Alkali Halides
Alkaline Earth Halides
Recrystallization
Crack Coalescence
Fracture
Fracture Statistics
Flaw Detection
Subgrains
Grain Boundary Migration
Solute Drag
KCl
CaF_2

20. ABSTRACT (Continue on reverse side if necessary and identify by block number)

The effects of aliovalent solutes on the grain boundary mobility of KCl and of oxides has been studied. The previously developed model for boundary mobility in KCl has been reformulated to include the effect of a strain energy interaction between the divalent solute ions and the boundary. Numerical calculations show that the solute ion and defect distributions, as well as the electrostatic field around a boundary are all affected.

DD FORM 1 JAN 73 1473 EDITION OF 1 NOV 65 IS OBSOLETE
S/N 0102-014-6601

Unclassified
SECURITY CLASSIFICATION OF THIS PAGE (When Data Entered)

JOB 220 050

The theory predicts the resulting boundary drag will increase in order for Ba^{+2}, Sr^{+2}, to Ca^{+2} solutes. A fluctuation mechanism by which a boundary can shed its solute cloud and move at intrinsic velocity has been analyzed to indicate the conditions under which this can occur and lead to more rapid rates of discontinuous recrystallization. A survey of grain boundary mobility data in oxides was made to indicate the relative importance of various controlling mechanisms.

CaF_2 single crystals of various orientations have been forged over a range of 0.46 to 0.92 T_m. Optical and TEM studies of the microstructure revealed that subgrain formation occurs over the entire temperature range investigated. At the lower temperatures the subgrain boundaries are not fully equilibrated and the microstructures are nonuniform and include deformation bands. Crystals forged in the <100> direction are more uniform and less prone to cracking than those forged in <111>. The subgrain size is inversely proportional to forging stress.

Models have been developed to calculate the effects of microcracking and crack coalescence on fracture statistics. The stresses for first cracking and for failure are determined. The grain boundary strengths are assumed to satisfy extreme-value statistics. For a typical distribution, the stress at first cracking is 50% higher for biaxial than uniaxial stress. The maximum stress is less size dependent than predicted from extreme-value statistics, and the biaxial and uniaxial strengths are less different. The presence of free surfaces do not strongly affect the fracture statistics. A variety of methods for determining flaw distributions and detecting flaws have been investigated. These include indentation tests, acoustical emission, and light scattering.

TABLE OF CONTENTS

A. INTRODUCTION

The objectives of this program have been to conduct research on processing and microstructure relations on materials suitable for infrared windows and to develop design procedures appropriate for these brittle materials. The program has been specifically concerned with producing high strength, forged alkali, or alkaline earth halides, or oxides and with characterizing the mechanical behavior and developing appropriate design, proof test or inspection techniques for these or other window materials.

Specific areas of research have included: a) investigation and characterization of the substructure formation during hot forging; b) determination of the effects of additives or impurities on grain boundary mobility; c) investigation into the causes and mechanisms of recrystallization or microstructural instabilities including the inhibiting effects of solutes; d) evaluation of the statistics of macrostrength as influenced by statistical variations in the strength of microstructural elements; e) develop flaw density curves for candidate materials; f) explore various methods of non-destructive evaluation suitable for finding small, sharp cracks of the type expected in brittle materials; h) consider design procedures incorporating statistical predictions, proof testing, and non-destructive evaluation as appropriate.

The work on grain boundary mobility focused primarily on further elaborating the solute drag effects and refining the theoretical models for solute drag and for the mechanism by which a moving boundary can breakaway from a solute cloud. The solute drag model was modified to include strain interactions between aliovalent solute ions and the boundary in addition to the primary electrostatic forces. The method by which a moving boundary can breakaway from its solute cloud was considered as this may be important during recrystallization of forged materials and also in breakaway of boundaries from pores or precipitates. This latter process is a particularly important problem during sintering of oxide materials to high density. Finally an extensive analysis of grain growth data in ceramics was performed to put into perspective the importance of solute drag relative to other mechanisms which can control boundary mobility in oxides.

Forging of CaF_2 was studied with particular emphasis on the substructure formation during hot forging. Crystals of various orientations were forged over a wide temperature range to find conditions under which crack free forgings could be accomplished and to investigate the subgrain formation, microstructural uniformity and extent of recrystallization. Extensive effort was devoted to microstructural examination using optical and electron microscopy.

The effort on designing with brittle materials focused on the problems of detecting flaws and developing flaw density curves and on the effect of microcrack coalescence on brittle fracture statistics. Analytic and numerical models were developed to evaluate the effects of microcrack coalescence on the size and principal stress effects on fracture statistics. These models also indicate the extent of precracking to be expected before failure. Several methods were evaluated for determining flaw distribution curves using non-destructive or destructive techniques. These results provide important elements for designing with brittle materials and for monitoring structural parts with acoustical emission to anticipate failure.

The research on this program has been performed by three research groups and has involved a significant contribution from students. Those who have contributed include Professors H. K. Bowen, R. M. Cannon, F. A. McClintock and J. B. Vander Sande, and research assistants P. T. Chiu, A. M. Glaeser,

P. J. Lemaire, H. J. Mayson, W. M. Sherry, and M. F. Yan. A. M. Glaeser was partially supported by a fellowship from the Fanny and John Hertz Foundation.

B. COUPLED SPACE CHARGE AND SIZE MISFIT CONTRIBUTIONS TO SOLUTE SEGREGATION.

B.1. Introduction:

Solute segregation near grain boundaries has been observed in ceramics as well as metals. Kingery (1974) and Gleiter and Chalmers (1972) have extensively reviewed the driving forces for the segregation phenomena. The major factors leading to equilibrium segregation in ceramics are probably the electrostatic potential associated with a grain boundary, and the reduction in strain energy of solute ions at and near a grain boundary, Kingery (1974). However, since the strain field affects the distribution of one of the charged species and therefore the charge density in the space charge region near the grain boundary, the electrostatic potential and the strain field are coupled. The coupling between these two interaction potentials also leads to coupling of the differential segregations of the aliovalent dopants of the same valence but with a different degree of size misfit with the matrix ions.

In a moving grain boundary, the models of Cahn (1962) and Lucke and Stuwe (1962) for the solute drag depend strongly on the detailed form of the interaction forces. Thus such coupling can be expected to affect the solute drag.
This section treats the equilibrium interaction forces and

solute distributions. Applications to the case of a moving boundary will follow in section C.

B.2. Theory:

The existence of space charge regions near lattice discontinuities (free surfaces, dislocations and grain boundaries) in an ionic solid was first postulated by Frenkel (1946); the charge distributions have been formulated by Frenkel (1946), Lehovec (1953), Eshelby, et al. (1958) and Kliewer and Koehler (1965). The potential difference between the surface and the bulk leads to a nonuniform distribution of aliovalent solute ions in a region which typically extends 2-20 lattice spacings in from the surface.

Gibbs showed that solute elements which decrease the surface energy should concentrate at the surface. Many other thermodynamic approaches after Gibbs have been reported. In particular, McLean (1951) showed that for an impurity with an adsorption free energy, F_a, and a bulk concentration, C_∞, the solute concentration at the boundary, C_b, is given as

$$C_b = \frac{C_\infty \exp(-F_a/kT)}{1 + C_\infty \exp(-\frac{F_a}{kT})} \qquad (1)$$

For a solute ion which has a size misfit in the matrix the adsorption free energy can arise from the partial reduction of the strain energy for an atom segregated to the already distorted boundary regions. Furthermore, due to the spatial dependence of the lattice distortion in the grain boundary region, the adsorption free energy is likely to have a certain spatial dependence. However, the details of the spatial dependence are related to the grain boundary structure and are not known with precision. The range of the strain field normal to the boundary likely corresponds to the periodicity of the structural units in the coincidence model of the grain boundary structure and is about several lattice constants, Chalmers and Gleiter (1971). The maximum magnitude of the strain energy, U_o, can be approximately estimated from the size misfit, Δr, of the solute ion, Young's modulus, Y, and Poisson's ratio, ν, as given by Lucke and Stuwe (1962) as

$$U_o = \frac{4\pi Y r^3 \eta^2}{(1 + \nu)} \qquad (2)$$

where $\eta \equiv \frac{\Delta r}{r}$ and r is the radius of the lattice ions of the sublattice in which the solute ion is substitutionally located.

In an ionic solid, the strain field interaction between a grain boundary and solute ions affects the charge distributions and therefore the electrostatic potential distribution in the grain boundary region. For illustrative purposes, we analyze the impurity segregation of divalent cations, I, e.g., Sr^{2+}, Ca^{2+}, Ba^{2+} in the grain boundary region of an ionic solid, e.g., KCl.

We use the approach of minimizing the free energy of the crystal including the lattice defects and solute ions and the interaction between the charged species and the grain boundary, following Kliewer and Koehler (1965). In formulating the free energy of the system of defects within a distance, L, from a grain boundary, we include the strain field and the electrostatic interaction energies between the defects and the grain boundary. For generality, we assume strain interaction energies, $U_s^i(x)$, between the defects (vacancies, vacancy pairs, vacancy-solute pairs, and unassociated solute ions) and the grain boundary. In particular, we assume that the strain interaction energy, $U_s^f(x)$, between the unassociated divalent cation dopant, I, and the grain boundary has the functional form,

$$U(x)^f = \begin{cases} U_o \left(1 - \left(\frac{x}{2a}\right)^n\right) \text{eV} & x \leq 2a \\ 0 \text{ eV} & X > 2a \end{cases} \qquad (3)$$

where a is the lattice constant of the matrix, and a choice of the index, n, affects the detail of the strain function. The range of strain field energy is chosen as two lattice constants and is within the periodicity of the structural units in the coincidence grain boundary model, Chalmers and Gleiter (1971). For specific calculations the magnitudes of U_o are chosen as ± 0.2 eV and ± 0.05 eV. A strain energy, U_o, of -0.2 eV is probably appropriate for Ca^{2+} and -0.05 eV for Sr^{2+} in KCl.

Furthermore, we assume that a certain binding energy is required for an excess quantity of the divalent cation, I, and the matrix ions, K and Cl, to be associated within the grain boundary core. This binding energy, similar to the delta function discussed in Lifshitz et al. (1965) can also be a function of the particular grain boundary.

The free energy, F, in a system with number densities of $n_+(x)$ cation vacancies, $n_-(x)$ anion vacancies, $n_B(x)$ vacancy complexes, $n_f(x)$ unassociated solutes and $n_{ib}(x)$ associated vacancy-solute complexes, can be expressed as

$$F = \int_0^L dx[n_+(F^+ + U_s^+) + n_-(F^- + U_s^-) + n_B(F^+ + F^- - B + U_s^B) + n_f U_s^f + n_{ib}(F^+ - B_+ + U_s^b) + \frac{1}{2}\rho\phi] - TS_c + \frac{1}{2}\sigma\phi_1 + N_s^f F_s^f + N_s^+ F_s^+ + N_s^- F_s^- \qquad (4)$$

where F^+ and F^- are the formation energies of the cation and anion vacancies respectively; B and B_+ are the binding energies of the vacancy complexes, $(V_K' - V_{Cl}^{\bullet})^*$, and the vacancy-impurity complexes, $(I_K^{\bullet} - V_K')^*$, respectively; $\frac{1}{2}\rho\phi$ is the electrostatic energy term for the charge density, ρ, with the space charge potential, ϕ; S_c is the configurational entropy of the system but excluding that in the boundary core; $\frac{1}{2}\sigma\phi_1$ is the electrostatic energy term for the boundary core with a "surface" charge density, σ, and a "surface" potential, ϕ_1; N_s^f, N_s^+ and N_s^- are the number per unit area of the unassociated I, K and Cl ions respectively in the boundary core with their respective binding energies F_s^f, F_s^+ and F_s^-; and U_s^+, U_s^-, U_s^B, U_s^f, U_s^b are the strain field interaction energies between the grain boundary and the unassociated cation vacancies, unassociated anion vacancies, cation-anion vacancy pairs, unassociated solute ions and solute-vacancy complexes.

The charged species in the crystal are related by Poisson's equation,

$$\frac{d^2\phi}{dx^2} = -\frac{4\pi}{\varepsilon}\rho = -\frac{4\pi e}{\varepsilon}(n_f + n_- - n_+) \qquad (5)$$

where e is the magnitude of an electronic charge, and ε the permittivity.

The free energy, F, must be minimized while subjected to the constraints of Poisson's equation and the conditions of electrical neutrality requiring the charge per unit area on the boundary, σ, to be

$$\sigma = -e\int_o^L (n_f + n_- - n_+)\, dx \qquad (6)$$

and that the unassociated I ions in the boundary core and in the boundary region are conserved,

$$N_s^f + \int_o^L n_f\, dx = \text{constant} \qquad (7)$$

and that the excess matrix ions in the core are compensated by the vacancies in the crystal,

$$N_s^+ - N_s^- = \int_0^L [n_+(x) - n_-(x)]\, dx \tag{8}$$

These constraints are somewhat more restrictive than necessary, but allow solutions which contain the important elements of the problem.

After the minimization of the free energy, F, with these constraints we obtain

$$\frac{n_+}{N} = \exp -\left(\frac{F^+ + U_s^+ + F_s^+ - e\phi}{kT}\right) \tag{9}$$

$$\frac{n_-}{N} = \exp -\left(\frac{F^- + U_s^- + F_s^- + e\phi}{kT}\right) \tag{10}$$

$$\frac{n_f}{N} = \exp -\left(\frac{U_s^f - F_s^f + e\phi + \alpha_H}{kT}\right)$$

$$= (1 - p_\infty)C_\infty \exp -\left(\frac{e\phi - e\phi_\infty + U_s^f(x) - U_s^f(\infty)}{kT}\right) \tag{11}$$

$$\frac{n_{ib}}{N} = 12 \exp -\left(\frac{F^+ - B_+ + U_s^b + \alpha_H}{kT}\right)$$

$$= C_\infty p_\infty \exp -\left(\frac{U_s^b(x) - U_s^b(\infty)}{kT}\right) \tag{12}$$

where N is the density of cation sites and α_H is the Langrange multiplier which is determined from the condition that the total number of impurity ions must be conserved, C_∞ is the total impurity concentration in the bulk and p_∞ is the fraction of these associated.

The bulk potential, $e\phi_\infty$, can be determined from the electrical neutrality condition in the bulk,

$$n_+(\infty) = n_-(\infty) + n_f(\infty),$$

$$\exp - \left(\frac{F^+ + U_s^+(\infty) + F_s^+ - e\phi_\infty}{kT} \right) =$$

$$\exp - \left(\frac{F^- + U_s^-(\infty) + F_s^- + e\phi_\infty}{kT} \right) + (1 - p_\infty)\, C_\infty \tag{13}$$

With the assumption that U_s^+ and U_s^- have no spatial dependence, the Poisson's equation can be reduced to

$$\frac{d^2 z}{ds^2} = \frac{1}{2} \left\{ e^{z} - e^{-z} \left[e^{-[U_s^f(x) - U_s^f(\infty)]/kT} \left(1 - \frac{n_-(\infty)}{n_+(\infty)}\right) + \frac{n_-(\infty)}{n_+(\infty)} \right] \right\}$$

$$\simeq \frac{1}{2} \left[e^{z} - e^{-[U_s^f(x) - U_s^f(\infty)]/kT}\, e^{-z} \right] \tag{14}$$

where

$$z \equiv (e\phi - e\phi_\infty)/kT \tag{15}$$

$$s \equiv x/\delta \tag{16}$$

and

$$\delta \equiv \left[\frac{8\pi \ Ne^2}{\varepsilon kT} \ \exp\left(\frac{e\phi\infty - (F^+ + U_s^+ + F_s^+)}{kT}\right)\right]^{-1/2} = \left[\frac{8\pi Ne^2 n_+(\infty)}{\varepsilon kT}\right]^{-1/2} \qquad (17)$$

and the approximation holds in the extrinsic temperatures where, $n_-(\infty)/n_+(\infty) << 1$.

Numerical integrations were performed to solve Poisson's equation, Eq. (14), for the strain field of the functional form, Eq. (3) and for the total impurity concentration of 50 ppm molar. The values of defect formation and association energy used for these calculations are listed in Table I.

At temperatures above the isoelectric point, the I ions are electrostatically repelled from the postively charged grain boundary. An attractive strain field, $U_o < 0$, counter-balances the electrostatic space charge effect and increases the space charge potential in the charge cloud. However, a repulsive strain field, $U_o > 0$, decreases the space charge potential to a more negative value, Figs. B1 and B2.

At temperatures below the isoelectric point, which is about 444°C for this impurity concentration level, the attractive space charge potential is complemented by an attractive strain field such that the potential near the boundary may exceed the bulk potential, Figs. B3 and B4. As seen from Eq. (13) and the Figs. B1 - B4 the value of $e\phi_\infty$ is not affected by the strain interactions; this is to be expected physically.

The distribution profiles of the K vacancies and the I

TABLE I

Data of KCl Vacancy Formation Energies, and Solute-Vacancy Binding Energies.

Quantity	Enthalpy (eV)	Entropy (k)
K-vacancy formation energy[1]	0.84	3.2
Cl-vacancy formation energy[1]	1.38	3.2
Schottky defect formation energy[2]	2.49	7.64
I-solute K vacancy binding energy[2]	0.57	1.88

1. Dreyfus and Nowick (1962).
2. Fuller, et al. (1968).

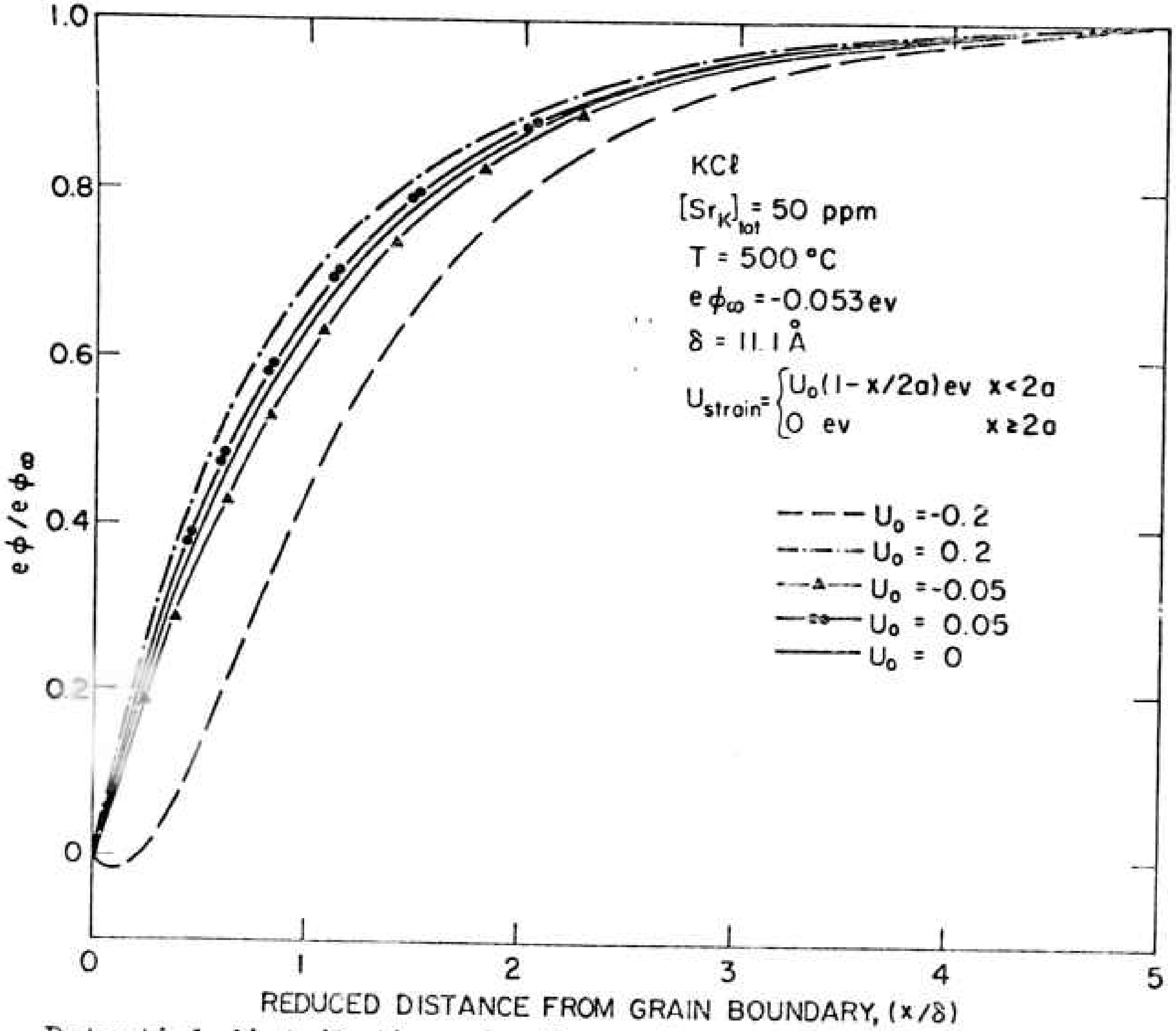

Fig. B1 Potential distributions in the grain boundary region due to the coupled effects of the electrostatic space charge and the mechanical strain field interactions at 500°C ($>T_0$).

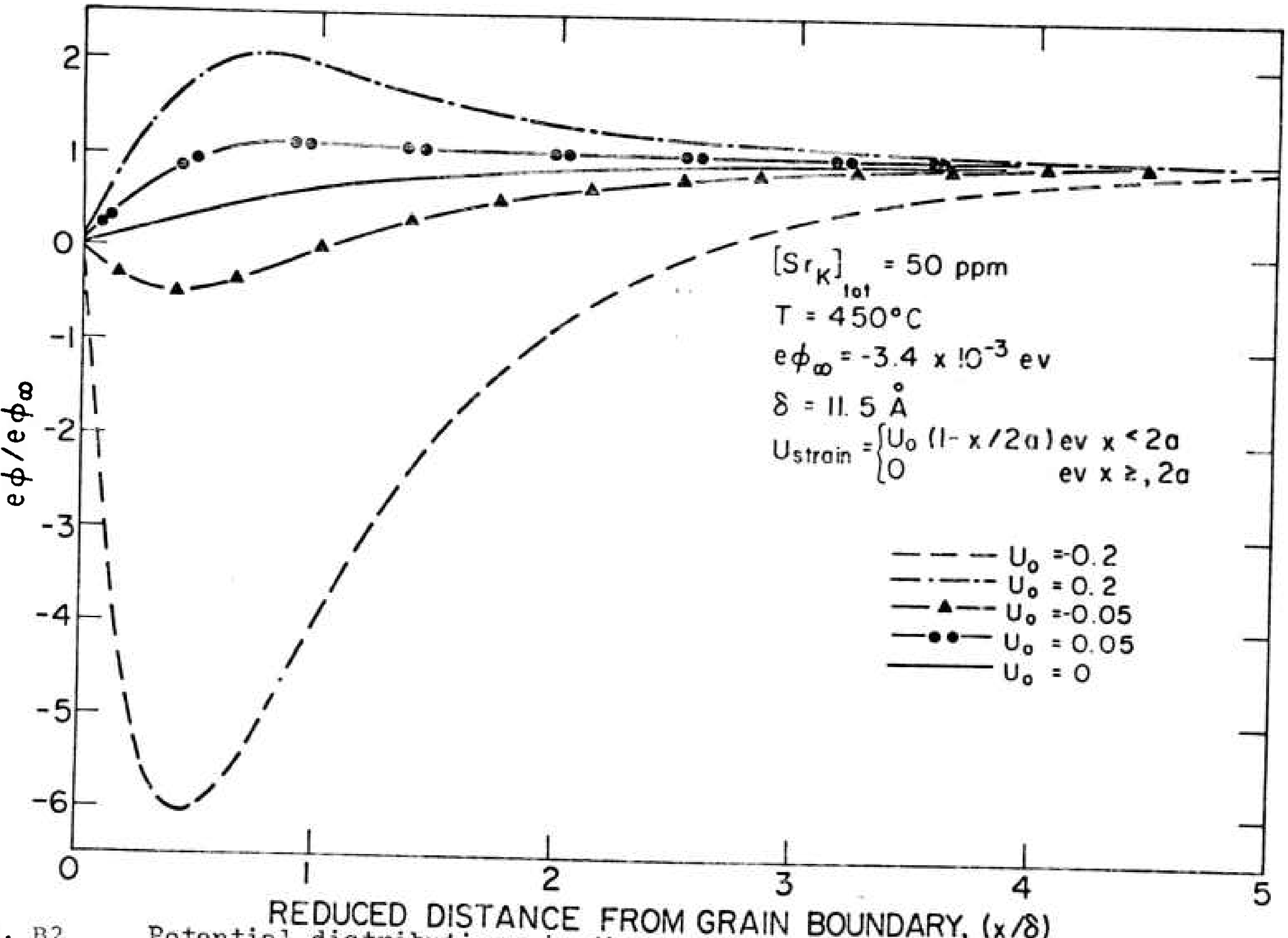

Fig. B2 Potential distributions in the grain boundary region due to the coupled effects of the electrostatic space charge and the mechanical strain field interactions at 450°C (≳ T_o).

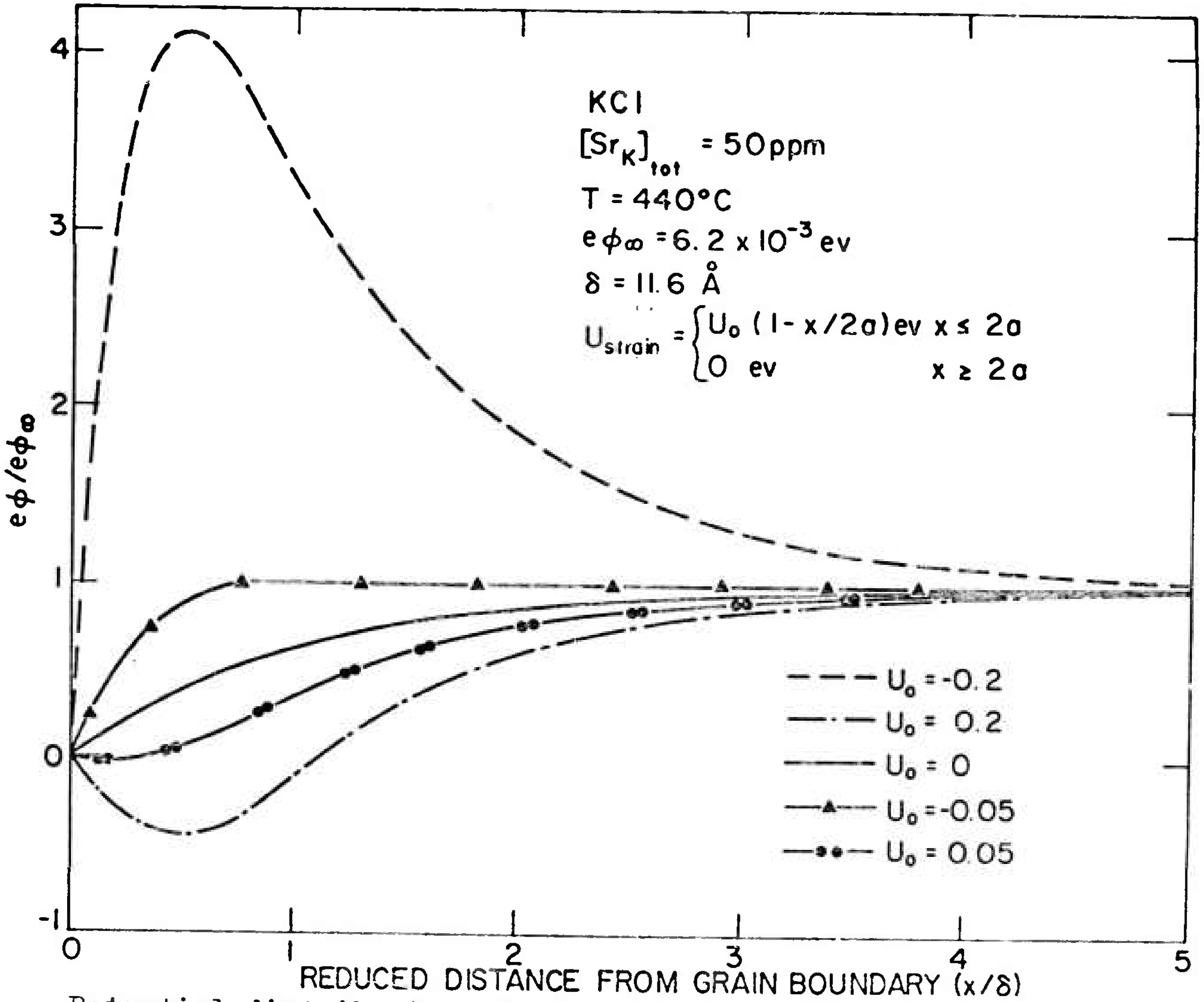

Fig. B3 Potential distributions in the grain boundary region due to the coupled effects of the electrostatic space charge and the mechanical strain field interactions at 440°C ($\lesssim T_o$)

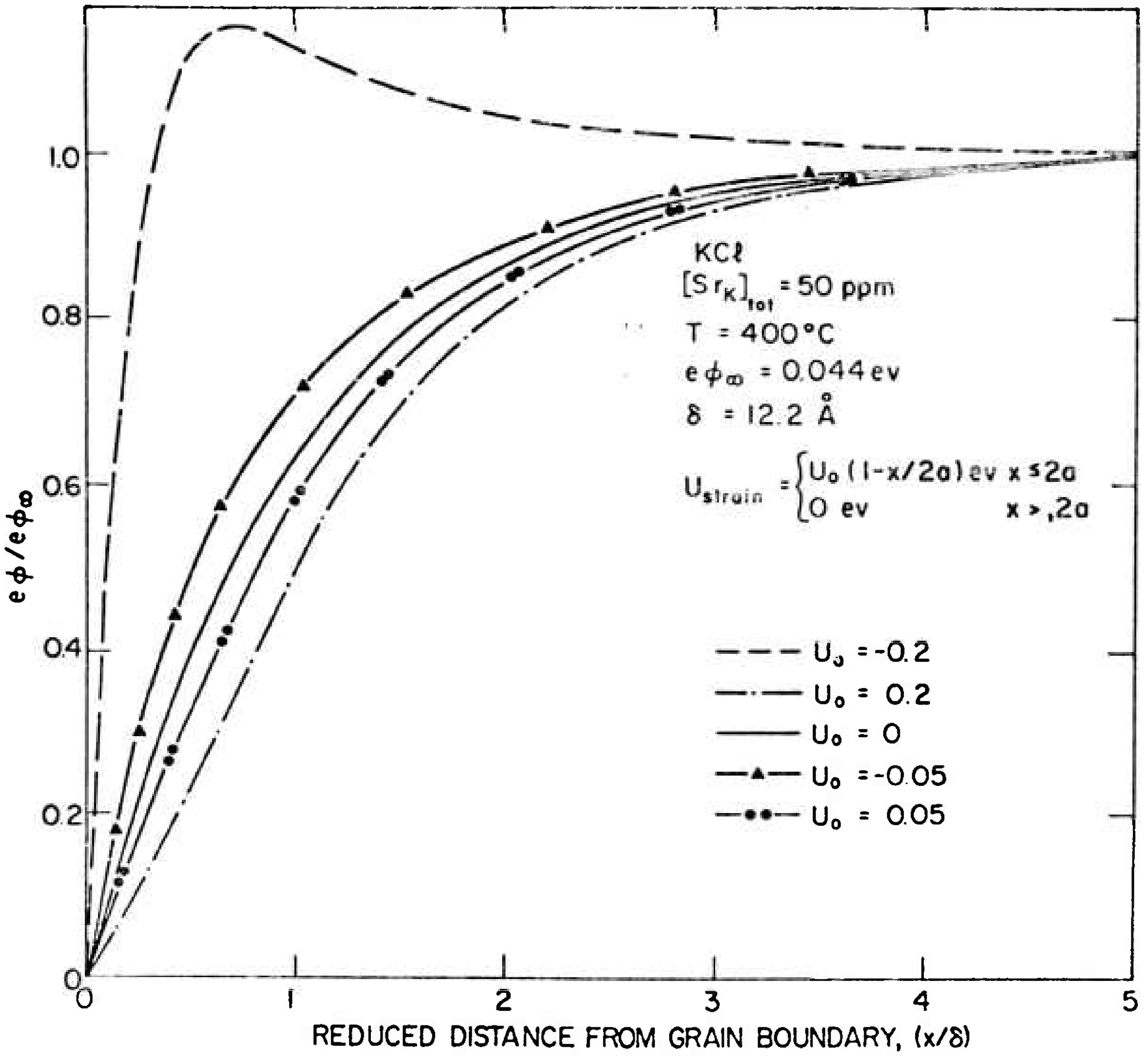

Fig. B4 Potential distributions in the grain boundary region due to the coupled effects of the electrostatic space charge and the mechanical strain field interactions at 400°C (< T_o).

ions in the grain boundary region, for an attractive impurity strain field, $U = -0.2\text{eV}$, are shown in Fig. B5. At the location where the concentration of K vacancies and I ions are equal, there is no net charge density (with Cl vacancies neglected); and this location corresponds to the inflection point, $\partial^2\phi/\partial x^2 = 0$, in the potential distributions shown in Figs. B1-B4. The segregation of I ions within two lattice spacings of the grain boundary is due in large part to the attractive strain field. Beyond the range of the strain field interaction, the space charge potential is repulsive to I ions even at 400°C, Fig. B5.

Several functional forms of the strain field interaction energy are assigned by the designation of $n = 2$, 1, and 1/4 in eq. (3). Due to the coupling with the strain field, the electrostatic space charge potential distributions are different for different strain functions. The distributions of the charged species due to the coupled effects of the electrostatic space charge potential and the different strain functions are shown in Fig. B6 for a temperature just above the iso-electric temperature, 444°C.

For the case of a sample with two divalent cation solutes of the same ionic charge but with different ionic radii, Poisson's equation, Eq. (14), in the grain boundary regions becomes

$$\frac{d^2z}{ds^2} = \frac{1}{2}\left\{e^{z} - e^{-z}\left[(1-A)e^{-\frac{U_1(x)-U_1(\infty)}{kT}} + Ae^{-\frac{U_2(x)-U_2(\infty)}{kT}}\right]\right\} \quad (18)$$

where U_1 denotes the strain energy function of solute 1 and U_2 of solute 2; and A is the fraction of the total unassociated

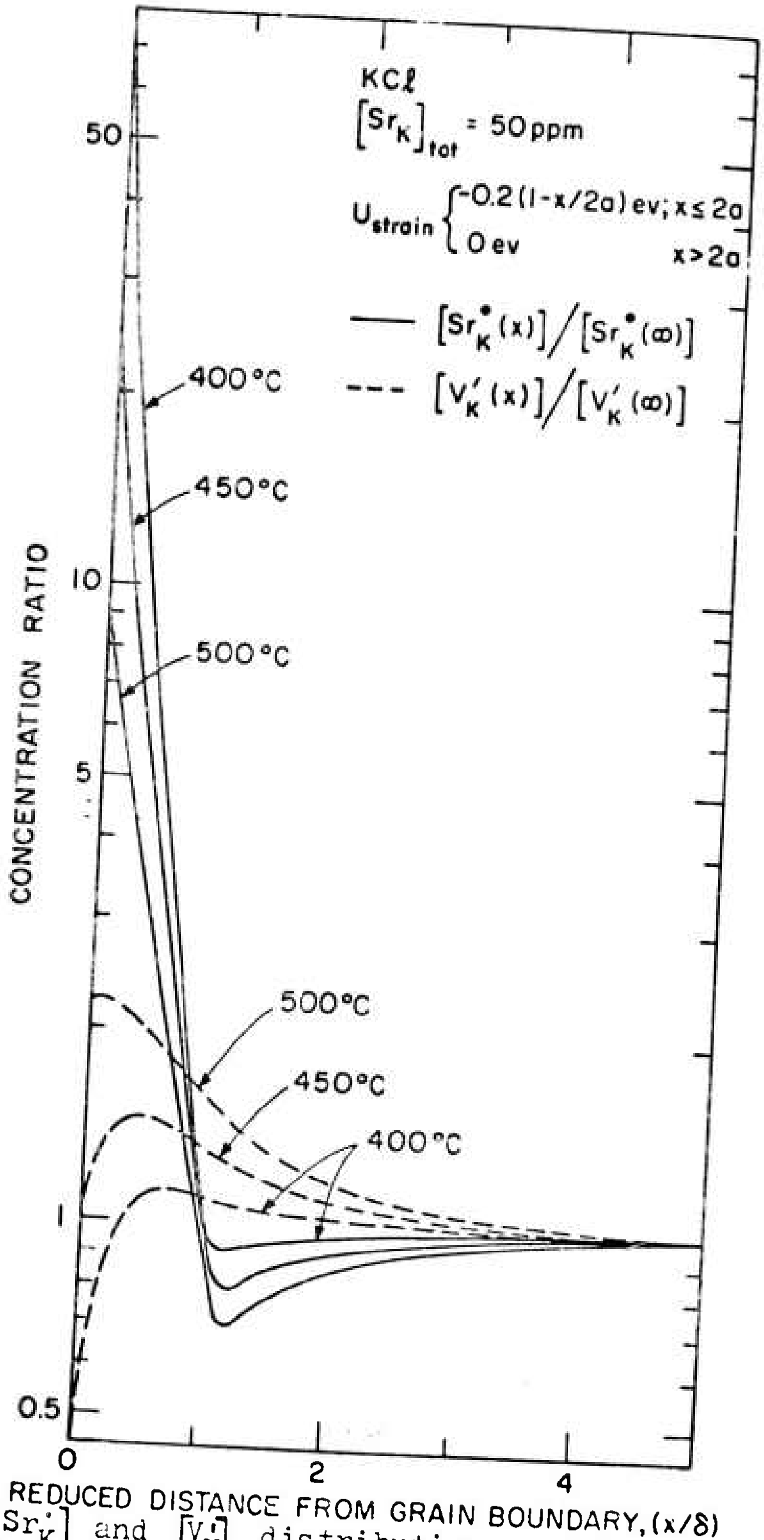

Fig. B5 $[Sr_K^{\cdot}]$ and $[V_K^{'}]$ distribution profiles, under the coupled effects of the electrostatic and the mechanical strain interactions in the grain boundary region of 50 ppm Sr doped KCl.

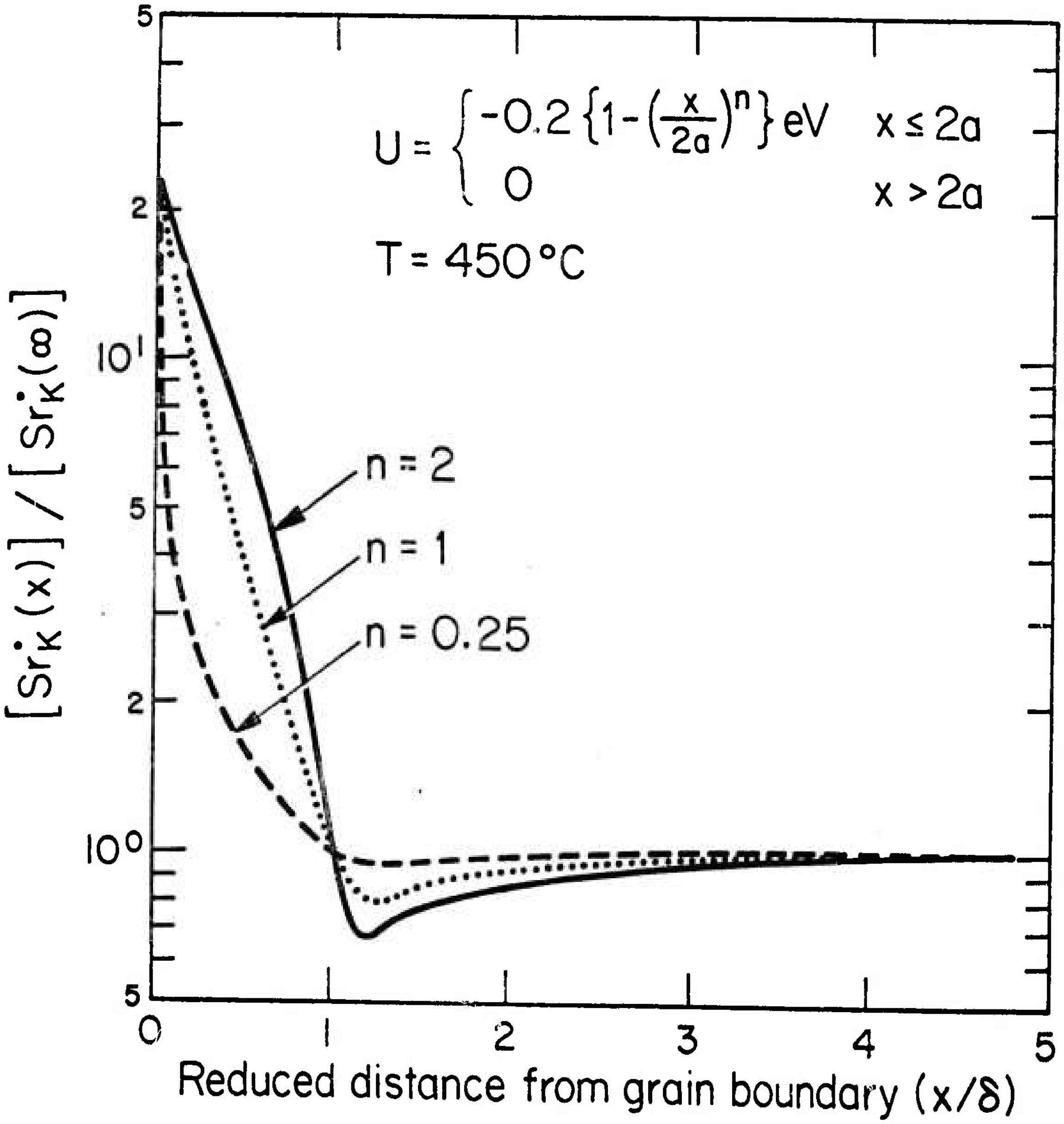

Fig. B6. Calculated values of the solute distribution near the grain boundary for three different assumed forms of the strain field interaction energy.

divalent cation which is solute 2. In the limit of a negligible amount of dopant 2, the Poisson's equation is reduced to Eq. (14).

For the case where the ion with the greater misfit is the smaller fraction of total impurity, Fig. B7 shows the concentrations of the impurities calculated from Eq. (18) and the expressions for the unassociated solute densities, n_{f1} and n_{f2} for solutes 1 and 2 respectively, are

$$\frac{n_{f1}(x)}{N} = (1 - A)C_\infty(1 - p_\infty)e^{-\left(\frac{e\varphi - e\phi_\infty}{kT}\right)} e^{-\left(\frac{U_1(x) - U_1(\infty)}{kT}\right)} \qquad (19)$$

$$\frac{n_{f2}(x)}{N} = AC_\infty(1 - p_\infty)e^{-\left(\frac{e\phi - e\phi_\infty}{kT}\right)} e^{-\left(\frac{U_2(x) - U_2(\infty)}{kT}\right)} \qquad (20)$$

where the impurity-vacancy binding energy and the probability of association are assumed to be identical for solutes 1 and 2.

B.3. Discussion:

(1) A coupling between the electrostatic potential and the mechanical strain interaction between an aliovalent solute and the grain boundary is shown to exist and to induce a non-uniform distribution of the solutes and the electrostatic potential in the grain boundary region.

(2) The coupling is visibly strong at temperatures close to the isoelectric temperature where the electrostatic

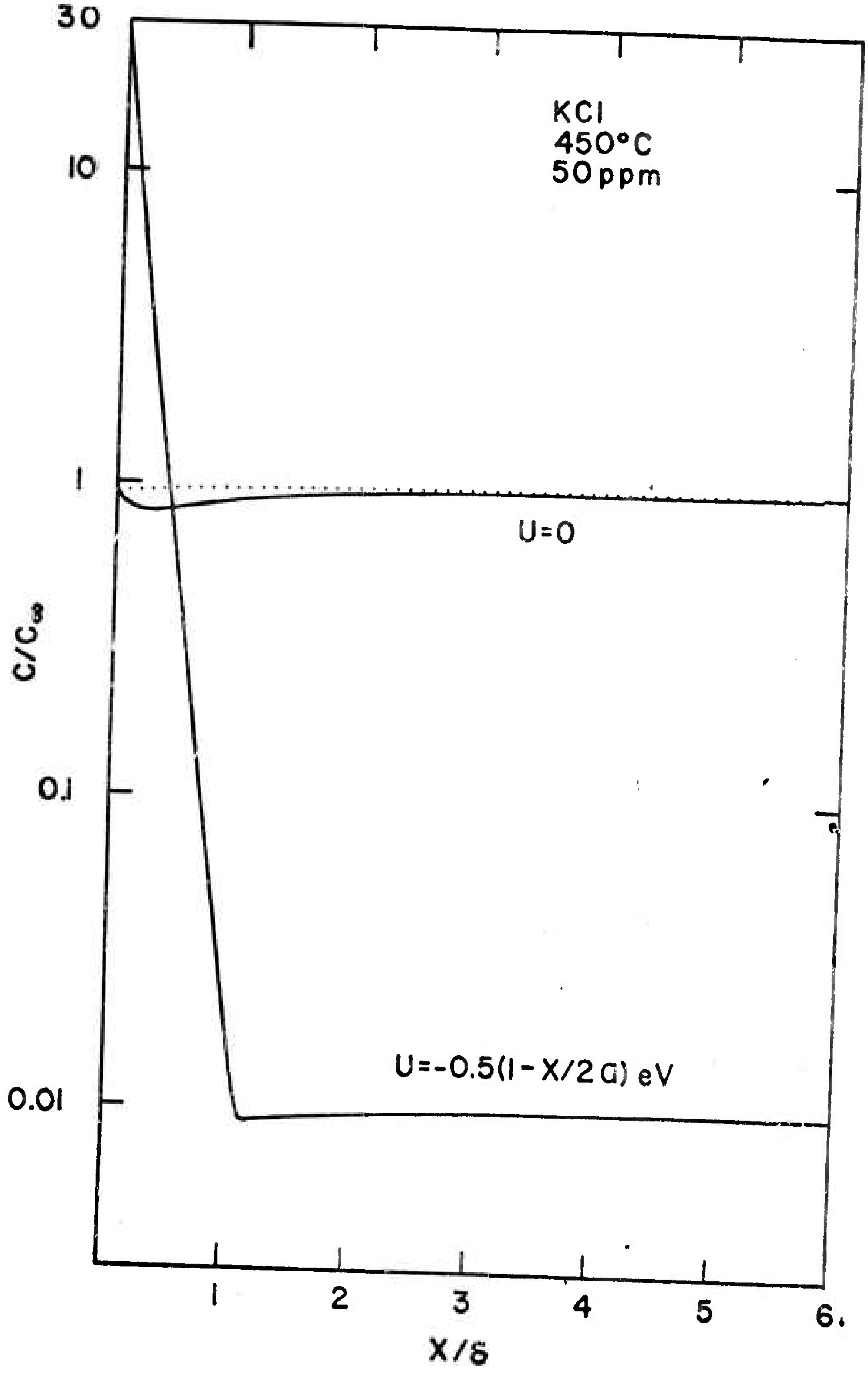

Figure B7. Coupling effect on the distribution of two divalent solute cations. The majority solute (49 ppm) is assumed to have no strain interactions; the minority solute (1 ppm) has a very strong interaction. The dotted line shows the solute distribution calculated from space charge theory for 50 ppm strain free solute ions.

potential is small. Under these conditions the electric fields will be much stronger than in the strain free case, and both the potentials and fields may reverse their sign within the charge cloud.

(3) The choice of the functional forms of the strain field potential is rather arbitrary. However, the magnitudes of U_o are chosen in that they are reasonable values for Sr and Ca dopants in a KCl matrix. The range of the strain field are chosen as two lattice spacings, and this corresponds to the periodicity of the structural units in the coincidence model of the grain boundary structure.

(4) The solute profile in the grain boundary region is more sensitive to the functional form of the strain field at temperatures close to the isoelectric point.

(5) If the strain interaction goes to zero at infinity, the bulk potential, $e\phi_\infty$, and the isoelectric temperature are unaffected by the strain interaction and are the same as for the purely electrostatic case.

(6) Although the binding energies for the defects in the boundary core are included in the initial formation they do not affect the results in an important way without making additional restrictive assumptions about the surface or boundaries. As discussed by Lifshitz et al, the F_s terms must be functions of the particular boundary; in the absence of such specific information, if the F_s terms are taken as constants they have no interesting effect and the quantities $(F^i + F_s^i)$ become the defect creation energies used by others.

(7) Similarly the binding energy of cations to the core does not affect the spatial distribution of potential, cations

or vacancies near the boundary except indirectly through the affect on the bulk concentration, C_∞. This effect on C_∞ is negligible if L is large. At high concentrations and low temperatures when the impurity concentration at the boundary core becomes high enough to saturate the available sites, then a more explicit effect would be anticipated which would be evident if the surface were treated as having a finite number of sites in the analysis.

(8) The analysis of the free energy minimization implicity assumes a continuous charge distribution. Although this is probably not correct as pointed out in Whitworth, (1972, 1975) the resulting errors do not obscure the present results regarding the effects of strain interactions on segregation.

B.4. References:

Cahn, J.W. (1962), Acta. Met., 10, 789.

Chalmers, B. and Gleiter, H. (1971), Phil. Mag. 24, 1541.

Dreyfus, R.W., and Nowick, A.S., (1962), J. Appl. Phys. Suppl. 33, 473.

Eshelby, J.D., Newey, C.W.A., Pratt, P.L. and Lidiard, A.B., (1958), Phil. Mag. 8, 75.

Frenkel, J., (1946), "Kinetic Theory of Liquids", Oxford U. Press, N.Y.

Fuller, R.G., Marquardt, C.L., Reilly, M.H. and Wells, J.C., Jr. (1968), Phys. Rev. 176, 1036.

Gleiter, H. and Chalmers, B. (1972), "High Angle Grain Boundaries", Prog. in Mat. Sci., Vol. 16, eds. B. Chalmers et. al., Pergamon Press.

Kingery, W. D., (1974), J. Am. Ceram. Soc. 57, 1 and 57, 74.

Kliewer, K. L. and Koehler, J. S., (1965), Phys. Rev. 140A (4) , 1226.

Lehovec, K. (1953), J. Chem. Phys. 21, 1123.

Lifshitz, I. M., and Geguzin, Ya. E., (1965), Sov. Phys.-Sol. St., 7, 44.

Lucke, K. and Stuwe, H. P. (1962), "On the Theory of Grain Boundary Motion", in Recovery and Recrystallization of Metals, ed., L. Himmel, Interscience/AIME.

McLean, D. (1951), "Grain Boundaries in Metals", Clarendon Press.

Whitworth, R. W. (1972), Phys. Stat. Sol. (b), 54, 537.

Whitworth, R. W. (1975), Adv. in Phys., 3, 203.

C. SOLUTE DRAG THEORY FOR GRAIN BOUNDARY MIGRATION IN KCl.

C.1. Introduction:

Alkali halides are appreciably strengthened by the deformation structure which forms during hot forging. These microstructures are comprised of low angle subgrains, typically of a size of 10μm or less, eg., Cannon et al. (1976), Yan et al. (1975a,c). In pure materials these forged crystals were found to be susceptible to strength degradation caused by recrystallization and growth of grains of the order of 1 mm in size during stress relief anneals and even at room temperature, eg., Koepke et al. (1974). The additions of solutes, particularly divalent cations, were found to be effective in inhibiting this undesirable recrystallization. Although the effects of solutes on nucleation are still not understood, the inhibition of recrystallization is apparently due, at least in part, to the reduction in grain boundary mobility caused by the additives, Yan et al. (1975a,b,c), Cannon et al. (1976).

In the impurity drag theories of Cahn (1962), Lucke and Stuwe (1962), the nature of the interactions between the impurity atoms and the grain boundary is an important feature. For grain boundary migration in metals, the interaction energy has generally been assumed to be a mechanical or strain field interaction. However, the experimental results in ionic solids, showed that aliovalent cation solutes have a much stronger effect than monovalent solutes in retarding the grain boundary migration, Yan et al. (1975C). Yan (1976). Further, the space charge theories showed that ionic crystal interfaces at thermal equilibrium with the bulk crystal are electrostatically charged.

Consequently, we proposed that the impurity-boundary interaction energy is mainly due to the electrostatic interactions between the space charge cloud and the moving grain boundary. A theory was developed on the previous program for the solute drag caused by divalent cations in KCl; it was based exclusively on electrostatic interactions. The theory was an extension of the equilibrium space charge theory, and allowed calculations of the mobility based upon experimentally determined values of solute diffusivities and other defect energies and mobilities, Yan et al. (1975C). The only parameter in this idealized theory which is not sufficiently well known is the difference in energy for a cation vacancy located at a boundary compared to one in the lattice.

In the case of a monovalent dopant, the strain field interaction, rather than the space charge potential, is more likely to be the dominant interaction potential between the dopant and the grain boundary. It is generally agreed that the strain field interaction potential originates from the size mismatch between the dopant and the matrix ions, Lucke and Stuwe (1962). However, for an aliovalent dopant with a significant ionic size mismatch with the matrix ion in the same sublattice, both the strain field and the electrostatic interactions are significant. The strain field interaction energy affects the distribution of the charged solute ions and therefore, the electrostatic potential and defect distribution in the grain boundary region. In section B, we analyse the coupled effects of the strain field and the electrostatic interactions on the solute and space charge distribution.

This section includes two extensions of the grain boundary mobility model. First we incorporate the strain field interaction into the solute drag theory. This is of particular importance at temperatures near the isoelectric temperature where the electrostatic forces become low enough that the solute cloud may not remain attached to the boundary in the absence of a strain field interaction. Secondly we consider the mechanism by which a moving boundary can breakaway from the solute cloud and move at high velocity. It had been previously suggested that this is an important step in the discontinuous recrystallization observed at low temperatures in KCl, Yan et al. (1975a), Cannon et al. (1976).

C.2. Calculation of Solute Drag:

The solute drag force can be calculated from the asymmetric solute distribution about the boundary at a given velocity. The solute profiles are determined by solution of the flux equation; this requires explicit expression of the vacancy concentrations near the boundary in order to calculate the diffusivity. Considering only electrostatic effects the solute diffusivity can be expressed as, Yan et al. (1975b), Yan (1976).

$$D^s(x) = D_o p(x) = \frac{D_o p_\infty}{p_\infty + (1-p_\infty)\exp(-\frac{e\phi(x) - e\phi_\infty}{kT})} \qquad (1)$$

where D_o is the diffusion coefficient of the associated vacancy-solute complexes, and p(x) is the probability of association near the boundary

$$p(x) = \frac{p_\infty}{p_\infty + (1-p_\infty)\exp(-\frac{e\phi(x) - e\phi_\infty}{kT})} \qquad (2)$$

The electrostatic field, ϕ, has the value ϕ_∞ in the bulk. The concentration of vacancy-solute complexes in the bulk is $C_\infty p_\infty$, where C_∞ is the nominal solute concentration.

Such calculations were preformed previously; however, it is computationally simpler to evaluate the solute drag from an approximate expression, which is constructed from Taylor's expansions of the integral form of the drag force at the high or low velocity limits, Cahn (1962).

Consequently, the total drag force, F, experienced by a moving grain boundary with velocity, V, can be approximated as

$$F = \frac{V}{M_o} + \frac{\alpha\ C_\infty V}{1+\beta^2 V^2} \tag{3}$$

where M_o is the intrinsic boundary mobility, α^{-1} is the mobility per unit impurity concentration in the solute controlled low velocity region; and β^{-1} is the drift velocity of the impurity atoms across the grain boundary and it is also the boundary velocity at which the impurity drag reaches the maximum. Furthermore, as shown in Cahn (1962), the quantities α and β are related to the impurity-boundary interaction energy, U(x), and the impurity diffusivity, D(x), as

$$\alpha = 4NkT \int_{-\infty}^{\infty} \frac{\sinh^2 U(x)/2kT}{D(x)}\, dx \tag{4}$$

$$\frac{\alpha}{\beta^2} = \frac{N}{kT} \int_{-\infty}^{\infty} \left(\frac{dU}{dx}\right)^2 \cdot D(x)\ dx \tag{5}$$

where N is the number of cations per unit volume, and we take

$$U(x) = e\phi(x) - e\phi_\infty \tag{6}$$

This procedure can be directly modified to include the strain interaction energy by using

$$U(x) = (e\phi - e\phi_\infty) + U_{strain} \tag{7}$$

$$D(x) = \frac{D_o p_\infty}{p_\infty + (1-p_\infty)\exp\left(-\frac{e\phi - e\phi_\infty + U_{strain}}{kT}\right)} \tag{8}$$

where the electrostatic potential is modified by the strain interaction as discussed in section B.

Calculations of α and β^{-1} have been done for strain functions of the form.

$$U_s = \begin{cases} U_o \quad (1 - (x/2a)^n) & x \leq 2a \\ 0 & x > 2a \end{cases} \tag{9}$$

where a is the lattice parameter, n determines the rate of decrease of the strain interaction energy in moving away from the boundary a distance x. The maximum interaction force U_o is calculated from the elastic strain energy for a sphere with a radius difference Δr compared to the host ion:

$$U_o = -\frac{4\pi E r^3}{(1+\nu)} \left(\frac{\Delta r}{r}\right)^2 \tag{10}$$

where E is the elastic modulus, and ν is Poisson's ratio. Using typical values for KCl with a Ca^{+2}, Sr^{+2}, or Ba^{+2} dopant gives values of U_o of -0.2, -0.05, and -10^{-4}eV respectively.

Plots of α and β^{-1} are shown in Figs. (C1) and (C2). These were calculated for n = 1, and $U_o = \pm 0.2$, and ± 0.05. The values for $U_o = +\ 0.2$ and $+\ 0.05$ are less likely to be physical (i.e., a strain energy interaction will always be attractive, $U_o < 0$) but were included for completeness. At temperatures near the isoelectric point the drag parameter, α, does not vanish for a finite strain field of either sign, Fig.(C1). The strain field interaction tends to decrease the breakaway velocities, β^{-1}, over most of the temperature range.

Since the drag forces must be balanced by the driving force in order to maintain a steady state boundary motion, Eq. (3), presents a cubic equation of the boundary velocity for a given driving force. The solutions of boundary

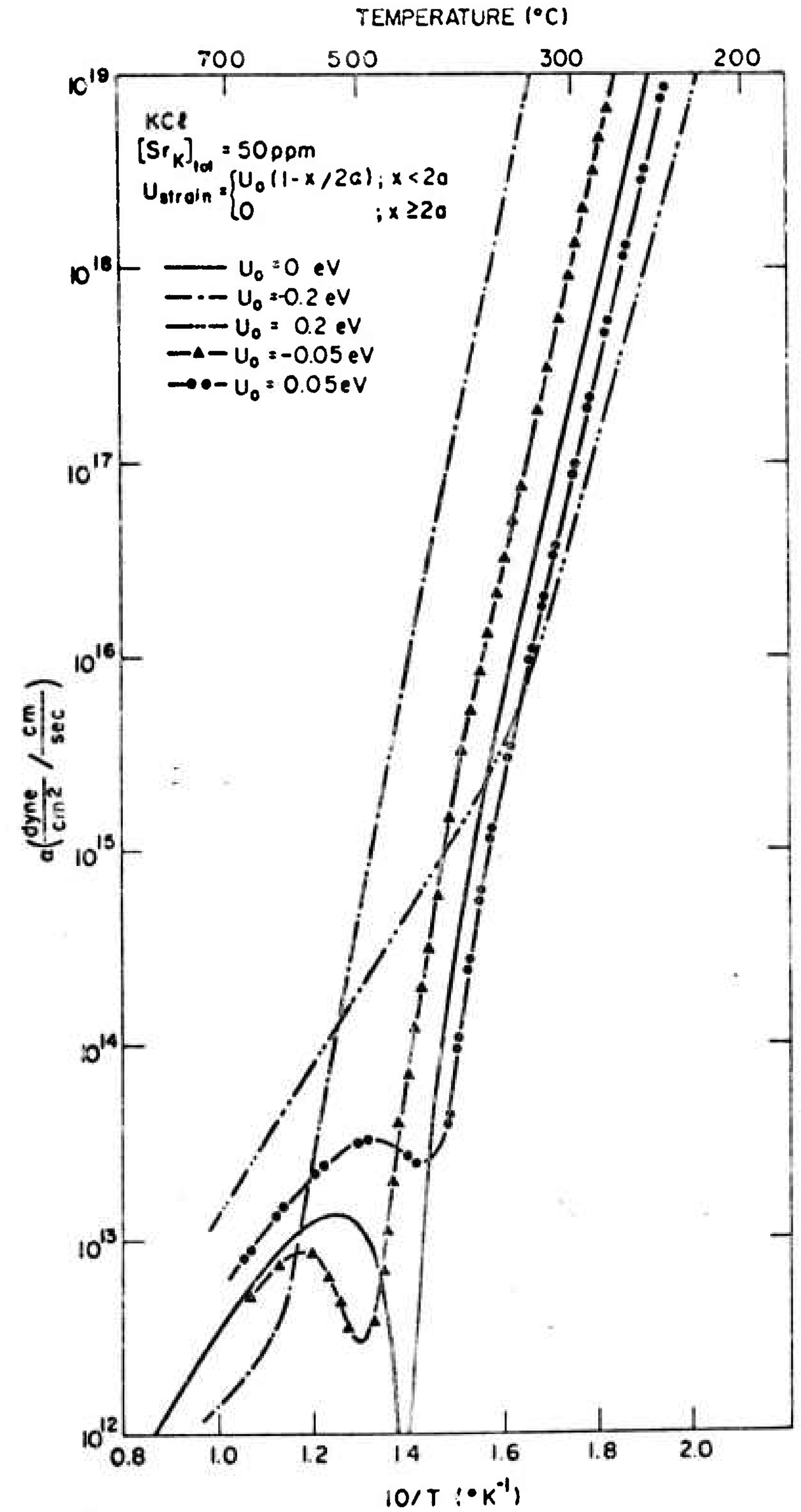

Figure C1. Calculated values of α, the drag force per unit velocity, per unit dopant concentration on a moving grain boundary, considering the coupled interactions of the electrostatic and mechanical strain fields.

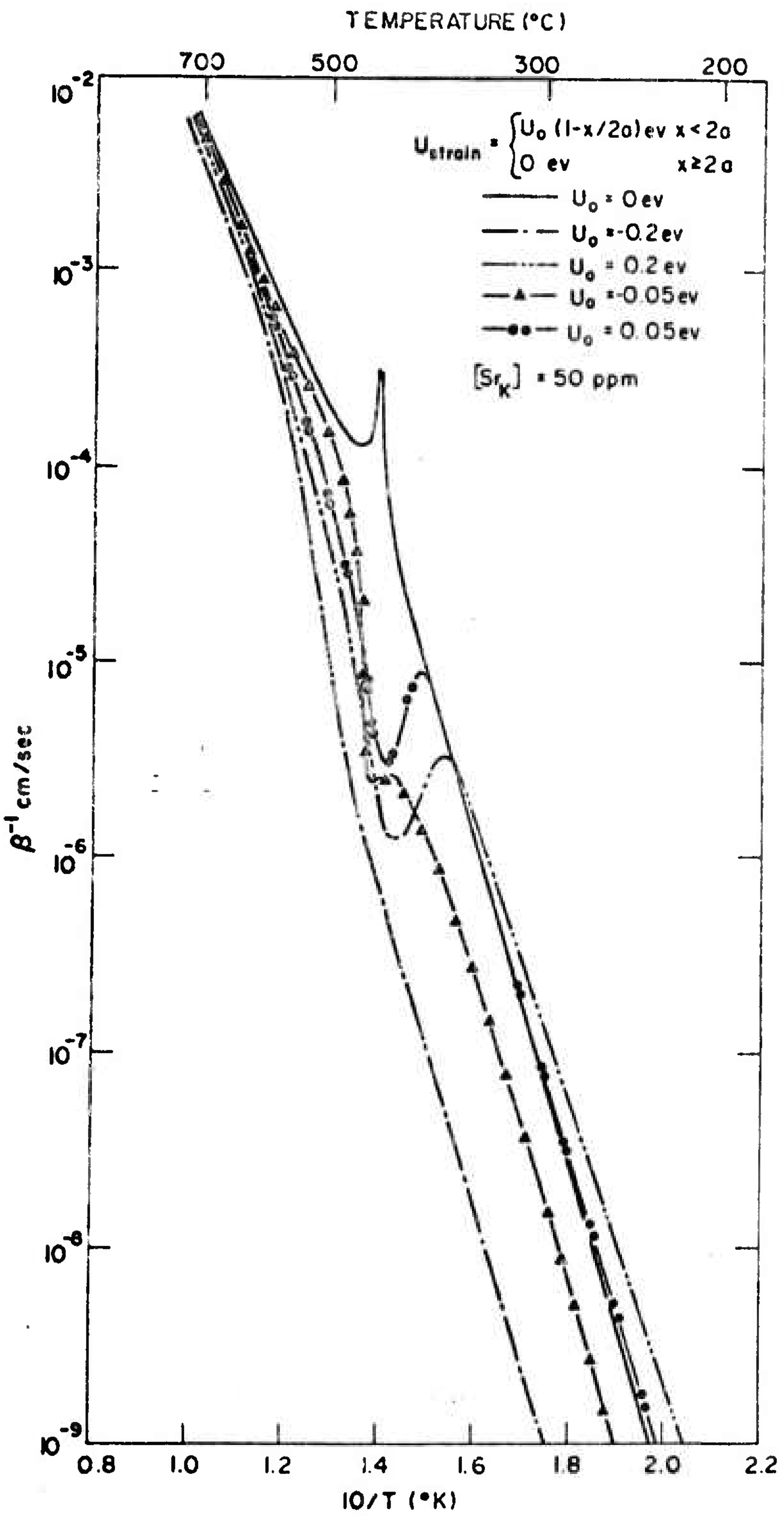

Figure C2. Calculated values of β^{-1}, the breakaway velocity of a grain boundary from the associated solute cloud. Both the electrostatic and mechanical strain interactions are included.

velocities under a driving force of 10^5 dynes/cm^2, which corresponds to an average of 7.3μm for the linear grain size intercepts, are shown in Figs. (C3) and (C4). Mobility calculations alternatively assuming $n = 1$ and $n = 2$ are shown in Fig. (C3); the purely electrostatic case is shown for comparison in Fig. (C4). The values of defect diffusivities and association energies, and of M_O were those previously used, Yan et al. (1975b), Yan (1976). The experimental data for similar Sr concentration, 50 ppm, and driving force are also shown.

It can be seen that away from the isoelectric temperature, the effect of the coupled strain field is relatively small, but near the isoelectric temperature the calculated mobility is substantially modified. For the assumed value of $n = 1$, the general shape of the curves is similar. There is a region in which the driving force exceeds the drag force so that the boundary would move at the intrinsic velocity in this temperature range. For the purely electrostatic interaction, the temperature range for this high velocity behavior is centered about the isoelectric. For the coupled case with $n = 1$, the temperature range for a single high velocity solution is smaller and further it is displaced to a higher temperature range rather than being centered around the isoelectric temperature. If a repulsive force, $U_O > 0$, is used the gap in the low velocity drag curves shifts to lower temperatures and is centered below the isoelectric. For the $n = 2$ assumption the detailed form of the velocity curve is changed; the cause for this is not presently understood. However for this case the maximum in the velocity is also shifted to a temperature higher than the isoelectric. Where a low velocity solution does exist it is very similar for both assumptions.

The formulation of the expression for α and α/β^2, Eqs. (4) and (5) were based on the assumption that the solute-boundary interaction energy U is independent of velocity.

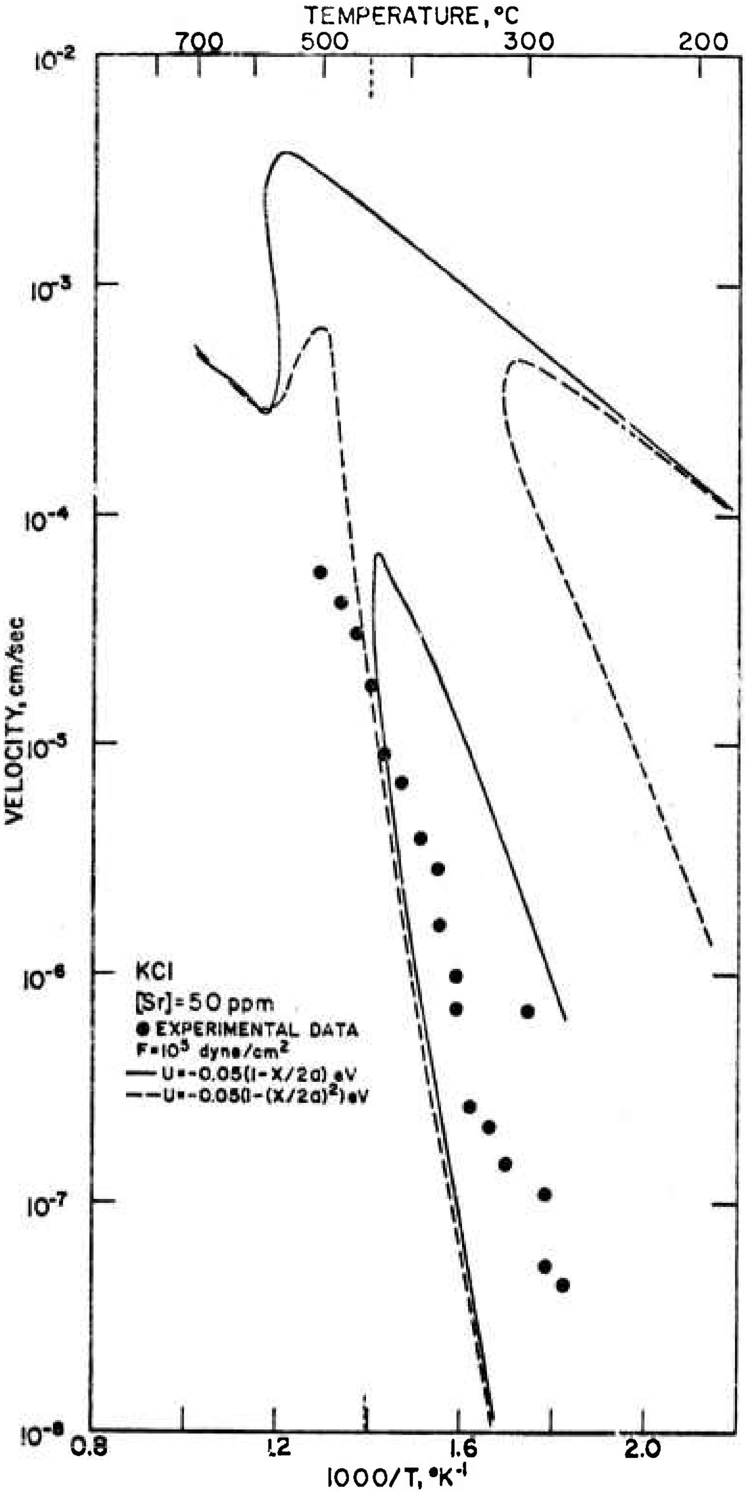

Figure C3. Calculated grain boundary mobility for Sr doped KCl where a strain field interaction force is included in addition to the electrostatic effects.

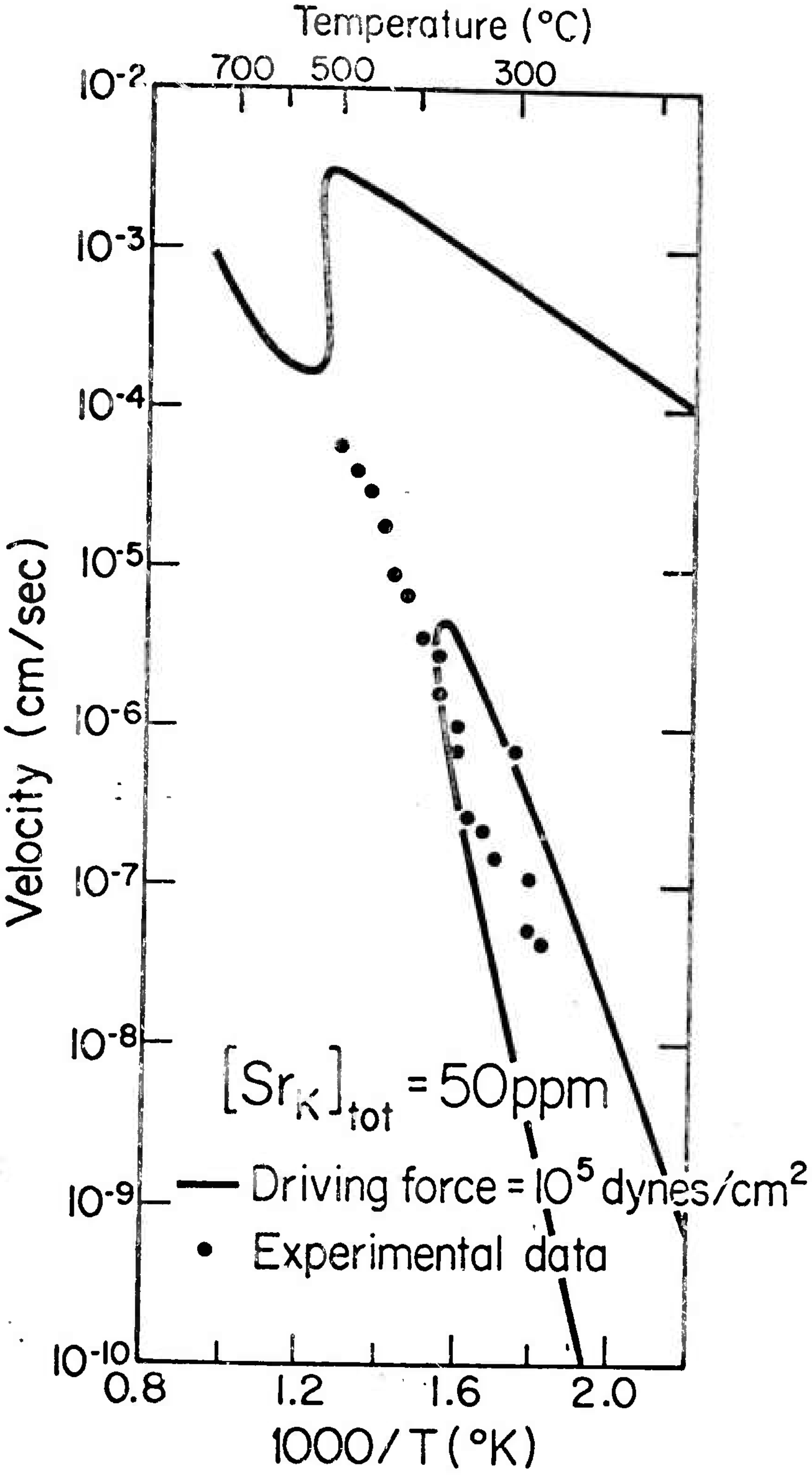

Figure C4. Calculated grain boundary mobility for Sr doped KCl considering only electrostatic interactions.

This may be so for a strain interaction, particularly in dilute solution, but it is not obviously so for the electrostatic interactions. The origin of the space charge cloud is essentially due to the difference in the distributions of the charged species, namely the unassociated Sr ions, and K and Cl vacancies. The space charge potential, ϕ, must satisfy Poisson's equation, $\frac{d^2\phi}{dx^2} = -\frac{4\pi\rho}{\varepsilon}$. However, ρ is composed of two major components, namely free Sr ions, $Sr_K^{\cdot}$, and free K vacancies, $V_K^{'}$. The contribution of free Cl vacancies, $V_{Cl}^{\cdot}$, is not significant in Sr-doped KCl in the extrinsic temperature region. Furthermore, the relative proportion of $Sr_K^{\cdot}$ and $V_K^{'}$ in the total charge density, ρ, also varies with temperature. At temperatures above the isoelectric temperature, the $V_K^{'}$ constitutes the bulk of the charge density whereas at temperatures below the isoelectric temperature, the charge density is mainly due to the $Sr_K^{\cdot}$ impurity cloud. Furthermore, the charge distributions are affected by the strain field interaction between the charged species and the grain boundary.

When the grain boundary migrates, the space charge potential will be affected by the variation of the impurity distribution which is a function of the boundary velocity. This will introduce a velocity dependence to the interaction energy, U, between the dopant and a moving boundary. We previously showed that for the purely electrostatic case the velocity dependence of ϕ was relatively small because the distribution of the more mobile vacancies readjusts in response to the changes in solute distribution; Yan et al. (1975b). Consequently the static values of ϕ could be used in Eqs. (4) and (5) or in other calculations of solute or defect distributions.

The calculations for the coupled strain and electrostatic forces are more approximate than those for the purely electrostatic case because the detailed form of the strain field is not known, but must be assumed and treated parametrically. In addition, the assumption of a negligible velocity dependence of the electrostatic field is not as good for the coupled case as for the purely electrostatic case, especially at high velocities. Nevertheless, the calculations, Fig.C3 indicate that the low velocity drag is relatively insensitive to the detailed form of the strain field assumed.

Especially at temperatures near the isoelectric temperature, the existence of the strain field interaction causes a significant change in the electrostatic field near the boundary, (see B, Figs. B1 - B4). Thus as the velocity is increased and the excess solute concentration near the boundary decreases the electrostatic potential will approach that for a uniform distribution of solute. This is much more like that for the static case with $U_o = 0$, than with the finite strain interaction. The effect on α will be quite small since it is representative of the low velocity limit where the solute profiles are changed only very slightly. The greater effect will be on the integral in Eq. (5), and so β^{-1} is more likely to be effected than will α. This means the greater uncertainty from this approximation will be on the conditions for breakaway from the solute cloud.

Overall the agreement between the experimental data and the theoretical calculations is improved by including a strain field interaction. This suggests the basic concept is valid and warrants further development of the theory. The calculations done to date all suggest that the temperature range for which the impurity drag would be effective would increase in order for the additives Ba^{2+}, Sr^{2+} and Ca^{2+}. Attempts to verify this experimentally were inconclusive because of unexpectedly low rates of nucleation of large grains, Bowen et al (1977).

C.3. Breakaway from the Solute Cloud:

From the steady state solution, if M_o and $(1/\alpha C_\infty)$ are sufficiently different, the drag force has a local maximum of $F_{max} \simeq \frac{C_\infty \alpha}{2} \beta^{-1}$ at the boundary velocity, $V_{max} \simeq \beta^{-1}(1+\frac{4}{C_\infty \alpha M_o})^{1/2}$ and also a local minimum of $P_{min} \simeq 2\ (\alpha C_\infty / M_o)^{1/2}\ \beta^{-1}$ at $V_{min} \simeq (M_o C_\infty \alpha)^{1/2} \beta^{-1}$. When the experimental driving force, F, is $F_{min} < F < F_{max}$, there exist three possible velocity solutions for Eq. (3), as shown in Figs. (C3) and in some temperature range. The intermediate solution is unstable and so physically uninteresting. However, in this range it is possible for a boundary to move at either the slow, drag limited velocity, or the fast, intrinsic velocity. The time dependent problem which would indicate the conditions for achieving either mode has not been solved. It is anticipated that transitions between the two modes may result from local fluctuations along the boundary. If the amount of solute at the boundary is reduced it may lead to a transition from the slow to the high speed mode. Conversely, if a region of high speed boundary slows down it may accumulate impurity and then shift to the slow velocity mode. An estimate of the conditions for this instability can be obtained from consideration of the geometrical instabilities which can result during the motion of a planar boundary.

If a boundary has a waviness, as in Fig. C5 the local motion of an impurity as it is dragged by the boundary will include a component perpendicular to the average direction of motion of the boundary. This lead to a tendency to accumulate impurity in the slower regions of the boundary which increases the drag and may further slow such regions. This convective effect similarly tends to remove impurity from the more rapid, bulging regions leading to a local reduction in the drag. The impurity redistribution (parallel to the boundary) is resisted by parallel diffusion of the impurity, with D', and the surface tension of the boundary, γ. From a simplified model of the problem, Roy and Bauer (1975) showed that for small fluctuations along a boundary, the

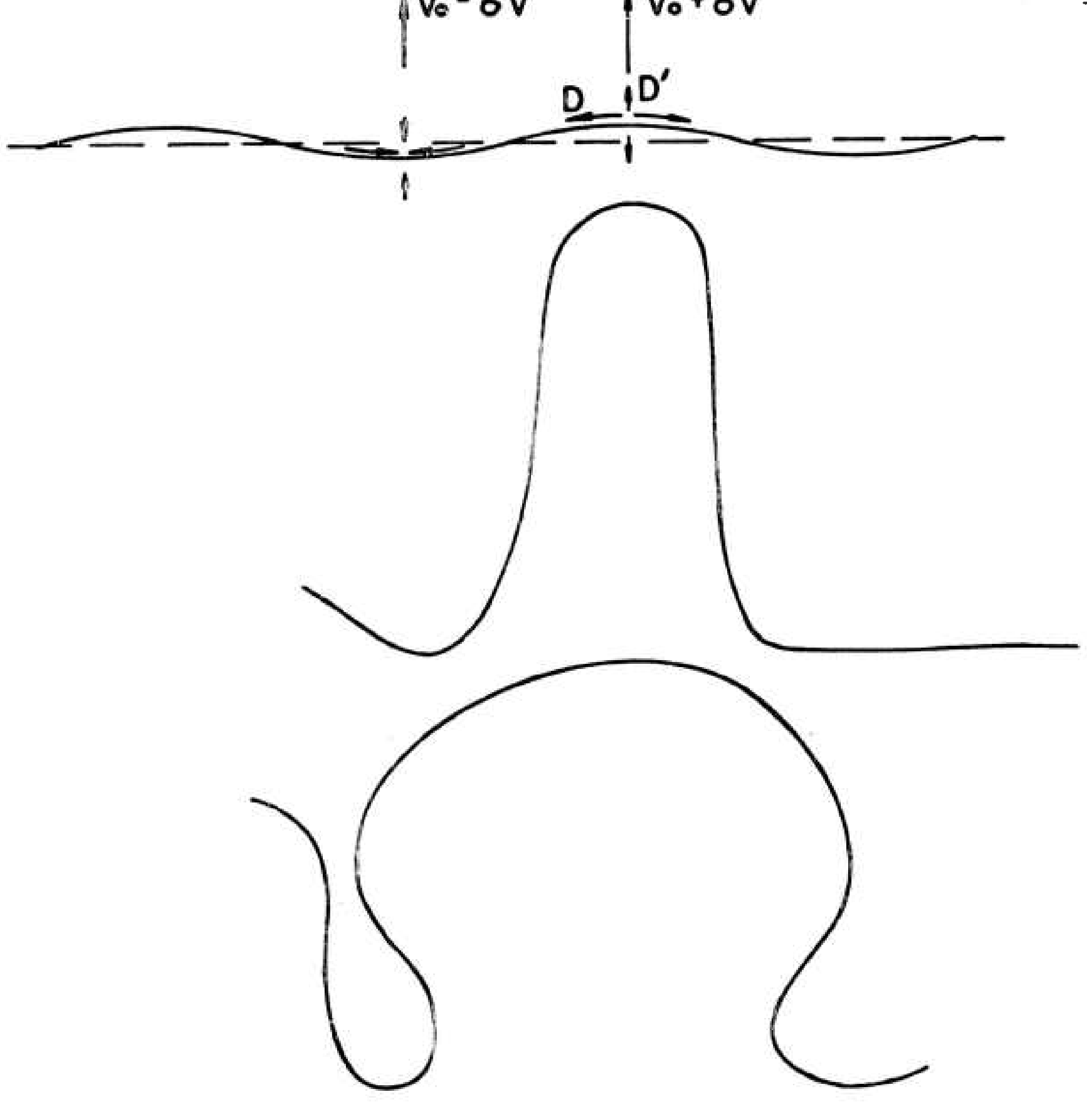

Figure C5. Schematic of breakaway of a grain boundary from its impurity cloud by growth of unstable velocity pertubations.

position of the boundary and the impurity at the boundary can be expressed in terms of the steady state values for the average velocity, V_o, and solute concentration at the boundary, C_o, plus the correction terms of the form:

$$\Delta X(y,t) = [A_1\exp(q_s^{+}t) + A_2\exp(q_s^{-}t)]\cos\frac{2\pi y}{\lambda} \tag{11}$$

and

$$\Delta C = [A_3\exp(q_c^{+}t) + A_4\exp(q_c^{-}t)]\cos\frac{2\pi y}{\lambda} \tag{12}$$

where A_i are amplitudes of the pertubations. By modifying the perturbation analysis to include the nonlinear drag force and excess solute concentration at the boundary it can be shown that

$$q^{\pm}_{s,c} = (1/2)k^2_{s,c}\left\{-Q \pm \sqrt{Q^2 - 4D'\gamma + \frac{4C_\infty V_o^2\alpha}{(1+\beta^2V_o^2)k^2_{s,c}}}\right\} \tag{13}$$

and in the low velocity limit,

$$Q = D' + \cfrac{\gamma V_o}{\cfrac{V_o}{M_o} + \cfrac{\alpha C_\infty V_o}{1+\beta^2V_o^2}\left\{\cfrac{C_\infty}{C_o}\exp\left(\cfrac{-U(0)}{kT}\right) - \cfrac{2\beta^2V_o^2}{1+\beta^2V_o^2}\right\}} \tag{14}$$

and in the high velocity limit,

$$Q = D' + \cfrac{\gamma V_o}{\cfrac{V_o}{M_o} + \cfrac{\alpha C_\infty V_o}{1+\beta^2V_o^2}\left\{\cfrac{C_o}{C_\infty} - \cfrac{2\beta^2V_o^2}{1+\beta^2V_o^2}\right\}} \tag{15}$$

It is obvious from Eq. (13) that q^- is always negative and cannot contribute any instability to the grain boundary motion. However, where $q^+ > 0$, i.e.,

$$D' < \frac{\lambda^2_{s,c}\,C_\infty\alpha V_o^2}{(2\pi)^2(1+\beta^2V_o^2)\gamma} \tag{16}$$

the perturbations in both the shape and concentration profile will grow and instability in the grain boundary motion will result. This condition of instability, Eq. (16), holds for both the low and high velocity limits; and to the first approximation, it may be correct for all velocities.

Experimentally, it is easier to treat the driving force F rather than the dependent variable V_o. In the solute limited region the driving force is balanced by the solute drag force, Eq. (3). Consequently, the condition of instability, Eq. (16), can be expressed in terms of the driving force, F, as

$$\lambda^2 > \lambda_c^2 = \frac{(2\pi)^2 \alpha C_\infty \gamma D'}{F^2 (1 + \beta^2 V_o^2)} \qquad (17)$$

$$\simeq \frac{(2\pi)^2}{F^2} \alpha C_\infty \gamma D' \text{ in the low velocity limit}$$

Essentially for long wavelengths, λ, at which $q > 0$, any fluctuations are stable and will grow spontaneously. For all driving forces, F, if $\lambda > \lambda_c$ dimensional instability of boundaries can result leading to wavy boundaries. Further, if $F_{min} < F < F_{max}$, this geometrical instability may lead to pertubations which allow the transition between velocity modes. The explicit inclusion of the possibility of evaporation or condensation of impurity from the boundary is expected to lead to a wider range of instability, i.e., smaller λ_c. If a half wave segment shifts from the low to high velocity regime, it may spread laterally, Fig.C5 and carry a large segment of the entire boundary into the high velocity mode. It is thought that for these intermediate driving forces, the actual velocities of boundaries may be distinctly nonuniform or jerky as they switch from one mode to the other.

The switch to high velocities could lead to orders of magnitude higher rates of growth during recrystallization, Yan et al. (1975a), Cannon et al., (1976). The irregularly shaped grains frequently seen during low temperature recrystallization of KCl, Fig. C6, are thought to be representative of this process. Idiomorphic grains are also seen which are thought to result from boundaries in which the entire boundary has made the transition to intrinsic velocity. Thus for a given situation Eq. (17) provides a condition on the amount and type of solute necessary to inhibit breakaway and rapid recrystallization. The upper limit to λ is of course the physical dimension of the piece, but as a practical matter λ_c may not need to be quite so large.

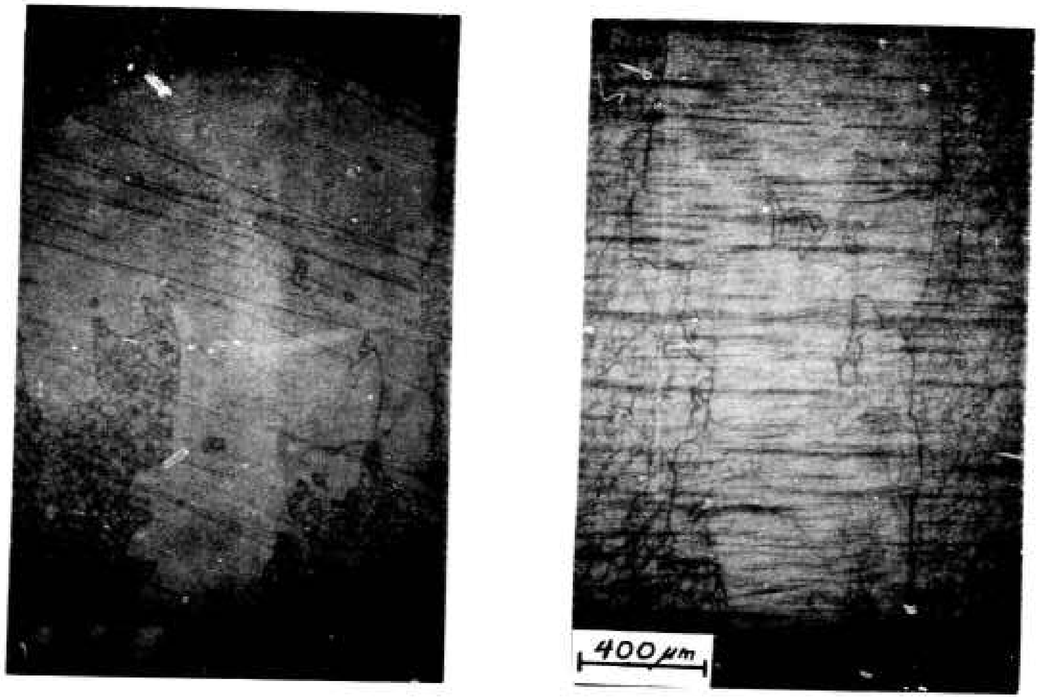

(a) (b)

Figure C6. Irregular grains in forged and annealed pure KCl (a) and from dynamic recrystallization in pure KCl (b).

C. 4. References

H. K. Bowen, et al, (1977) Research on Materials for High Power Laser Windows, Semi-Annual Technical Report No. 3, RADC-TR-77-227.

J. W. Cahn, (1962), Acta. Met., <u>10</u>, 789.

R. M. Cannon, M. F. Yan and H. K. Bowen, (1976), "Substructure Formation During Halide Processing", in Proceedings of the Fifth Conference on Infrared Laser Window Materials, ed., C. R. Andrews and C. L. Strecker, ARPA.

B. G. Koepke, et al. (1974), J. Appl. Phys. <u>45</u>, 969.

K. Lucke and H. P. Stuwe, (1962), "On the Theory of Grain Boundary Motion", in Recovery and Recrystallization of Metals, ed., L. Himmel, Interscience/AIME.

A. Roy and C. L. Bauer, (1975), Acta. Met., <u>23</u>, 957.

M. F. Yan, (1976), "Grain Boundary Mobility of KCl", Sc.D. Thesis, M.I.T., Department of Materials Science and Engineering.

M. F. Yan, R. M. Cannon and H. K. Bowen, (1975a), "Substructure Formation in Hot Forged KCl and KBr", in Research on Materials for High Power Laser Windows, N. J. Grant, et al., AFCRL-TR-76-0027.

M. F. Yan, R. M. Cannon and H. K. Bowen, (1975b), "Impurity Drag Theory in Grain Boundary Migration of KCl", in Research on Materials for High Power Laser Windows, N. J. Grant et al., AFCRL-TR-76-0027.

M. F. Yan, R. M. Cannon, H. K. Bowen and R. L. Coble, (1975c), "Grain Boundaries and Grain Boundary Mobility in Hot Forged Alkali Halides", in Deformation of Ceramic Materials, ed., R. C. Bradt and R. E. Tressler, Plenum Press, N. Y.

D. GRAIN BOUNDARY MIGRATION IN CERAMICS

M. F. Yan
Bell Laboratories
Murray Hill, N.J.

R. M. Cannon and H. K. Bowen
Massachusetts Institute of Technology
Cambridge, Massachusetts

ABSTRACT

Conditions under which four possible mechanisms may control grain boundary mobility are described. Intrinsic mobility, impurity drag, pore or particle drag, and liquid phase control are considered and possible mechanisms for transitions among these regimes are suggested. The particular mechanism controlling mobility can affect the kinetics of grain growth and the resulting grain morphologies. A survey of the data for many ceramics indicates qualitative agreement with theory.

INTRODUCTION

The importance of microstructural control in achieving the desired mechanical, electrical, magnetic and optical properties in ceramic materials cannot be over-emphasized. For sintered materials the microstructural evolution depends upon the characteristics of the starting powder (e.g., particle size, size distribution, particle shape and particle agglomeration); the green compact microstructure (e.g., green density, binder material and the state of particle agglomerates); and finally the sintering and coarsening processes. During sintering, pores are removed from a ceramic body and grain boundaries develop between particles. If a dopant is added, the dopant ions will further react with the major constituents and may be redistributed for thermodynamic or kinetic reasons. The grain boundaries developed during sintering act as vacancy sinks permitting pore removal and densification. However, the boundaries tend to migrate toward their center of curvature to reduce the total grain boundary area and energy. Consequently, the kinetics of grain boundary migration have a profound effect on the sintering process, on the achieveable final grain sizes and densities, and on resultant physical properties. Even in forged, cast, or CVD ceramics grain boundary motion may be important.

Although the boundary mobility and the microstructure can be significantly affected by subtle changes in the dopant[1] and porosity levels, the mechanisms of grain boundary migration are not yet well understood. A dramatic demonstration of this variability can be seen in the collection of grain boundary mobility data in Fig. 1 for many ceramic oxides with varying purities, densities and amounts of second phases.[2-34] For example, the measured boundary mobilities in MgO differ by as much as 10^4 at one temperature.

THEORY

In order to understand data (like that in Fig. D1), the motion of grain boundaries is first considered in terms of four different limiting cases which are shown schematically in Fig. D 2, and are referred to as: intrinsic, impurity drag, pore drag, and liquid phase controlled. The conditions under which the various mechanisms may be controlling are then examined. Frequently more than one regime may be possible for a given experimental situation; possible mechanisms for transitions among the regimes are considered. Finally the effects of the mechanism controlling mobility on the kinetics of grain growth and the resulting grain morphologies and pore distributions are discussed.

The intrinsic grain boundary mobility refers to motion limited by the movement of ions across the grain boundary of a width of a few Ångstroms and includes the processes of detachment from one side of the boundary and attachment to the other side. Under the proper conditions, this process can control the boundary motion even in typical ceramic materials which have impurity or nonstoichiometry which create atomic defect concentrations greater than those due to thermal energy (e.g., Schottky or Frenkel). Thus the use of the term intrinsic does not refer to a process which occurs only in pure ceramics. For simplicity, it is assumed that the impurities within the grain can on average move as rapidly across the boundary as the host ions and that they do not affect the grain boundary diffusivity. Thus, although it need not be, the intrinsic mobility is taken to be independent of solute species and concentration.

The major effect of impurities which do not exist as a second phase is shown descriptively in Fig. D2. If the impurities are attracted (or repelled) to the grain boundary

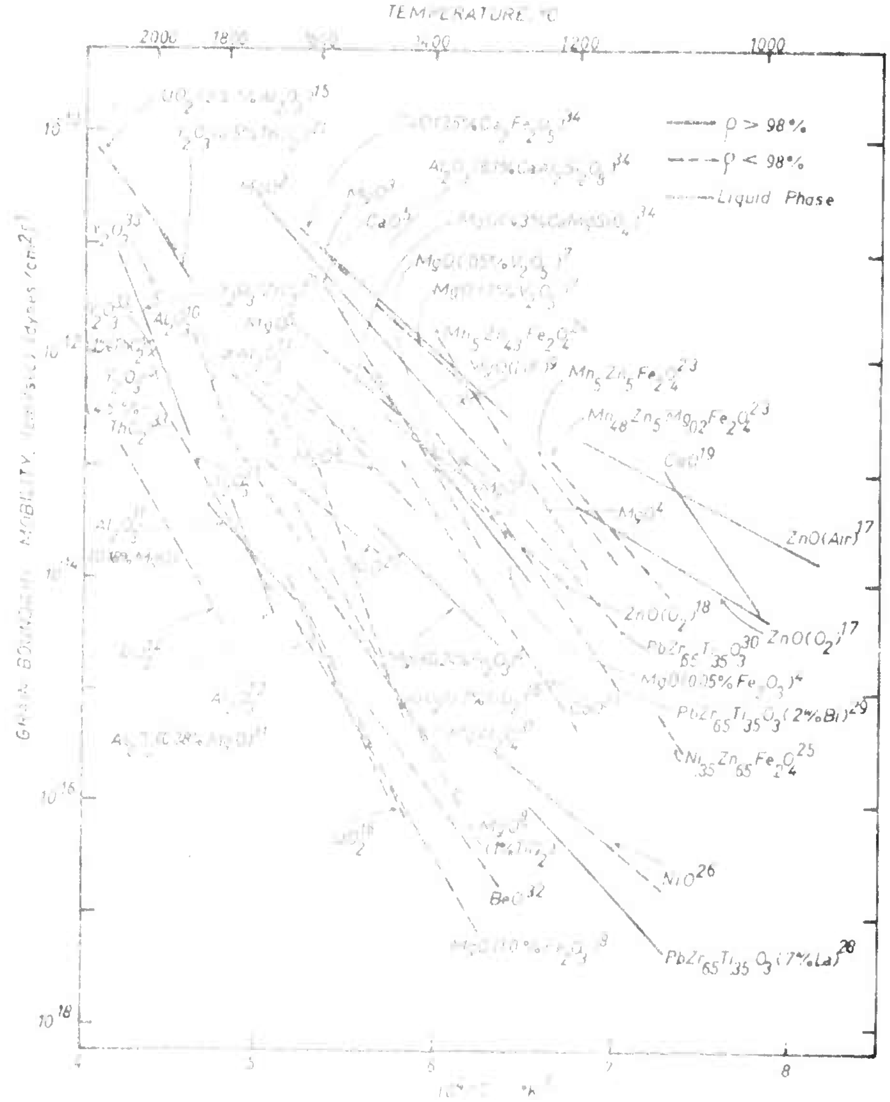

Figure D1. Grain boundary mobility as a function of temperature for oxides. Distinction was made for those known to have second phase liquid at the grain boundaries and those with densities greater than 98% theoretical. The additive concentrations are in cation fraction unless otherwise noted.

and exist in concentrations which are greater (or less) than the bulk value in the "near grain boundary region",[35] then these ions may be carried along by a moving boundary. If these ions are in a region, 2δ, wider than the boundary core, ω, the diffusivity controlling their motion will be similar to a bulk diffusivity rather than a grain boundary diffusivity. The motion of these impurity ions may limit the velocity of the boundary.

If there is a liquid layer of thickness, ℓ, between grains, the transport in the liquid is rapid but the diffusion distance ℓ will be larger than ω. Two limiting processes controlling boundary motion are considered: diffusion through the liquid and surface reaction kinetics.

Finally, the fourth situation arises when a drag force is exerted by second phases which may be crystalline particles, liquid droplets, or pores. Then the motion of the boundary is frequently limited by the motion of the second phase particles.

Intrinsic Grain Boundary Mobility

From absolute reaction-rate theory, Turnbull[36] has derived an expression for the velocity, V, of a high angle grain boundary acted upon by a driving force, F, across the boundary width, ω:

$$V = \frac{kT}{h} \cdot \frac{e\Omega\omega F}{kT} \exp(-\Delta G_i/kT) \simeq \frac{D_b}{\omega}\left(\frac{\Omega F}{kT}\right) \qquad (1)$$

where ΔG_i is the free energy of activation for the migration process; h, Planck's constant; Ω is the ionic volume; D_b is the appropriate grain boundary diffusion coefficient; kT has its usual meaning; and e is the base of Naperian logarithms.

In a ceramic, the migration of a grain boundary requires the simultaneous diffusion of cations and anions. If the diffusivities of the two ions are different, the migration process is limited by the diffusivity of the slower diffusing species. Generally, the cations diffuse much slower than the anions in the grain boundaries; then, the intrinsic grain boundary velocity is limited by the cation grain boundary diffusivity .

The effects of grain boundary structure may be important leading to mobilities lower than those given by the Turnbull expression, Eq. (1), to anisotropic mobilities and possibly to impurity effects. The structural effects envisaged are analogous to those in crystal growth models in which an accomodation coefficient is included to account for atomistic attachment or detachment occurring at only a fraction of the atomic sites; e.g., screw dislocation growth.[37] Gleiter[38] has derived an expression for intrinsic grain boundary migration in which a specific atomistic model was assumed. The transport

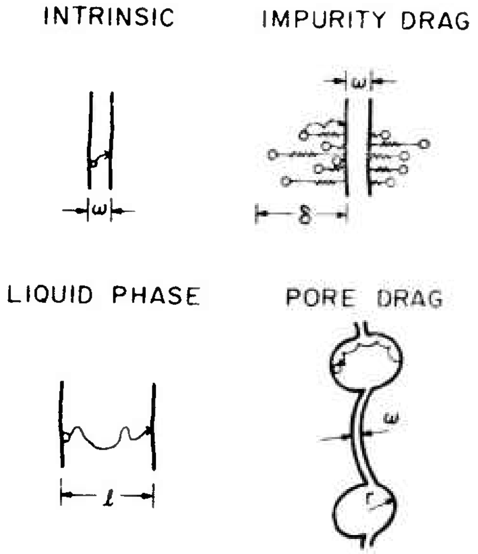

Figure D2. Schematic representation of grain boundary motion limited by intrinsic, impurity drag, liquid phase diffusion, and pore drag mechanisms.

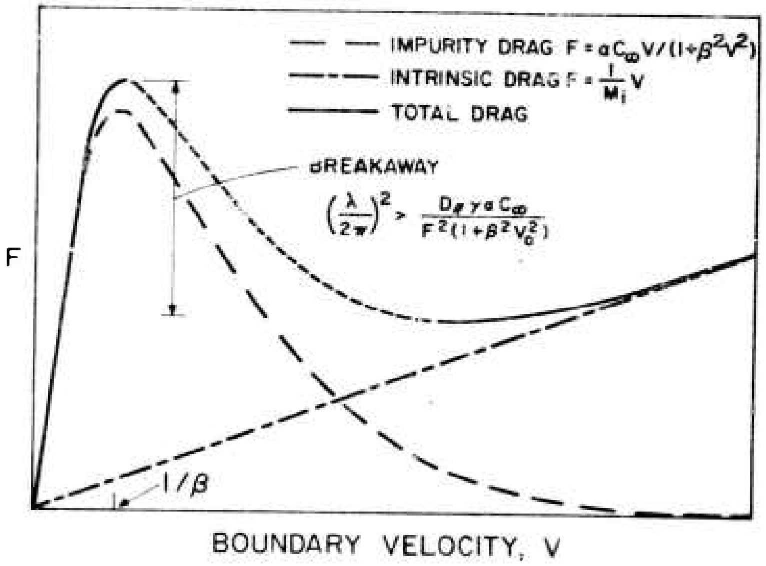

Figure D3. Intrinsic and impurity drag forces on a grain boundary moving at velocity, V.

of an atom from a kink site in a step on the surface of a shrinking grain to a similar site on a growing grain was assumed to occur by several separable kinetic processes: (a) dissociation of the atom from the kink site; (b) atomic diffusion along the step; (c) dissociation from the step; (d) diffusion on the surface and desorption into the grain boundary region; and (e) diffusion in the grain boundary and adsorption on the surface of the growing grain, and the reverse attachment steps.

The velocity expression obtained by Gleiter is incorrect; each of the above separate processes was assumed to always be relatively slow leading to an activation energy which is the sum of those for all the processes rather than just that of the slowest process(es) which limits the rate of atomic jump across the boundary. However the interesting features are continued in the expression

$$V = f \frac{kT}{h} \frac{\Omega}{b\omega} \frac{\Omega F}{kT} g \exp(\frac{-\Delta G}{kT}) \qquad (2)$$

where b is the Burgers vector. The important differences compared to Eq. (1) are in the function f which is related to the step density and is limited to $0 \leq f \leq 1$. Gleiter argued that f may be controlled by structural considerations and that under certain conditions it may be affected by the driving force leading to a nonlinear relationship between velocity and driving force. The activation energy should be that for the slow process(es), but there may be additional pre-exponential terms, g, to account for the other processes. A strong anisotropy may result from f such that boundaries nearly parallel to low index planes may have low step densities and mobilities. For a coherent twin boundary with a zero step density, f will vanish and the boundary will be immobile.

Solute Drag

If an interaction potential exists between solute ions and the grain boundary, these ions tend to be non-uniformly distributed in the near grain boundary region. Near a stationary grain boundary, the distribution profile is symmetrical and there is no net interaction force between the grain boundary and the solute on both sides of the boundary. As the boundary migrates, the concentration profile becomes asymmetric and this results in a net drag force on the moving boundary. The derivation of a rate equation entails the calculation of the impurity distribution and the motion of the solute relative to the moving boundary. If the driving force is too high, the boundary will break away from the impurity cloud and the velocity will approach that given by Eqs. (1) or (2).

Impurity drag models have been derived by Cahn[39], Lucke and Stuwe[40], Hillert and Sundman[41] and others. The more quantitative and concise model of Cahn[39] is described here. This one dimensional model is based on the following assumptions: (1) There is a dilute solution of solute in the matrix, thus the chemical potential for the impurity is, $\mu = \mu_o + kT\ell nC$, where C is the dopant concentration. (2) There exists an interaction energy, U, between the solute and the grain boundary which is assumed to have the following properties; (a) it is not a function of velocity; (b) it is not an explicit function of local dopant concentration; but (c) it is a function of the spatial coordinates in the frame of reference of the moving boundary. (3) The Einstein relation between the diffusion coefficient and the mobility is assumed. (4) Only the steady state condition is considered; thus the grain boundary velocity, V, is a constant.

Because of the convective motion of the impurity relative to the boundary

$$\frac{\partial C}{\partial t} = -V \frac{\partial C}{\partial x} \tag{3}$$

The chemical potential of the impurity in the near grain boundary region is

$$\mu = kT\ell nC + U(x) + U_o \tag{4}$$

where U_o is a constant. The impurity flux, J, as observed from the reference frame of the moving grain boundary is

$$J = -\frac{DC}{kT}\frac{d\mu}{dx} \tag{5}$$

The impurity profile, C(x), can now be calculated from the continuity equation

$$\frac{\partial J}{\partial x} + \frac{\partial C}{\partial t} = 0 \tag{6}$$

and the boundary conditions at $x = \infty$: $dC/dx = 0$, $dU/dx = 0$ and $C(\infty) \equiv C_\infty$. Thus, C(x) must satisfy,

$$D\frac{dC}{dx} + \frac{DC}{kT}\frac{dU}{dx} + V(C - C_\infty) = 0 \tag{7}$$

The drag force per unit of solute is $-dU/dx$. The net impurity drag force on the boundary, F_i, due to C(x) is,

$$F_i = -N_v \int_{-\infty}^{\infty} [C(x) - C_\infty] \frac{dU}{dx}\, dx \tag{8}$$

where N_v is the matrix atom density. The C(x) which satisfies Eq. (7) is used to calculate a drag force from Eq. (8). A simpler approximate form which describes both high and low velocity extremes is

$$F_i = \frac{\alpha C_\infty V}{1 + \beta^2 V^2} \tag{9}$$

where

$$\alpha \equiv 4N_V kT \int_{-\infty}^{\infty} \frac{\sinh^2 \left(\frac{U(x)}{2kT}\right)}{D(x)}\, dx \tag{10}$$

and

$$\frac{\alpha}{\beta^2} \equiv \frac{N_V}{kT} \int_{-\infty}^{\infty} \left(\frac{dU}{dx}\right)^2 D(x)\, dx \tag{11}$$

Physically, α is the impurity drag per unit velocity and per unit dopant concentration in the low velocity limit; and β^{-1} is the drift velocity with which an impurity atom moves across the grain boundary region. From the form of α, Eq. (10), dopants with either attractive or repulsive interaction energies of equal magnitude will exert similar drag forces.

The intrinsic drag on the moving grain boundary, F_o, is given by an expression such as that from Turnbull, e.g., Eq. (1) or (2).

$$F_o = \frac{1}{M_o} V \tag{12}$$

where M_o is the intrinsic boundary mobility. The total drag force, Fig. 3, is the sum of these two and is just equal to the driving force at steady state.

$$F = F_o + F_i = \frac{V}{M_o} + \frac{\alpha C_\infty V}{1 + \beta^2 V^2} \tag{13}$$

In the low velocity limit, where the impurity drift velocity across the near grain boundary region is high relative to the grain boundary velocity, $\beta^{-1} >> V$, there is a linear relationship between the velocity and the drag force

$$V \simeq \frac{F}{\frac{1}{M_o} + \alpha C_\infty} \tag{14}$$

This is the experimentally interesting regime considered for the impurity drag model in Fig. D2. At high velocities the amount of excess impurity near the boundary is very small and the velocity approaches the intrinsic value. Even at low velocities the amount of excess solute at the boundary decreases as V increases. From Fig. D3, it can be seen that there is a range of conditions for which there are three possible solutions to the force-velocity equation. The intermediate solution is unstable and so physically unimportant. However, it is possible for a boundary to move at either the fast or slow velocity for driving forces between F_{max} and F_{min}.

In the Cahn model D(x) and U(x) are left arbitrary; they must be specified in order to calculate the drag for a particular system. These functions are generally not known for metals. In ionic materials the distributions of aliovalent impurities and charged defects around the boundary are controlled by electrostatic fields as well as strain energy or other interactions. For alkali halides the electrostatic forces and defect distributions around boundaries can be calculated using space charge theory. This provides one case where D(x) and U(x) can be explicitly expressed and the impurity drag calculated.[1] Modifications can be made to include secondary solute-boundary interactions. Although the problem has not been solved for oxides similar interactions are expected to exist.

The existence of space charge regions near lattice discontinuities (free surfaces, dislocations and grain boundaries) was first postulated by Frenkel[42] and the charge distributions have been formulated by Frenkel[42], Lehovec[43], Eshelby et al[44], and Kliewer and Koehler[45]. This electrostatic field develops because of the differences in the free energy of formation of positively and negatively charged defects and the need to maintain neutrality in the bulk by adjusting the defect concentrations. From the formulation of Kliewer and Koehler the defect distributions, solute distributions, and the electrostatic space charge potential distributions in the space charge double layer region of the free surfaces in pure and divalently doped alkali halides can be calculated[45,46]. These distributions are expected to be similar near a grain boundary. Both the charged vacancies and aliovalent solute ions in the space charge region experience an electrostatic interaction force with the grain boundary and assume non-uniform distributions in order to minimize the free energy. Since the vacancy diffusivity is significantly faster than the solute diffusivity, the drag force on a moving boundary due to vacancies is much smaller than the impurity drag.

An interaction between a moving grain boundary and dopant ions can also originate from the strain energy caused by the size mismatch between the matrix and impurity ions, i.e., the difference in the strain energy of a solute ion placed at or near the grain boundary region instead of in the crystal lattice. For aliovalent ions the strain field interaction is coupled with the electric field because these ions have an excess charge. Thus the distribution of the charged ions and defects within the charge cloud and the electrostatic potential distribution can be significantly affected by the strain field or other secondary interactions.

For a given functional form of the strain field interaction energy, the solute and defect distributions near the grain boundary can be formulated[1] following the technique of Kliewer and Koehler[45]. Poisson's equation is expressed in terms of solute and defect distributions in the grain boundary region and can be solved by numerical analysis.[1] Calculated equilibrium impurity and vacancy concentration distributions satisfying the coupled electrostatic and mechanical strain fields are shown in Fig. D4 for KCl containing 50 ppm Ca. The total interaction energy is $U(x) = [U_S(x) - U_S(\infty)] + [e\phi(x) - e\phi(\infty)]$ where $[U_S(x) - U_S(\infty)]$ is the strain energy difference between impurity ions at a distance x from the grain boundary as compared to the bulk; and $[e\phi(x) - e\phi(\infty)]$ is the electrostatic potential near the surface as compared to the bulk. The maximum value of the strain interaction energy was taken to be[40]

$$U_s(o) = \frac{4\pi E\ r^3}{(1+\nu)}\left(\frac{\Delta r}{r}\right)^2 \qquad (15)$$

where E is the modulus; ν, Poisson's ratio; r the matrix ion radius; and Δr, the radius misfit. There are regions of both enhanced and depleted solute concentration because of these coupled interactions. Further, even near the isoelectric temperature there are appreciable electric fields near the boundaries because of this coupling.

The solute diffusion coefficient has a spacial dependence near the boundary due to the variation in the defect concentrations. Consider Sr-doped KCl; the Sr-ions can only move by associating with K vacancies. The probability of association in the bulk, p_∞, is determined largely by the electrostatic attraction between the differently charged solute ion and vacancy. The spacially dependent diffusion coefficient is[1,46]

$$D^{Sr}(x) = \frac{D_o p_\infty}{C_\infty p_\infty + (1-p_\infty)\, C_\infty \exp\left(-\dfrac{e\phi(x) - e\phi(\infty) + [U_S(x)-U_S(\infty)]}{kT}\right)} \qquad (16)$$

where Do is the diffusivity of Sr-vacancy complexes.

Using data from the literature for the Sr-vacancy diffusivity, the defect association enthalpy, and the interaction energy, U(x), the impurity diffusion coefficient, Eq. (16), can be evaluated. More importantly, the impurity drag parameters α and β can be determined from Eqs. (10) and (11). The intrinsic mobility can also be estimated from known experimental data and the use of Eq. (1). From these the velocity as a function of temperature for a fixed driving force has been calculated as is shown in Fig. D5. The driving force of 10^5 dyne/cm^2 corresponds to about 12μm diameter grains with very low misorientation angles and thus a boundary energy of about 40 ergs/cm^2. Over much of the temperature range

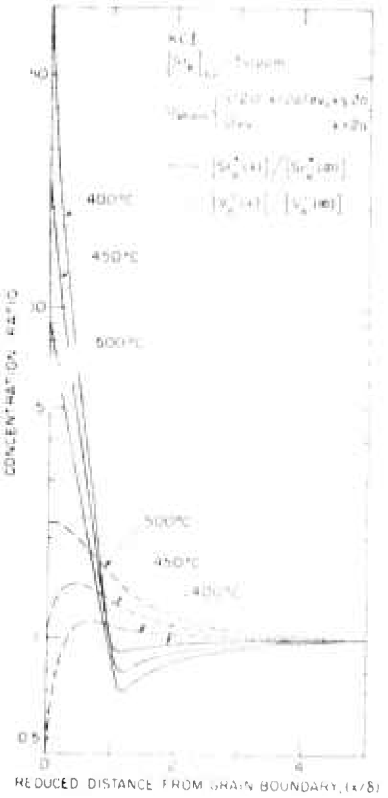

Figure D4. Concentrations of vacancies and Sr-impurity near the grain boundary of KCl. The range of the attractive strain field was assumed to be 2 lattice spacings. The maximum value (-0.2eV) is appropriate to Ca in KCl.

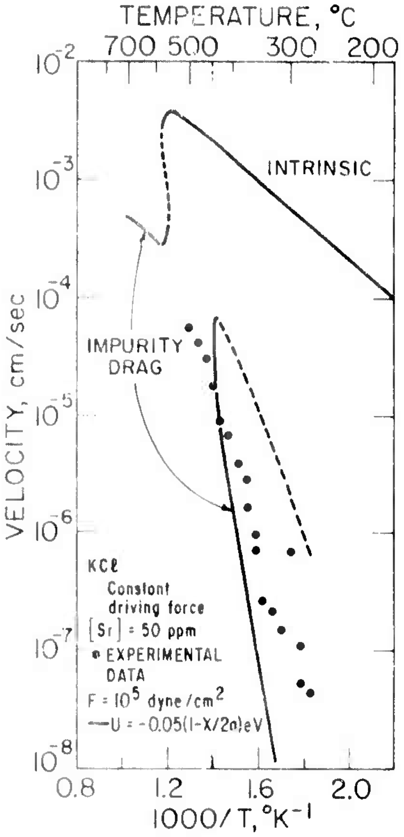

Figure D5. Calculated velocity of grain boundaries in Sr-doped KCl in which electrostatic and strain energy coupling are both included. The intrinsic and impurity drag regions are noted; the dashed line is an unstable solution. The points are experimental data. For these conditions the isoelectric temperature is 444°C.

motion in either the low velocity, impurity drag mode or the high velocity, intrinsic mode is possible for this driving force. The gap in the impurity drag solution results from the lower electrostatic attraction near the isoelectric temperature.

Recently, Hillert and Sundman[41], developed a solute drag model based upon the evaluation of the free energy dissipation due to diffusion when a grain boundary passes through a unit volume of the lattice. Their treatment utilized a regular solution model for the solute activity and is therefore valid even for a high solute concentration level. This formulation may be required in the more complex oxide systems e.g., ferrites and titanates in which solid solutions of several components commonly occur. At low concentrations this model is similar to the Cahn model.

Although the steady state solution for the impurity drag shows that over a range of driving forces the boundary may move at either of two velocities, the time dependent problem which would indicate the conditions for achieving or remaining in either mode has not been solved. It is anticipated that transitions between the two modes may result from local fluctuations along the boundary. If a slowly moving boundary enters a region where the driving force is higher or the impurity concentration is lower than the average values such that locally $F > F_{max} = \alpha C_{\infty}/2\beta$, then the boundary would likely jump to the higher, nearly intrinsic velocity. In making this transition it would shed most of its excess impurity. Conversely, if a boundary at high speed enters a region of lower driving force or higher solute concentration and slows down, it may accumulate further impurity and shift to the low velocity mode. These transitions need not occur uniformly along a boundary, but instead may start in a particular region and spread laterally along the boundary. The degree of spacial variability in F or C_{∞} sufficient to cause a transition is less if there is a tendency for impurity to redistribute laterally along a boundary. Any non-uniform lateral redistribution along a slow boundary would cause some regions to accelerate, to then lose more impurity laterally and to the surrounding lattice, and perhaps to make the transition to high velocity. An estimate of the conditions for which these transitions can occur can be obtained from consideration of the geometrical instabilities which can result during the motion of a planar boundary.

If a boundary has a waviness resulting from a velocity perturbation, as in Fig.D6, the local motion of solute ions dragged by the boundary will include a component perpendicular to the average direction of motion of the boundary. This moves impurity toward the slower regions of the boundary where it may accumulate, increase the drag, and further slow such regions. This convective effect removes impurity from the more rapid, bulging regions leading to a local reduction in the drag. This impurity redistribution parallel to the boundary is resisted by diffusion of the impurity parallel to the boundary and the surface tension of the boundary, γ. From a highly simplified model of the problem Roy and Bauer[47] showed that for small fluctuations, the position of the boundary and the excess impurity at the boundary can be expressed in terms of the steady state values for the average velocity, V_o, plus first order correction terms of the form:

$$\Delta X(y,t) = [A_1 \exp(q^+t) + A_2 \exp(q^-t)] \cos \frac{2\pi y}{\lambda} \tag{17}$$

and

$$\Delta C = [A_3 \exp(q^+t) + A_4 \exp(q^-t)] \cos \frac{2\pi y}{\lambda} \tag{18}$$

The time exponents of the fluctuations, q^+ and q^-, are complex functions of the driving force, velocity, drag parameters and diffusivities. Fluctuations with $q > 0$ will grow spontaneously whereas those with $q < 0$ decay. By modifying the perturbation analysis to include the nonlinear drag force, Eq. (13), it was shown that $q > 0$ for long wavelengths, λ, which satisfy:[1]

$$\lambda^2 > \lambda_c^2 = \frac{(2\pi)^2 \alpha C_\infty \gamma D'}{F^2 (1 + \beta^2 V_o^2)} \tag{19}$$

where D' is the effective diffusivity parallel to the boundary.

For any driving force if $\lambda > \lambda_c$ dimensional instability of boundaries can result leading to wavy boundaries. However, if $F_{min} < F < F_{max}$, this geometrical instability may lead to a transition between velocity modes. A better model explicitly including the possibility of gain or loss of impurity from the boundary from or to the matrix is expected to lead to a wider range of instability, i.e., smaller λ_c. If a half wave segment shifts from low to high velocity, it may spread laterally, Fig. D6, and carry a large segment of the entire boundary into the high velocity mode. For intermediate driving forces, the actual velocities of boundaries may be distinctly non-uniform or jerky as they switch from one mode to the other.

Drag from Pores and Particles

Porosity is the most common second phase in ceramic materials. Pores distributed throughout the matrix or located at the grain boundaries restrict boundary motion. The discrete nature of pores leads to important differences between pore drag and impurity drag: (1) the drag force due to pores on the moving front of the grain boundary is non-uniform as compared to the more nearly uniform impurity drag; (2) the pore mobility is frequently much slower than the impurity diffusion. Second phase particles similarly restrict grain boundary motion, but the mobility of particles may be lower than that for pores.

A pore pinned to a grain boundary can be dragged by the boundary at a velocity which depends upon the path of atom transport around or across the pore. The expressions for pore mobility, M_p, are generally of the form[48,49]

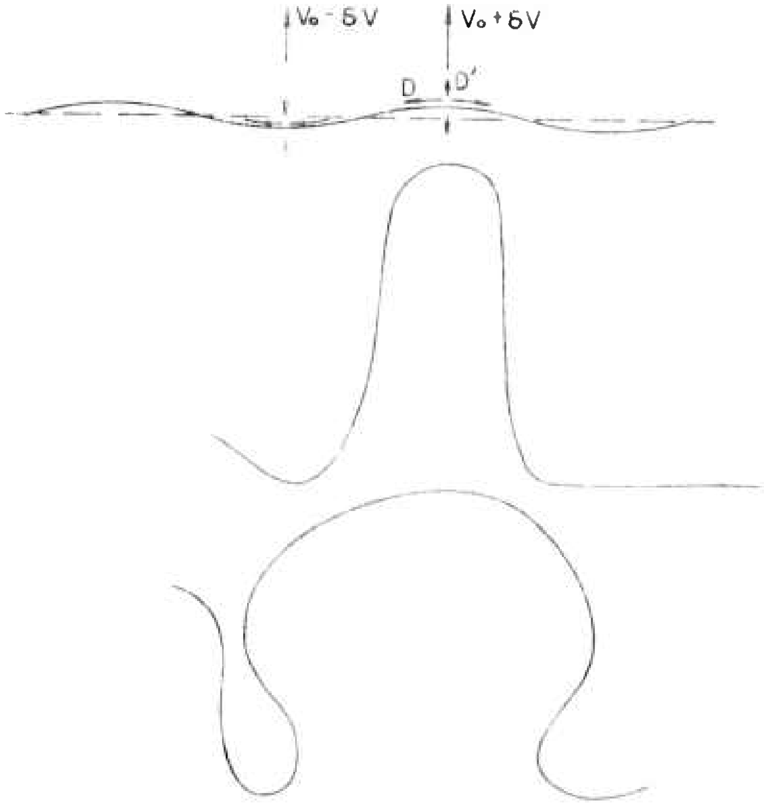

Figure D6. Schematic representation of the break-away of a grain boundary from its impurity cloud resulting from the growth of unstable velocity pertubations.

$$M_p = A \frac{\exp(-\Delta G_i/kT)}{r^n} \qquad (20)$$

The exponent of the pore radius, r, depends upon the transport path with $n = 3$ for lattice diffusion, $n = 4$ for surface diffusion, and $n = 2$ or 3 for vapor transport, and ΔG_i is appropriate to the particular process. For particles vapor transport is impossible and interface diffusion may be slower than surface diffusion in the case of pores.[50]

Brook[51] treated the kinetics of grain boundary motion under the influence of pore interactions. If the pores are attached to the grain boundary, the boundary velocity, V_b, is equal to the pore velocity, V_p, giving

$$V_p = F_p M_p = V_b = M_b(F - NF_p) \qquad (21)$$

from which

$$V_b = F \frac{M_b M_p}{NM_b + M_p} \tag{22}$$

where the pores are moving under a driving force, F_p. The boundary mobility, M_b, includes both intrinsic and impurity effects, Eq. (13). Part of the driving force on the grain boundary, F, is neutralized by the drag forces from the pores which have an areal density, N.

Two limiting cases can be observed:

a) $$\frac{NM_b}{M_p} >> 1, \qquad V_p = V_b = \frac{FM_p}{N} \tag{23}$$

$$F - NF_p \simeq \frac{FM_p}{NM_b} << F \tag{24}$$

The driving force on the boundary is nearly balanced by the drag forces from the pores, and the boundary motion is limited by the pore mobility.

b) $$\frac{NM_b}{M_p} << 1, \qquad V_p = V_b = FM_b \tag{25}$$

and

$$NF_p \simeq \frac{NM_b}{M_p} F \ll F \tag{26}$$

The driving force for grain boundary motion exceeds the total drag forces due to all pores and the boundary motion is limited by its mobility.

The maximum force which can be exerted on a spherical pore by an attached grain boundary is $\pi r\gamma$. When the grain boundary moves at a velocity, $V_b > V_p^{max} = M_p \pi r\gamma$, it separates from the pores. The upper limit for the force necessary for pore-grain boundary separation is, from Eq. (21):

$$F > \pi r\gamma \left(N + \frac{M_p}{M_b}\right) \tag{27}$$

The pore density on the boundary may be much higher for a slow boundary than for a fast one in which separation has occurred and so an analogous situation as for impurity drag is expected where for a particular driving force there may be two stable conditions of widely different V_b.

Qualitatively, three different modes of grain boundary migration can be expected. For larger, less mobile pores and low driving forces the pores will stay attached to the boundary and control the motion. For higher driving forces the boundary may separate from the pores and its motion will be limited by M_b. Smaller, more mobile pores may remain attached to the boundary, but not exert a significant drag on the boundary; impurities which lower M_b extend the range of this regime of pore attachment. The fact that M_b can assume two different values for some ranges in F further complicates delineation of the conditions for these modes. The separation from pores and break-away from impurities may be correlated in some cases.

Grain Boundary Mobility with a Liquid Film

It has often been observed that the rate of grain growth is rapid when a small amount of liquid wets the grain boundary area. The rate limiting cases which have been considered are: (1) diffusion of the bulk ions through the liquid; and (2) surface reaction, i.e., control by dissolution or precipitation.

The analysis is essentially that due to Greenwood[52] and Wagner[53] who treated a similar problem, the coarsening of particles. Smaller particles have a higher free energy and thus the ions dissolve into the liquid and precipitate on the surface of larger particles which have lower free energy due to lower curvature. In the coarsening case the diffusion field was assumed to be large, i.e., a dilute concentration of particles. Lay[15] corrected the expressions for the finite diffusion field for a liquid film around grains.

When diffusion through the liquid layer of thickness ℓ (Fig. 1) is rate limiting

$$V_\ell \simeq \frac{D_\ell C_\ell}{\ell} \frac{\Omega F}{kT} \tag{28}$$

where the motion results from the difference in solubility, C_ℓ due to curvature, $\Delta C_\ell = C_\ell \Omega F/kT$. Although D_ℓ and D_b may be of comparable orders of magnitude, if the film thickness is in the range $10^2 - 10^4$ Å the mobility is much less than the intrinsic mobility, Eq. (1).

The process may alternatively be controlled by the surface reaction rate, Wagner.[53] If it is slow relative to Eq. (28)

$$V'_\ell \simeq \frac{\Omega F}{kT} \kappa \tag{29}$$

The reaction constant, κ, is generally exponentially dependent on temperature but also depends on the precise kinetic process and may be dependent upon orientation and driving force.

Grain Growth Kinetics

Boundary motion can result from the free energy difference between phases during a solid-solid phase transformation, from strain energy during recrystallization, or simply from grain boundary curvature during grain growth. In principle, the overall grain growth kinetics can be predicted from the boundary velocity relations and specification of the driving force in terms of the evolving microstructure. A statistically averaged boundary velocity is assumed to be

$$V = \frac{1}{2}\frac{dG}{dt} \qquad (30)$$

The total driving force available can easily be obtained from the density of grain boundary energy as

$$F_t = \gamma S_v = \frac{2\gamma}{\bar{L}} \simeq \frac{3\gamma}{\bar{G}} \qquad (31)$$

where S_V is the boundary area per unit volume, $\bar{L}$ the mean linear intercept, and $\bar{G}$ the average grain size.[54] The maximum growth rate is then

$$\frac{dG}{dt} = \frac{6M\gamma}{\bar{G}} \qquad (32)$$

However, the net driving force for growth of most grains will be less than that predicted by Eq. (31) because the actual curvature of each boundary is less than that for an equivalent sphere. Hillert[55] has shown that a reasonable approximation for the net driving force which takes into account the actual curvature is

$$F_n = 2\eta\gamma\left(\frac{1}{G_c} - \frac{1}{G}\right) \qquad (33)$$

where η is a factor which is $\sim 5/4$*. Grains smaller than the critical grain size, G_c, have a net negative curvature and shrink and eventually disappear; those larger than G_c have a net positive curvature and grow. After a transient stage during which abnormal grain growth may occur, a steady state may be achieved in which there is a rather narrow size distribution. For this so-called normal growth the distribution of relative sizes, G/G_c, remains constant and there are no grains with size $G > 2G_c$.[55] The average size $\bar{G} = 8G_c/9$ increases as[55]

$$\frac{d\bar{G}}{dt} = \frac{M\gamma}{\bar{G}} \qquad (34)$$

The average driving force and growth rates are about 1/6 that predicted from the simple model, Eq. (32). However, if the growth is abnormal with only a few large growing grains, the growth rate of these large grains is given by Eq. (32).

---

* In three dimensions Eq. (33) is not exact. In the limit of $G \ll G_c$, $\eta = 1$;[55] for $G \gg G_c$, $\eta \simeq 3/2$ from Eq. (31).

When pores or particles are present and are relatively immobile (i.e., $NM_b \gg M_p$) they can pin boundaries and reduce the driving force sufficiently that a limiting grain size results. Zener[56] has shown that this occurs when the decrease in grain boundary area from grain growth is balanced by the increase in area as boundaries separate from the pores. For a uniform size distribution the limiting grain size, G_1, is $8r/3v$, where v is the volume fraction of pores. The pores provide an effective back stress resisting the motion of any boundary so that if there is a distribution of grain sizes the growth rate is approximately[55]

$$\frac{dG}{dt} = \begin{cases} 4\pi M_b\gamma\left(\frac{1}{G_c} - \frac{1}{G} + \frac{1}{G_1}\right), & \frac{G_1G_c}{G_1+G_c} > G \quad \text{(a)} \\ 0 & , \frac{G_1G_c}{G_1-G_c} > G > \frac{G_1G_c}{G_1+G_c} \quad \text{(b)} \\ 4\pi M_b\gamma\left(\frac{1}{G_c} - \frac{1}{G} - \frac{1}{G_1}\right), & G > \frac{G_1G_c}{G_1-G_c} \quad \text{(c)} \\ 0 & , G,\ G_c > G_1 \quad \text{(d)} \end{cases} \qquad (35)$$

The growth rate is essentially zero for those grains on which the net driving force is insufficient to tear the boundary away from the particles. Hillert[55] showed that for small initial grain sizes, normal growth can occur but the rate will decrease as the limiting size is approached. This asymptotic decay may be approximated by:[55]

$$\frac{dG_c}{dt} \simeq \frac{M_b\gamma}{G_c}\left(1 - \frac{G_c}{G_1}\right)^2 \qquad (36)$$

If the size distribution is narrow the final grain size, G_c, may actually fall in the range $\frac{2}{3}G_1$ to G_1 because the larger grains become immobile at $G < G_1$, i.e., Eq. (35b).

Normal growth can only continue if G_1 increases by dissolution or coalesence of the pores or particles. If coarsening occurs by diffusion between particles, i.e., Ostwald ripening, there will be a slow growth of r, which may follow a $t^{1/3}$ or $t^{1/2}$ dependence,[52,53] allowing a similar growth of G_c and G_1. This will occur on a much longer time scale than growth below G_1. Alternatively pores or particles can be dragged by the boundaries which also results in much slower growth controlled by M_p. As the smaller grains disappear the pores on these boundaries will coalesece[57] leading to an increase in r and G_1. Coalescence by particle drag will be more rapid than by interparticle diffusion only at small concentrations, v, of second phase.

For normal grain growth integration of Eq. (34) gives the familiar parabolic growth relation

$$\bar{G}^2(t) - \bar{G}^2(o) = 2M\gamma t \qquad (37)$$

This results only if the controlling mobility, M_b, is equal for all boundaries, as may occur under proper conditions for the intrinsic mobility or for solute drag in the low velocity limit.

Frequently, grain growth data are found to fit the relation $\bar{G}^n(t) - \bar{G}^n(o) = Kt$. If the growth is normal it may be inferred that

$$V = \frac{1}{2}\frac{d\bar{G}}{dt} = \frac{K}{2n\bar{G}^{n-1}} \qquad (38)$$

further, if the lower driving force, Eqs. (33) and (34), is appropriate, it may also be inferred that

$$M = \frac{V}{F} = \frac{K}{n\gamma\bar{G}^{n-2}} \qquad (39)$$

For some mechanisms the magnitude of the mobility will change with grain size as is implied by Eq. (39) if $n \neq 2$. When growth is controlled by particle drag and coalescence, the increase in r as $\bar{G}$ increases will cause M_p to decrease, Eq. (20). Similarly for a boundary with a thickening liquid film M may change with $\bar{G}$,[15] i.e., Eq. (28). Cubic growth, $n = 3$, can obtain for impurity drag control if the amount of solute segregated at the boundaries is much greater than that in the grain interiors.[58] This is most likely to occur at low temperatures and fine grain sizes with impurities which are strongly attracted to the boundaries. Transitions between impurity drag limited motion and the intrinsic velocity will result in various boundaries moving with much different mobilities which will invalidate the assumptions and detailed results of Hillert's theories,[55] such as Eqs. (34) and (36). The rate and steady state size distribution of normal growth will be altered by rapid disappearence of the smaller grains if the boundaries breakaway from the impurity cloud. Alternatively, the susceptibility to rapid abnormal growth will be increased if the boundaries of the larger grains can breakaway from the solute and grow at high velocity. Care must be taken to distinguish steady growth with $n = 3$ or 4 from asymptotically decaying growth of the type predicted by Eqs. (35) and (36). An analogous decay will result from a shift with increasing grain size from growth at the intrinsic mobility to control by impurity drag.

Generally, during sintering of ceramics all the pores are initially on the boundaries so the grain size is essentially at the limiting size, i.e., $\bar{G} \simeq G_1$. Normal growth can occur by pore drag or by growth of G_1 as further sintering reduces the volume fraction, v, of pores. Coalescence by diffusion between isolated pores will not be as important as further densification[57] unless pore shrinkage is inhibited by entrapped gas or a low dihedral angle. If G_c is somewhat less than G_1, normal growth may be slow relative to abnormal growth if there are a few grains large enough to have sufficient driving force to separate from the pores, Eq. (35c). Abnormal grains can grow to much larger sizes than G_1 with the final grain size determined by the number of these large grains which eventually impinge and remove all grains smaller than G_1.

The tendency for abnormal growth and pore entrapment will be significantly affected by solute drag. If there is sufficient solute, continued densification will result in a shift to impurity drag control when v and r become sufficiently small such that $NM_b \ll M_p$. The force for pore separation, Eq. (27), will then be larger than the case in which M_b is high as assumed in Eq. (35c) and pores will tend to stay attached to the migrating boundaries. Abnormal growth may then involve, but not necessarily require, breakaway from the impurity cloud and separation from pores. If a portion of boundary breaks away from the impurity cloud, it may have sufficient driving force to tear away from pores since M_b will then be significantly increased. The occurrence of an abnormal grain with boundaries which are solute free but which are carrying pores is possible. However, its growth is likely to be limited by further accumulation of pores as it migrates.

The velocity fluctuation method of breakaway from the solute cloud can provide a path for nucleation of abnormal grain growth. This mechanism will become important when the critical wavelength, Eq. (19), becomes comparable to or less than the mean pore spacing along the boundaries, i.e., $\lambda_c < s$. During sintering the spacing between pores grows as v decreases and as $\bar{G}$ increases by normal growth with pore coalescence. At the critical stage that the spacing exceeds λ_c the microstructure becomes unstable with respect to separation of the grain boundaries from the impurity cloud and from the pores. The ensuing secondary grain growth and pore entrapment may stop further sintering. Increasing the solute concentration will increase the resistance of the boundary to breakaway from the impurity cloud, Eq. (19), by increasing λ_c, as well as lowering M_b in the drag regime, Eq. (14). Additives in excess of the solubility limit may give lower values of s because of precipitate pinning as well as give maximum values of λ_c and minimum values of M_b all of which further stabilize the body to boundary-pore separation.

EXPERIMENTAL DETERMINATION OF MOBILITY

Grain boundary mobilities are plotted in Figs. D1, D7, and D8. Most of those for oxides were calculated from grain growth studies done on sintered or hot pressed samples. For all of the oxides γ was assumed to be 300 ergs/cm^2 which is generally within a factor of two of the true values. For the relatively infrequent cases of parabolic growth Eq. (37) was used. When the apparent n values were 3 or 4 the mobility was calculated from Eq. (39) which implies a grain size dependent mobility. To facilitate comparisons all these mobilities were normalized to that for a grain size of 90μm (equivalent to $F_t = 10^5$ dyne/cm^2). There were a few reports[1 10 13 59] of abnormal grain growth from which the mobility could be calculated from Eq. (32). The KCl mobilities were so measured in hot forged single crystals.[1]

DISCUSSION

Grain Boundary Mobilities

Many grain growth studies reported in the literature are by-products of sintering studies; thus these grain growth data are for porous samples. Even with fully dense samples, ceramic materials are likely to be contaminated with impurities which can significantly affect boundary mobility. Although there are very few studies in which the mobility has been quantitatively explained in terms of any model, order of magnitude comparisons show important differences. This is done more effectively by comparing the mobilities as a function of reciprocal homologous temperature $(T/Tm)^{-1}$, Figs. D7 and D8.

There are no definitive measurements of the intrinsic mobility in any ceramic for which D_b for the slow ion is also known. This would allow a test of the validity of the Turnbull expression, Eq. (1). The highest measured values of M in KCl give a value of M_o which is consistent with Eq. (1) using a reasonable estimate of D_b. In Fig. D8 estimates of M_o, Eq.(1), are also shown for oxides where wD_b is known for the cation. For UO_2, wD_b of U was measured by tracer diffusion.[60] The wD_b values for the slower cations were obtained from creep studies for Al_2O_3[61] and MgO.[9 62] For Al_2O_3 wD_b was not sensitive to MgO concentration; but for MgO the value is an average for pure and doped samples and the actual value may be mildly sensitive to additives such as Fe or F. To estimate D_b the width, w, was assumed to be of atomic dimensions based on recent arguments which discounted wide boundaries and space charge

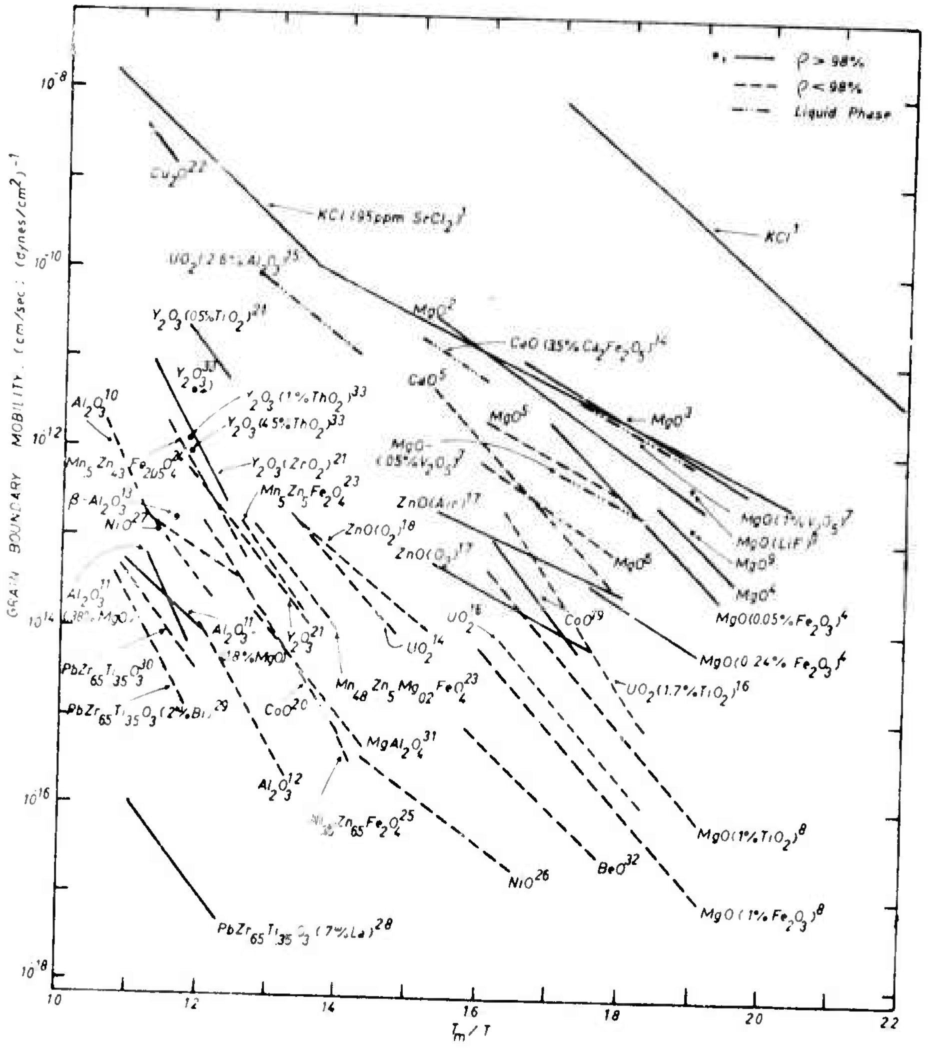

Figure D7. Grain boundary mobilities for oxides and halides as a function of reciprocal homologous temperature (Tm/T)$^{-1}$. The additive concentrations are in cation fraction unless otherwise noted.

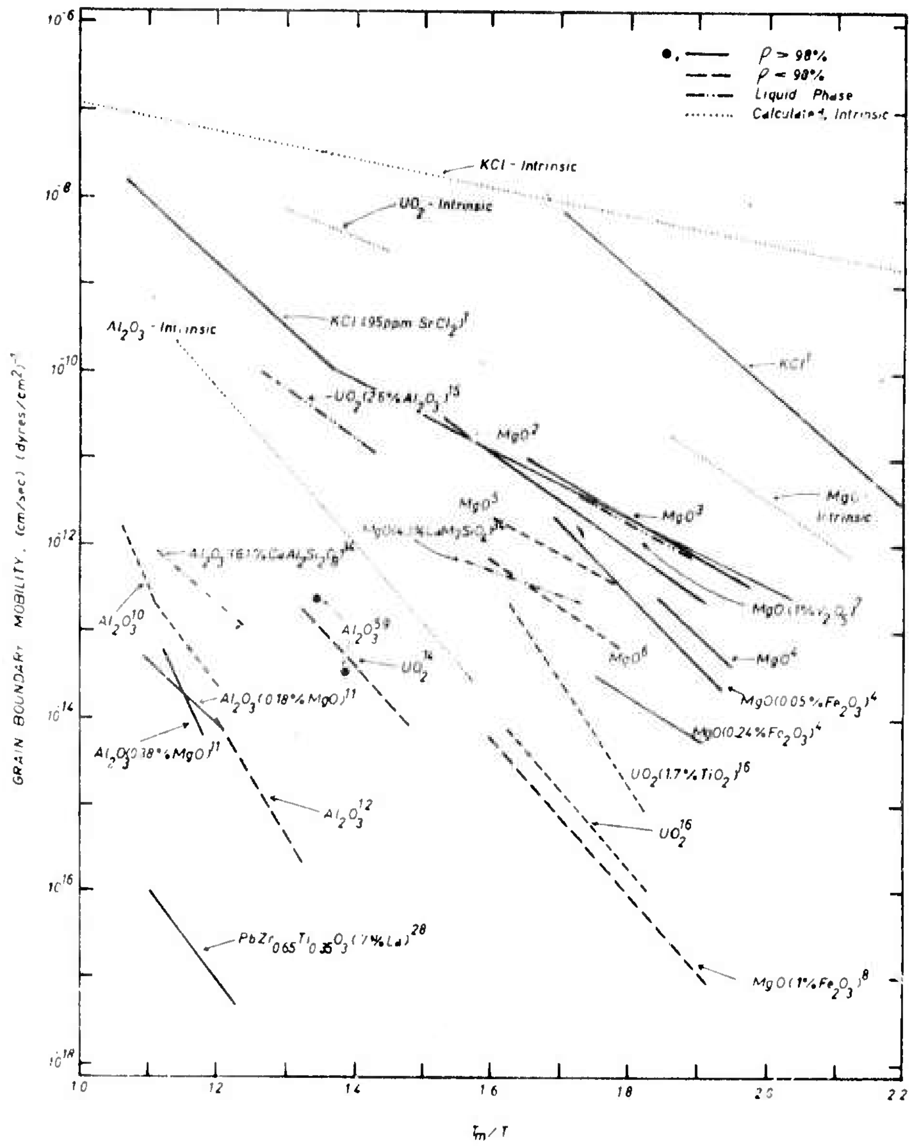

Figure D8. Selected grain boundary mobilities from Figure 7 compared with the calculated intrinsic mobility of KCl, UO_2, MgO and Al_2O_3.

contributions to wD_b.[46] The significant differences in M_o for different compounds with different crystal structures may be of theoretical interest. All of the measured mobilities for oxides are well below these estimates for M_o.

In general, the mobilities for porous samples are much lower than those for dense ones, e.g., 10^3-10^4 slower for MgO and CoO, which is consistent with particle coarsening or pore drag control. During sintering the porosity varies both in terms of the volume fraction and the topology. Gupta[63] and Samanta and Coble[64] have shown that a linear relationship frequently exists between density and grain size during intermediate stage sintering. Here the porosity is continuous and the densification and particle coarsening are obviously strongly interrelated. The coarsening may be limited by surface diffusion or vapor transport to the free surfaces or by densification rather than by grain boundary motion.[65]

Above about 85-95% density when the pores become isolated either normal or abnormal growth may be observed depending upon the size and distribution of pores and impurities. These grain growth rates are generally higher than the particle coarsening rates. For many of these the grain growth exponent n was reported to be 3 but there are reported results of $n = 2$ for porous samples of BeO,[32] CaO,[5] $MgAl_2O_4$,[31] NiO,[27] and UO_2[16] in which the mobilities were low. The value of n does not necessarily distinguish between grain growth models. In UO_2 grain growth with $n = 3$ and with pore growth and concurrent density loss, has been observed. It has been attributed to pore drag controlled by vapor transport with the pore growth caused by entrapped gases ($p = 2\gamma/r$) as well as coalescence.[49,66,14] For dense samples with second phase precipitates, such as MgO doped Al_2O_3,[11] the low mobilities are consistent with particle drag control.

It is suggested that the mobilities in most dense samples were impurity drag limited, although small amounts of porosity were sometimes important. For instance, in MgO parabolic growth was found in some undoped samples;[2,3] however, the mobilities are 20-100 times slower than M_o and the samples contained appreciable impurity ($\gg 100$ ppm) suggesting these are impurity drag limited. Additions of Fe_2O_3 or small amounts of porosity lead to $n = 3$ and further reductions of M.[9] In theoretically dense, hot pressed MgO high initial growth rates were found which decreased rapidly due to the development of small amounts ($< 1\%$) of porosity.[9,67]

The most compelling test of the impurity drag theory is for KCl in which Sr and Ca doping significantly reduces the mobility. This is the only ionic system in which the impurity drag has been explicitly calculated,[1,68] Fig. D5. The order of magnitude agreement is encouraging, but further refinements in the theory are necessary. In the absence of sufficient information to calculate α and β from Eqs. (10) and (11) the

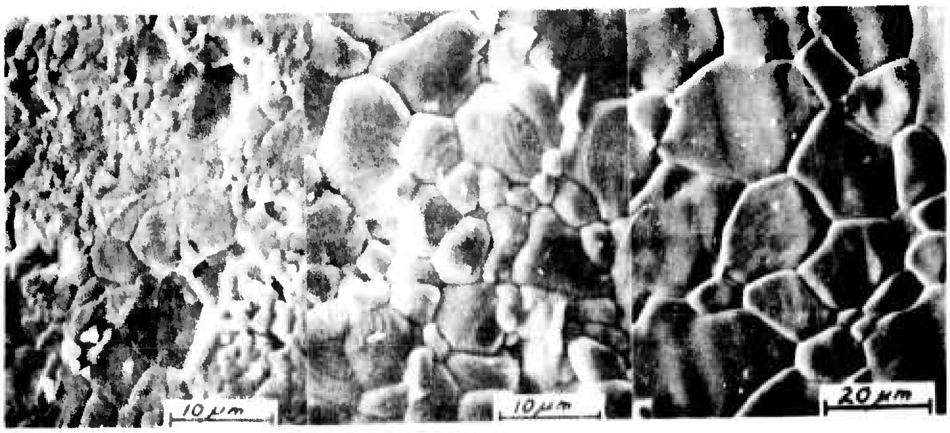

Figure D9. CoO after various amounts of grain growth showing the predominantly abnormal mode of growth with impingement to ultimately give a narrower distribution of grains; average density 99.3% (courtesy of U. Chowdhry).

the detailed time dependence cannot be expected to follow any simple $t^{1/n}$ law. The pattern of abnormal growth may be ultimately related to differences in porosity distribution caused by the agglomerate history of the starting powder.

The grain shapes observed in KCl during recrystallization provide an indication of the particular growth mode. The grains in Fig. D10(c) are thought to be growing in the impurity drag limited range and apparently do so rather uniformly. In contrast the straight sided grains seen by the authors, Fig. D 10(a), and others[70] in pure KCl result from rapidly moving boundaries at low temperatures which have broken away from the impurity cloud; these are thought to be moving essentially at the intrinsic velocity. The facets may be the result of anisotropy of M_0 as is predicted by the Gleiter,[38] model, Eq. (2) , where the atomic step density in the boundary and the mobility are lower for boundaries which are parallel to a low index plane in one grain. Finally, the very irregular grain, Fig. D10(b) is thought to have occurred because parts of the boundary had broken away from the impurity cloud by the fluctuation mechanism. Note the long fingers which can result from growth without spreading of one segment. Also note the regions of unrecrystallized material which is apparently entrapped between adjacent breakaway segments.

Straight sided grains frequently result from rapid secondary grain growth in the presence of a liquid phase; such straight grains, instead of cusped boundaries, resulting low velocity drag can only be estimated very crudely from[69]

$$M \approx \frac{\Omega}{kT} \frac{D_s}{2\delta\, C_\infty\, e^{Q/RT}} \qquad (40)$$

where D_s is the effective solute diffusivity (usually more like the lattice than boundary diffusivity), 2δ the width over which it is segregated, and Q the effective interaction energy. There are only a few studies in which the expected decrease in mobility with higher additive concentration is observed, e.g., MgO,[9] and Y_2O_3.[33] For instance in Y_2O_3 higher additions of ThO_2 were found to reduce growth rates,[33] but in another study[21] additions of TiO_2 or ZrO_2 increased the mobility relative to that in pure samples. This apparent increase in M may be due to combined effects of the additive on final density or pore mobility as well as on the solute diffusivity. In certain ranges of extrinsic behavior where $D_I = C_\infty D_{defect}$ the drag may be independent of the actual impurity concentration.[68] Frequently, various additives have been claimed to enhance secondary grain growth for reasons which are not known.

More complex solid solutions such as the ferrites and titanates have low mobilities even though in some cases (PLZT) the samples were single phase and theoretically dense ($v \ll 0.1\%$). This may be an indication of a low intrinsic mobility due to structural features resulting in few sites from which atoms can detach and jump across the boundary, e.g. Eq. (2).

When liquid phases are present the mobilities are higher than those for porous samples, but often not much higher than for dense samples. Lay[15] has shown satisfactory agreement between growth rates in UO_2 + 2.6% Al_2O_3, in which $n = 3$, and the order of magnitude predictions of the diffusivity and film thickness assuming control by diffusion in the liquid phase. When the liquid has a high dihedral angle and does not fully penetrate the grains the growth rates are slower.[34]

Microstructure

Very few grain growth studies in oxides fit simple parabolic kinetics, or even fit $\bar{G}^n = Kt$ over a significant range of $\bar{G}$. Microstructural examination of sintered materials indicates that one reason for this is that the growth is frequently not normal. In Fig.D9 the microstructure is shown after various amounts of grain growth for CoO samples for which the as-hot pressed grain size was 1.5μ.[20] The initially relatively uniform microstructure (not shown) evolved by secondary growth and after impingement approached a more normal distribution. Although the mobility can be estimated from such microstructures using Eq. (32) or Eq. (39),

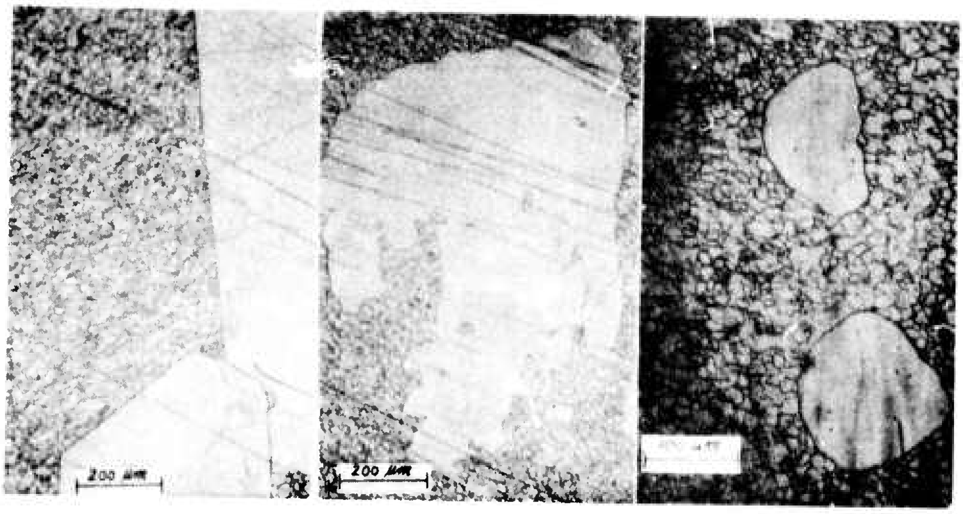

Figure D10. Various morphologies of recrystallized grains in forged and annealed KCl single crystals. The fine subgrains from the deformation do not grow.

from abnormal growthhave been claimed to be a test for the presence of a liquid phase. These idiomorphic grains in pure KCl indicate that there are other causes of straight sided boundaries.

The abnormal growth mode as well as other interesting features are seen in the microstructure of hot pressed and annealed Fe_3O_4,[71] Fig. D11. The large secondary grain on the left contains entrapped pores as are frequently observed, and also has an entrapped grain, A, perhaps similar in origin to those regions in Fig. D10 (b). In several places, particularly in the upper right, B and C, clusters of three pores can be seen. These are thought to result as pores at triple points are carried toward each other by a small shrinking grain as suggested by Kingery and Francois.[57] As the grain becomes small enough, and the curvature large enough, the driving force may be sufficiently large to cause separation before the pores meet and coalesce. Subsequent migration of the remaining boundaries or abnormal growth leaves these groups of pores isolated within grains. An example of a clover leaf shaped pore can also be seen, D, which apparently results fro several pores which have been carried together without separation but have not yet rounded. Other examples of pore coalescence can also be seen in the upper left. Finally, the ghost boundaries in the lower right show an array of pores, now trapped within a grain, which only shortly before were on grain boundaries.

SUMMARY

Models for the grain boundary mobility in ceramics are

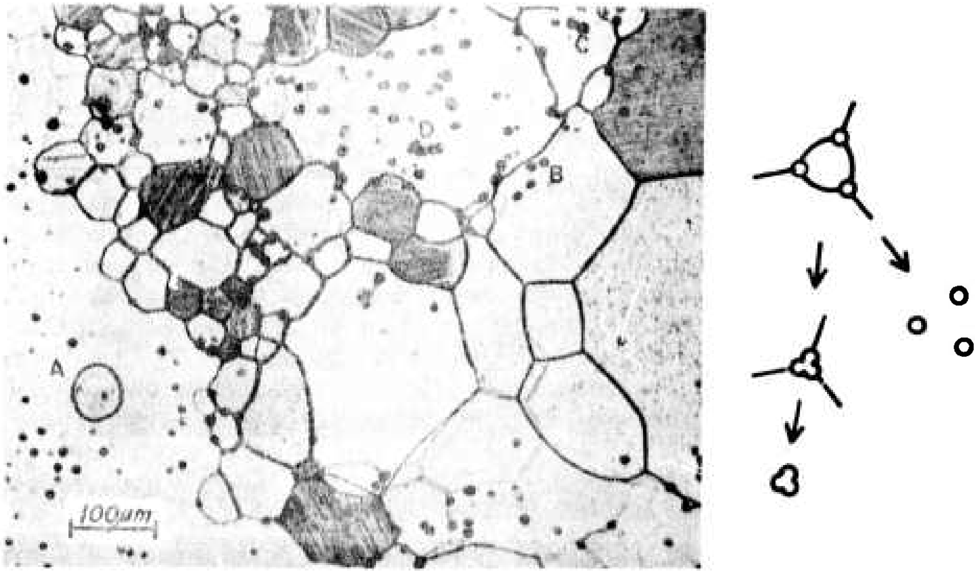

Figure D11. Hot pressed and annealed Fe_3O_4 which shows entrapped pores, some in non-random arrays, an entrapped grain, and predominantly abnormal growth; sample density 99.6% (courtesy of J. Halloran).

discussed for the cases of control by the intrinsic mobility, by drag of solute atoms, by drag of pores or particles, and for diffusion through a liquid film. The conditions for which the different mechanisms are operative have been indicated. Over wide ranges of driving force a boundary may be drag limited and move at a low speed or if separated from the solute cloud or pore it may move much faster. A simplified mechanism for breakaway from the impurity cloud is presented and the possibility of cooperative separation from impurities and pores is discussed.

Grain growth kinetics vary for different migration mechanisms. The multivalued aspect of the mobility can lead to complex growth kinetics including decaying growth rates caused by a transition in the limiting mechanism. The conditions for abnormal growth, with or without pore entrappment, are also affected by such transitions. This is of obvious importance in sintering as prevention of separation of boundaries from pores is important if dense, uniform microstructures are to be produced.

There are very few measurements of the boundary mobility in ceramics which unambiguously show the distinction between solute and second phase effects or which provide a quantitative confirmation of any of the mobility or grain growth models. From a comparison of the trends in the data with the models and from examination of microstructures it is concluded that

(1) The best confirmation of the solute grag theory arises from the agreement between mobility calculations for Sr doped KCl using a model incorporating electrostatic and strain energy interactions with experimental measurements in pore free samples.

(2) An upper bound estimate of the intrinsic mobility, using the Turnbull model, is much larger than observed boundary mobilities even in nominally pure and dense oxies. The lower velocities may be caused by impurity drag. The only data which appear to approach intrinsic velocities are from alkali halides.

(3) Consideration of the specific data for oxides suggests that:

(a) pores or particles generally exert a larger drag force than solute drag, particularly when the porosity is high as during sintering.

(b) the presence of a liquid film can give relatively high rates of grain growth.

(c) the boundary mobility in materials with simple structures and compositions is higher than that for more complex materials, e.g., MgO vs. PLZT or ferrites.

(4) The shape of grains can be affected by the controlling mechanism, e.g., faceted grains may result from growth at the intrinsic mobility or from liquid phase controlled growth particularly if it is interface reaction controlled. Transitions between solute drag and intrinsic control can cause very irregularly shaped grains.

(5) During grain growth the actual motion of boundaries is irregular. This results in part from the grain size dependent, spacial variations in the driving force. Thus, the boundaries of small and large grains have higher velocities. Transitions between mobility mechanisms can also cause jerky boundary motion.

REFERENCES

1. M. F. Yan, "Grain Boundary Mobility of KCl", Sc.D. Thesis, Dept. Mat. Sci. & Eng., M.I.T., 1976.
2. R. M. Spriggs, L. A. Brissette and T. Vasilos, J. Am. Ceram. Soc. 47, 417 (1964).
3. C. M. Kapadia and M. H. Leipold, ibid., 57, 41 (1974).
4. R. S. Gordon, D. D. Marchant and G. W. Hollenberg, ibid., 53, 399 (1970).
5. A. V. Daniels, Jr., R. C. Lowrie, Jr., R. L. Gibby and I. B. Cutler, ibid., 45, 282 (1962).
6. T. K. Gupta, J. Mat. Sci. 6, 25 (1971).
7. G. C. Nickolson, J. Am. Ceram. Soc., 48, 525 (1965).
8. G. C. Nickolson, ibid., 49, 47 (1966).
9. R. S. Gordon, U. of Utah, Salt Lake City, private communications, (1976).
10. R. E. Mistler, "Grain Boundary Diffusion, Widths and Migration Kinetics in Al_2O_3, NaCl, and Ag", Sc.D. Thesis, Dept. Mat. Sci. & Eng., M.I.T. (1967).
11. A. Mocellin and W. D. Kingery, J. Am. Ceram. Soc. 56, 309 (1973).
12. R. L. Coble, J. Appl. Phys. 32, 793 (1961).
13. U. Chowdhry and R. M. Cannon, unpublished research, M.I.T. (1976).
14. R. N. Singh, submitted to J. Nucl. Mat. (1976).
15. K. W. Lay, J. Am. Ceram. Soc. 51, 373 (1968).
16. I. Amato, R. L. Colombo, A. Petruccioli Balzari, J. Nucl. Mat. 18, 252 (1966).
17. S. K. Dutta and R. M. Spriggs, J. Am. Ceram. Soc. 53, 61 (1970).
18. T. K. Gupta and R. L. Coble, ibid., 51, 521 (1968).
19. U. Chowdhry, unpublished research, M.I.T. (1975).
20. P. Kumar and D. [illegible] Johnson, J. Am. Ceram. Soc., 57, 65 (1974).
21. J. C. Wurst, Ph.D. Thesis, U. Illinois, Urbana-Champaign, (1971).
22. I. Zikovsky, G. Vangard and J. S. Daniel, J. Am. Ceram. Soc., 55, 134 (1972).
23. T. Iimura, Ferrites: Proc. Int. Conf., 128, Japan (1970).
24. G. C. Jain, B. K. Das and N. C. Goel, Indian J. Pure & Appl. Phys., 14, 87 (1976).
25. H. L. Turk, Ferrites: Proc. Int. Conf., 99, Japan (1970).
26. K. Uematsu, Ph.D. Thesis, Dept. Mat. Sci. & Eng., M.I.T. (1976).
27. Y. Iida, J. Am. Ceram. Soc., 41, 297 (1958).
28. R.A. Langman and R. B. Runk, ibid., 56, 486 (1973).
29. G. H. Haertling, ibid., 49, 113 (1966).
30. R. B. Atkin and R. M. Fulrath, ibid., 54, 265 (1971).
31. R. J. Bratton, ibid., 54, 141 (1971).

32. T. E. Clare, ibid., 49, 159 (1966).
33. P. J. Jorgensen and R. C. Anderson, ibid., 50, 553 (1967).
34. D. S. Buist, et al., Trans. Brit. Ceram. Soc., 64, 173 (1965).
35. W. D. Kingery, J. Am. Ceram. Soc., 57, 1, 74 (1974).
36. D. Turbull, Trans. A.I.M.E., 191, 661 (1951).
37. W. D. Kingery, H. K. Bowen and D. R. Uhlmann, Introduction to Ceramics, Wiley, Ch. 8, (1976).
38. H. Gleiter, Acta. Met., 17, 853 (1969).
39. J. W. Cahn, ibid., 10, 789 (1962).
40. K. Lucke and H. P. Stuwe, "On the Theory of Grain Boundary Motion", in Recovery and Recrystallization of Metals, ed. L. Himmel, Gordon and Breach, N.Y., p. 171 (1963).
41. M. Hillert and B. Sundman, Acta. Met., 24, 731 (1976).
42. J. Frenkel, "Kinetic Theory of Liquids", Oxford U. Press, N. Y. (1946).
43. K. Lehovec, J. Chem. Phys., 21, 1123 (1953).
44. J. Eshelby, et al., Phil. Mag., 8, 75 (1958).
45. K. L. Kliewer and J. S. Koehler, Phys. Rev., 140 (4A), 1226 (1965).
46. M. F. Yan, R. M. Cannon. H. K. Bowen and R. L. Coble, J. Am. Ceram. Soc., 60, (1977)
47. A. Roy and C. L. Bauer, Acta. Met., 23, 957 (1975).
48. P. G. Shewmon, Trans. A.I.M.E., 230, 1134 (1964).
49. F. A. Nichols, J. Appl. Phys., 37, 4599 (1966).
50. M. F. Ashby and R. M. A. Centamore, Acta. Met., 16, 1081 (1968).
51. R. J. Brook. J. Am. Ceram. Soc., 52, 56 (1969).
52. G. W. Greenwood, Acta. Met., 4, 243 (1956).
53. C. Wagner, Z. Electrochemie, 65, 581 (1961).
54. E. E. Underwood, "Quantitative Stereology, Addison-Wesley, Reading, Mass. (1970).
55. M. Hillert, Acta. Met., 13, 227 (1965).
56. C. Zener, Private Communication to C. S. Smith, Trans. A.I.M.E., 175, 15 (1949).
57. W. D. Kingery and B. Francois, "The Sintering of Crystalline Oxides,I. Interactions Between Grain Boundaries and Pores", in Sintering and Related Phenomena, ed., G. C. Kuczynski, et al., Gordon and Breach, p. 471 (1967).
58. R. J. Brook, Scripta Met., 2, 375 (1968).
59. W. H. Rhodes, P. F. Jahn and P. L. Burnett, "Microstructure Studies of Polycrystalline Oxides", Summary Report, Contract N00019-68-C-0108, (25 May, 1968—24 June, 1969).
60. S. Yajima, H. Furuya and T. Hirai, J. Nucl. Mat., 20, 162 (1966).
61. R. M. Cannon and R. L. Coble, "Review of Diffusional Creep of Al_2O_3", in Deformation of Ceramic Materials, ed. R. C. Bradt and R. E. Tressler, Plenum Press, N.Y., p. 61, (1975).

62. P. A. Lessing and R. S. Gordon, "Impurity and Grain Size Effects on the Creep of Polycrystalline Magnesia and Alumina", ibid., p. 271.
63. T. K. Gupta, J. Am. Ceram. Soc., 55, 276 (1972).
64. S. C. Samanta and R. L. Coble, ibid., p. 583.
65. C. Greskovich and K. W. Lay, ibid., p. 142.
66. F. A. Nichols, ibid., 51, 468 (1968).
67. W. H. Rhodes, B. J. Wuensch and T. Vasilos, "Relation Between Particalate Chemistry and Ceramic Properties", Final Report, Contract N00014-70-C-0138, AVCO Corp., (1 Jan. 1970-31 Dec. 1972).
68. M. F. Yan, et al., "Grain Boundaries and Grain Boundary Mobility in Hot-Forged Alkali Halides, in Ref. 61, p. 549.
69. K. Lucke and K. Detert, Acta. Met., 5, 628 (1957).
70. B. G. Koepke, et al., J. Appl. Phys., 45, 969 (1974).
71. J. W. Halloran, "Iron Diffusion in Iron Aluminate Spinels", Ph.D. Thesis, Dept. Mat. Sci. & Eng., M.I.T. (1977).

E. HOT FORGING OF CaF_2

E.1. Introduction:

Of the various classes of materials, the alkaline earth halides have among the lowest absorption in the IR spectrum. This makes them a candidate material for use in the CO laser. The mechanical properties of these materials has become a limiting factor in their utilization in high power laser systems.

Hot forging of single crystals of alkali halides has proved to be successful in improving mechanical properties without degrading optical properties. As a result, deformation, subgrain formation, and recrystallization behavior has been studied in such alkali halides as KCl, KBr, AgCl, and NaCl. Data of this nature for alkaline earth halides is at best sparse. It was the objective of this work to determine this information for CaF_2.

E.2. Materials:

Single crystals of CaF_2 were purchased from two vendors. All crystals were in the shape of right circular cylinders with a height to diameter ratio of 1 to 1. All crystals purchased from Harshaw Chemical Co. were "pure" and unoriented. Two sets of crystals were purchased from Optovac; a) pure,oriented (<100>, <110>, and <111>) and b) doped, oriented (100 ppm Gd, <110>).

E.3. Experimental Procedure:

All samples were heated and subsequently deformed under vacuum. A graphite die was used for all runs. Grafoil[1] was used to reduce friction between the sample and die piston. An internal pressure of less than 10μ was maintained. Samples were heated at a maximum rate of 200°C/hr and allowed to soak at forging temperature for at least 30 minutes to minimize temperature gradients within the sample.

---

(1) Union Carbide pyrolitic graphite foil, 0.01 inches thick.

Samples were deformed at a constant true strain rate of $0.034 \pm .003$ min^{-1} for a total of 15 min. Ram displacement and load readings were taken at one minute intervals and converted to true strain and true stress, respectively, using previously reported procedures, Yan et al. (1975a,b). Samples were either hot ejected (∿3 minutes) or the sample and die were allowed to cool to room temperature (5-10 hrs.).

Samples were mounted and polished to a 1μ finish using diamond paste. This was followed by .3 and .06μ alumina. A thirty minute hand lapping on the .06μ alumina was found to greatly improve the surface condition.

Several etches were tried including concentrated H_2SO_4, and $HClO_4$ and hot aqueous solutions of NH_4Cl. The best etching behavior was obtained from a solution of 50 ml HCl + 20g NH_4Cl + 20g $AlCl_3$ in 100 ml H_2O at 70°C or from hot or cold concentrated HCl. Most samples were etched in concentrated (fresh) hydrochloric acid at room temperature for 20-30 minutes. Microstructures were examined and the mean linear intercept determined.

E.4. Results:

E.4.1. Stress Strain Behavior

Stress strain curves were constructed for each sample. Upon comparison several trends were observed. First, after some amount of strain, the stress approached a constant (steady state) value varying between several hundred to over eleven thousand psi depending upon the temperature of the run and orientation of the crystal. Both the amount of strain to reach steady state and the magnitude of the steady state flow stress were found to decrease with increasing temperature. At temperatures close to $0.5T_m$ a strain of the order of 40% was necessary to achieve a constant stress condition. At $T = 0.8T_m$ a strain of 20% was sufficient, the necessary strain continuing to decrease as T increased. Figure E1 illustrates these trends.

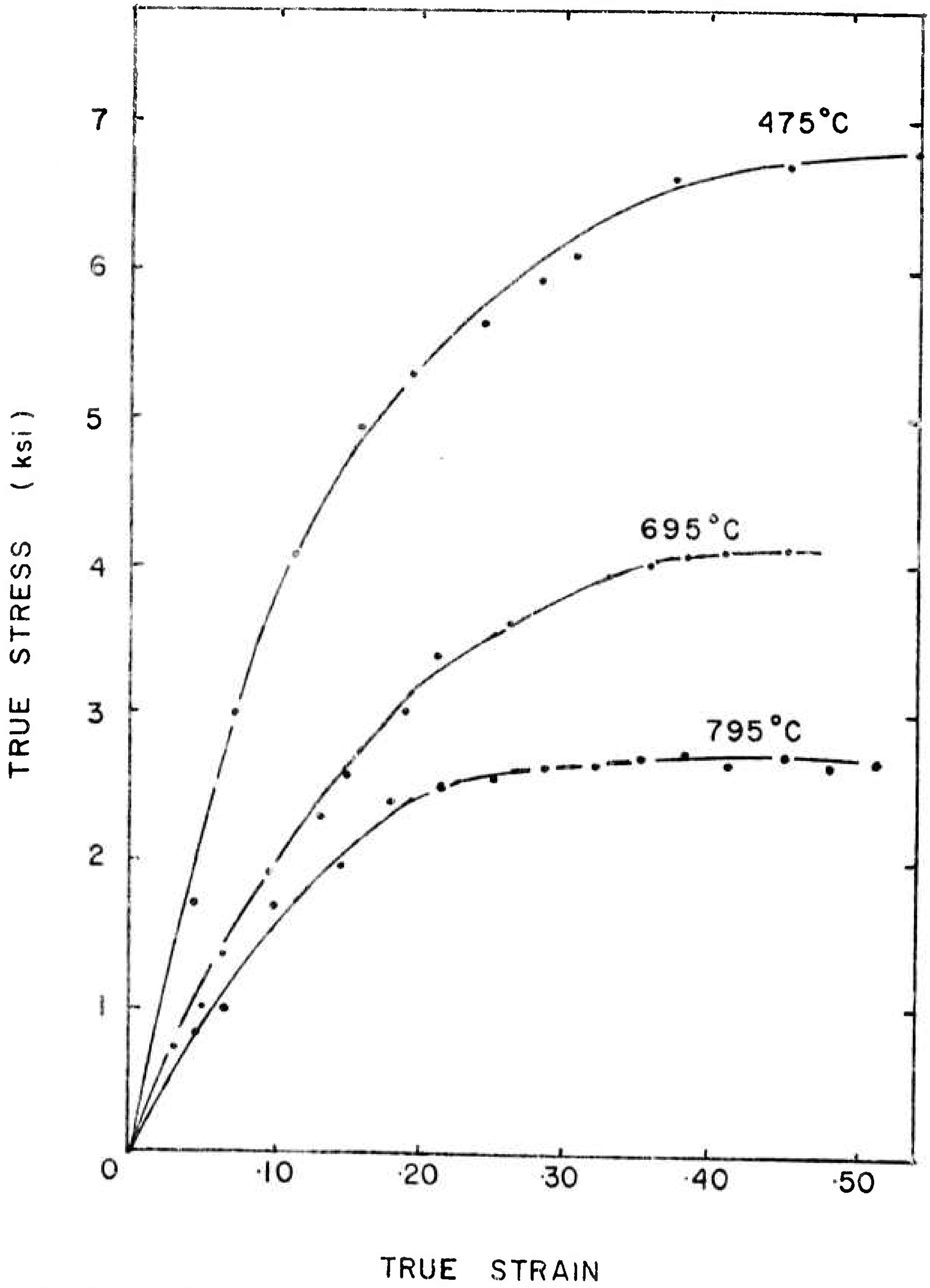

Figure E1. Representative stress strain curves for forged CaF_2.

For $T \gtrsim 0.65T_m$ the variation in steady state flow stress due to orientation was too small to be observable. The flow stress behavior of undoped oriented and unoriented crystals above $0.65T_m$ could easily be described by a single line, Figure E2. At $T \leq 0.65T_m$ the steady state flow stress behavior was orientation dependent. For any temperature within this regime it was found that $\sigma_{<100>} > \sigma_{<110>} > \sigma_{<111>}$. Extrapolation would suggest that the flow stress behavior for the various orientations is converging to a single line at $T \approx 0.45\ T_m$. Experimental verification of this is considered unlikely at the strain rates used in our experiments. It was found on several occasions that samples forged at $T < 0.5\ T_m$ shattered or cracked during forging. Prior to the forging of oriented crystals a certain amount of scatter in σ_f forging stress had been observed on unoriented crystals at lower temperatures, Bowen et al (1976). If one anticipates the values of σ for unoriented crystals to fall somewhere between the two extremes of the oriented crystals, the "scatter" is easily explained.

A limited amount of work was done on doped (100 ppm Gd) oriented <110> crystals. The flow stress was found to deviate rather considerably, but erratically from the values for undoped <110> crystals. At some temperatures σ was increased by as much as a factor of 3 at others there was a much smaller effect. All doped samples tested had higher flow stresses than equivalent undoped crystals indicating that there was some amount of dopant in all crystals. Our supposition is that the inconsistency in the flow stress behavior was to a large part controlled by an inhomogeneous dopant concentration from sample to sample.

E.4.2. Subgrains:

Subgrain formation occurred during the forging of all samples. The subgrain size decreased with increasing stress

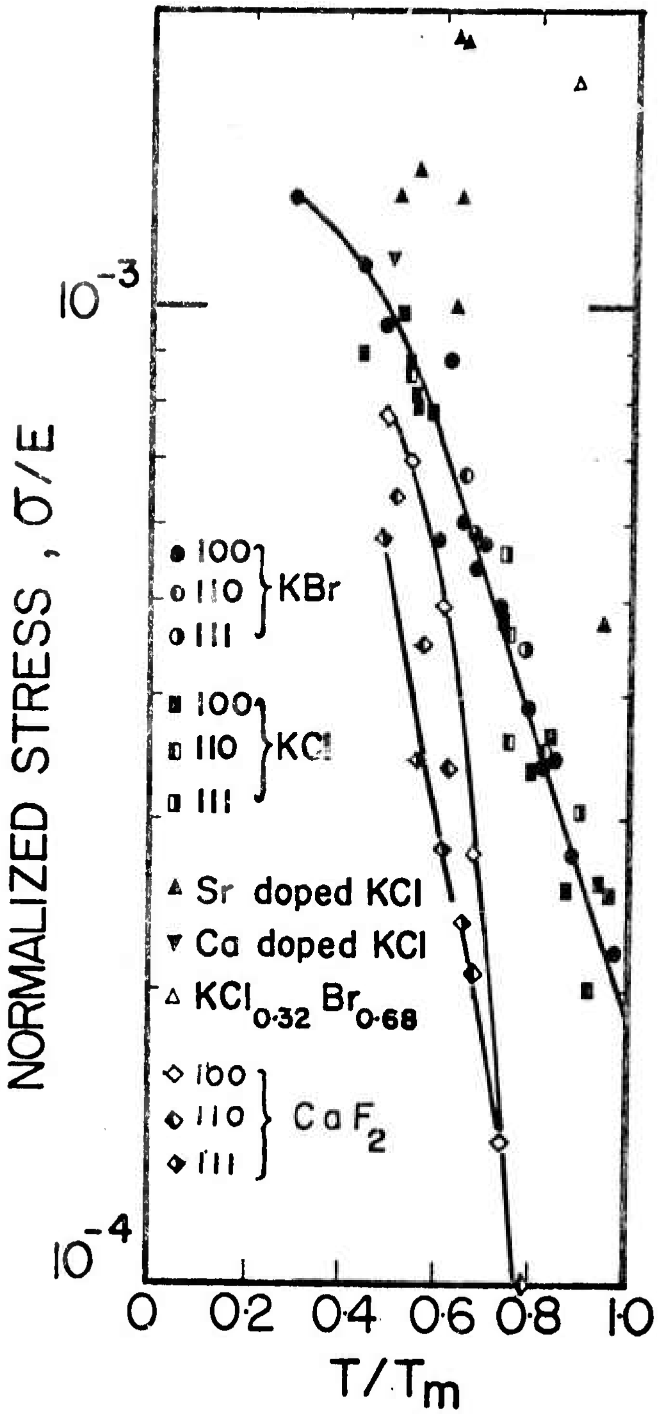

Figure E2. Normalized steady state flow stress vs. homologous temperature for CaF_2. Previous results for KCl and KBr are shown for comparison, Yan et al. (1975b). (T_m for CaF_2 is 1630°K).

(decreasing temperature). The results of TEM work (see section F) indicate that the subgrain boundaries are low angle. The subgrain boundaries appeared to become more diffuse as the temperature decreased (σ increased). The combination of increasing boundary width and the decreasing subgrain size made optical microscopy of some samples extremely difficult.

In the course of our investigation many samples were polished, etched, and examined. In our work on unoriented crystals there seemed to exist a sample to sample variation in the details of the microstructure, Bowen et al (1976,1977). The work on oriented single crystals suggests that the uniformity of the microstructure, the shape of the subgrains developed, and the susceptibility to cracking are orientation dependent.

Crystals with a <100> orientation were forged at temperatures ranging from 0.48 to 0.74 T_m. All samples were removed from the die free of optically detectable cracks. Only the sample forged at 0.48 T_m cracked during subsequent polishing and handling. The fracture was transgranular in nature. As the forging temperature was decreased the sample shape tended to be more blocky. Samples forged at 0.74 (940°C), 0.66 (800°C) and 0.60 T_m (700°C) displayed equiaxed grains which were uniform both in size and distribution, Figure E3. There was some evidence of recrystallization in the sample forged at 0.74 T_m. Occasionally a subgrain was observed which was perhaps a factor of ten larger than the average. The interior of these larger subgrains were free of etch pits whereas the matrix was not. The samples forged at 0.54 (630°C) and 0.48 T_m (510°C) showed evidence of localized strain and a greater variation in the subgrain size about the average. In the bandy regions some subgrains appeared to be nearly rectangular. Parallel bands of subgrains with subgrain free regions between them were observed in both samples. The fraction of the sample which

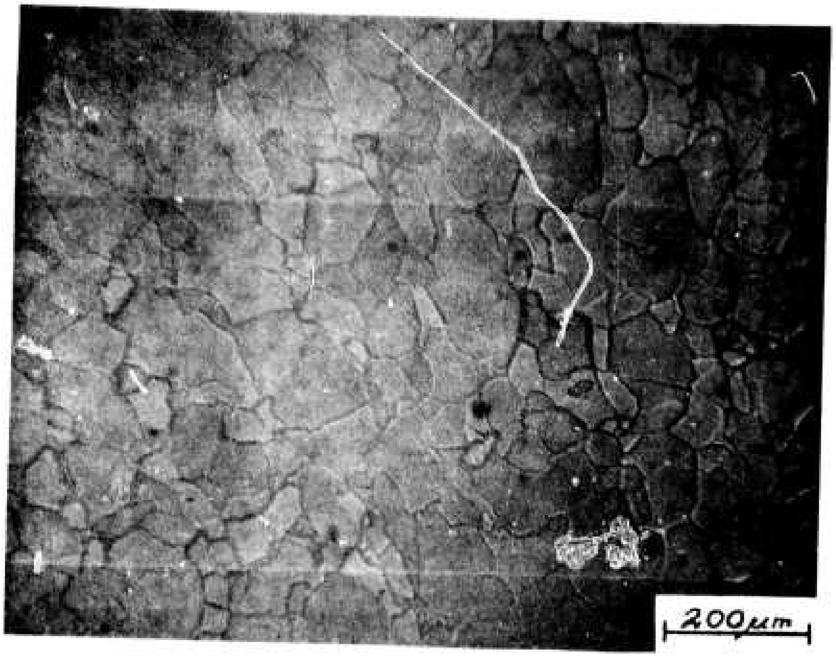

Figure E3. Subgrains in <100> sample forged at 0.74 T_m (940°C).

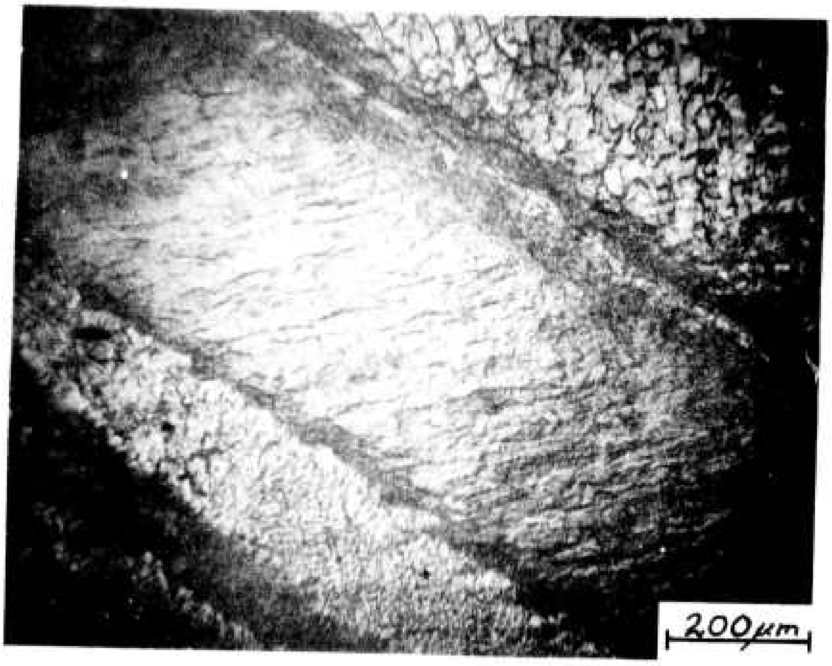

Figure E4. Inhomogeneous microstructure in <111> sample forged at 0.56 T_m (640°C).

was subgrain-free increased as the temperature decreased.

Forgings of <111> crystals were conducted at temperatures ranging from 0.49 (530°C) to 0.66 (800°C) T_m. All but the sample forged at 0.66 T_m underwent fracture either during polishing (0.56 and 0.61T_m) or during forging (0.49 T_m). Crystals of <111> orientation were found to be the most susceptible to cracking.

The microstructures of samples forged at 0.66 (800°C), 0.61 (720°C) and 0.56 (640°C) T_m were examined. The microstructure in each case was inhomogeneous. There were limited regions in which subgrains of uniform size were observed, Figure E4. Within these regions there was a tendency for the grains to be elongated. The most prominent microstructural features were bands within which the structure was poorly defined and kink bands. As the forging temperature was decreased the grains tended to become more elongated, the extent of "banding" and the areal fraction with poorly developed subgrains increased.

Forgings of <110> crystals were conducted at temperatures ranging from 0.51 to 0.78 T_m. All forgings were found to be crack free upon removal from the die. Microstructures were not examined.

E.4.3. Subgrain-Subcell-Flow Stress Correlation

Generally in the creep literature the subgrain size is correlated to the flow stress. In many metal systems it is observed that the subgrain size is inversely proportional to σ. A similar correlation was sought in the CaF_2 system.

During the earlier portion of our program the majority of our work was on unoriented crystals. It was observed that the "subgrain" size was inversely proportional to σ^2, Bowen, et al. (1976),Cannon, et al. (1976). There was also an unsatisfying amount of scatter in the data. We believe that our work on oriented crystals and the results of TEM work offer a plausible explanation.

In attempting to obtain a correlation between subgrain size and σ it is desirable to have a uniform microstructure. When confronted with inhomogeneous microstructures such as those observed in <111> crystals of CaF_2 it is not clear how the "average" subgrain size, $\bar{D}$, should be defined. If one includes the inhomogeneities the value of $\bar{D}$ becomes dependent upon the degree of inhomogeneity. If one excludes the inhomogeneities and correlates $\bar{D}$ to σ one must assume that the homogeneity of the sample does not significantly influence the magnitude of σ_f. These problems are made worse if appreciable dynamic recrystallization occurs. In light of these considerations it was felt that the most meaningful correlation would be obtained from measurements on <100> crystals.

When etch pits were observed they were generally confined to the interior of subgrains. Although in some areas of the samples the arrangement of etch pits appeared to be random, in a substantial fraction of the area the etch pits formed cellular networks, Figure E5. There were <u>two</u> distinct microstructural elements present in the samples. The cellular units, whose boundaries were defined by discrete etch pits are referred to in this paper as subcells, and their mean linear intercept (subcell size) designated by $\bar{d}$. Those boundaries which were not resolvable into etch pits and hence appeared to be continuous are referred to as subgrain boundaries. The subgrain size is designated by $\bar{D}$.

The subgrain size was found to be inversely proportional to the stress the magnitude of $\bar{D}$ ranging from 10 to 60μ. The subcell size was found to vary between 4 and 28μ. In the course of TEM work on our unoriented specimens, Sherry and Vander Sande, Section F measured cell sizes. Their data is included and complements our measurements.

In several samples with a <111> orientation subgrains and subcells were observed. The subcells were not as clearly

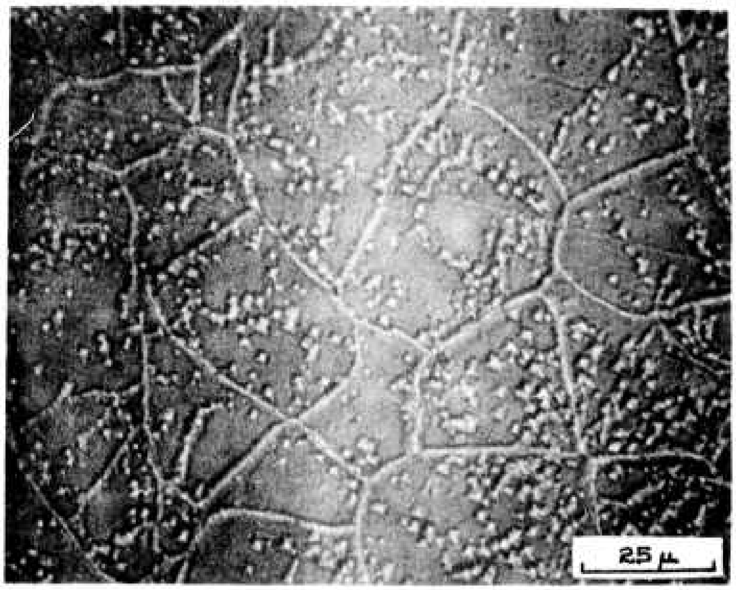

Figure E5. Cellular arrays of etch pits with subgrains in CaF_2 sample forged at 0.65 (795°C).

defined as in <100> forgings and an accurate measurement of $\bar{d}$ was not obtainable. The subgrain size in <111> forgings was smaller than those in <100> forgings of comparable stress. This may be the result of the microstructural inhomogeieity observed in <111> forgings.

The subcell size and subgrain size determine a band on a log $\bar{D}(\bar{d})$ vs. log σ plot, Figure E6. Nearly all our earlier data falls within this band. Our data most likely represents a mixture of subcell and subgrain size. This may be due to our use of an etchant which did not preferentially etch dislocations.

The reasons for the difference in subcell and subgrain etching behavior are not clear. We assume that there must be an energy difference which accounts for the difference. The subgrain boundaries perhaps correspond to a higher misorientation angle and hence a smaller dislocation spacing in the boundary. TEM measurements on misorientation angles by means of spot splitting have shown that θ can vary substantially within a given sample. Within some samples a nearly bimodal distribution was observed, Table I. A problem arises with this interpretation when one compares the TEM values of misorientation angle for subcells (presumably the $\sim 0.3°$ values) with those determined from etch pit spacing. Based on etch pit spacing one predicts a misorientation of the order of 0.01°. The possibility exists that the pits correspond to dislocations which have not yet been accomodated into the boundary. These extrinsic dislocations may have a higher energy than the knitted boundary dislocations. As the energy of the boundary increases with increasing θ, subgrain boundaries may etch without the presence of extrinsic dislocations. Alternatively the etching of individual dislocations may depend critically on the angle of intersection of the dislocation with the surface.

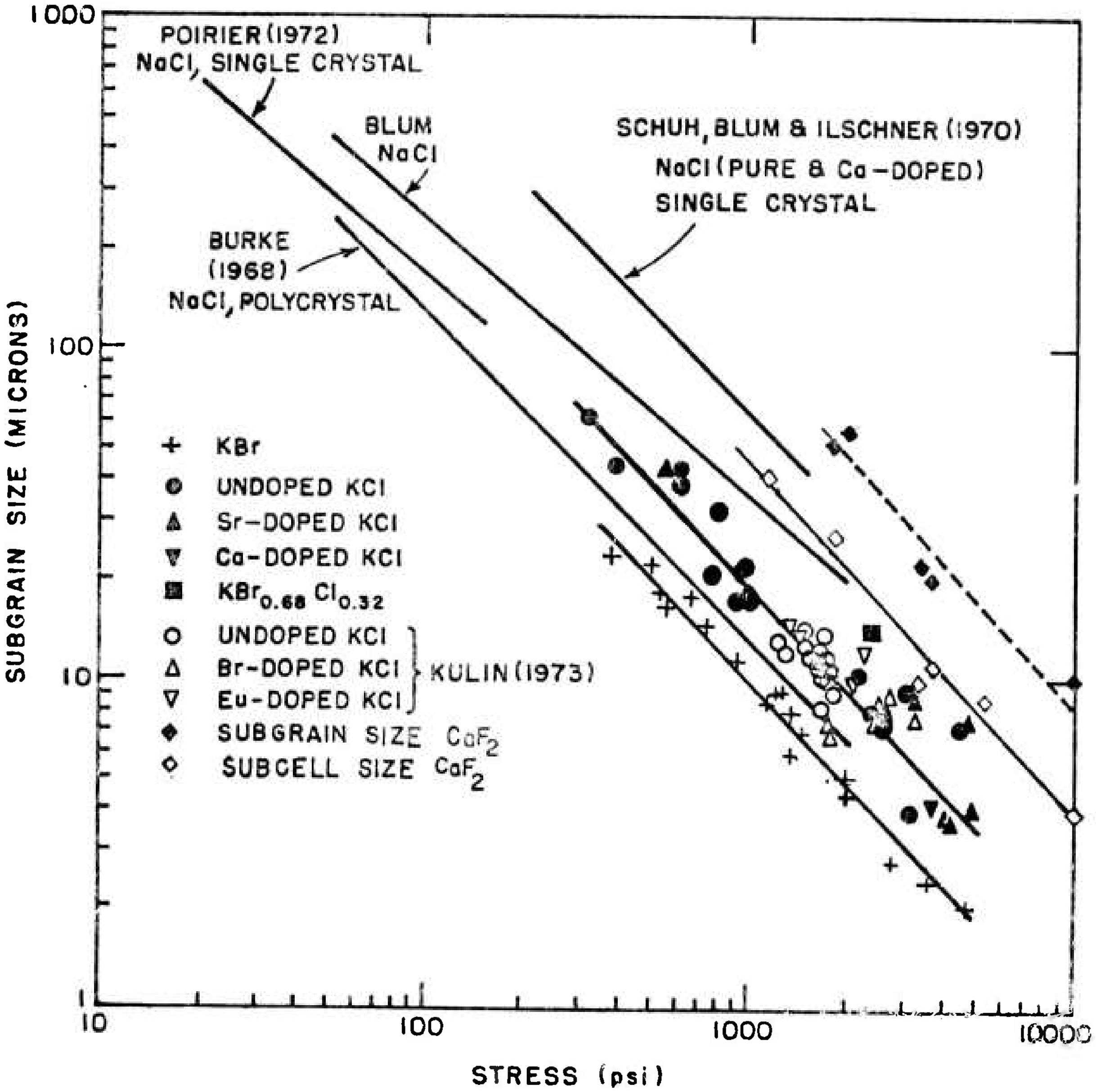

Figure E6. Plot of subgrain or subcell size vs. forging stress for CaF_2. Previous data on alkali halides, Yan et al., (1975a,b) and data from the literature are included for comparison.

TABLE I

Sub-boundary Misorientation Angle

Temperature	Misorientation Angle, Degrees		Mean
590°C	0.374	1.206	1.07
	0.695	1.273	
	0.781	1.302	
	0.955	1.507	
	1.042	1.507	
	1.074		
702°C	0.318	1.145	1.042
	0.465	1.309	
	0.478	3.55	
	0.786	4.010	
817°C	0.310	1.528	1.563
	0.337	1.637	
	0.674	1.763	
		2.191	
907°C	0.419	1.055	0.955
	0.441	1.066	
	0.559	1.146	
	0.637	1.273	
	0.800	1.302	
	0.819	1.375	
		1.432	

E.4.4. Recrystallization

The microstructure of samples forged at temperatures in excess of 0.65 T_m showed increasing evidence of recrystallization as the temperature was increased. At temperatures close to 0.65 T_m the evidence was limited. One occasionally observed larger than average subgrains outlined by a boundary which appeared to have a higher than average misorientation angle. These "nuclei" became more frequent as the forging temperature increased. This behavior is illustrated in Fig. E7. The presence of poorly defined subgrain boundaries within the large grain suggests that recrystallization occurred during forging. At $T \geq 0.79 T_m$ regions with well defined subgrains became increasingly sparse. These regions were limited to the edges of the forged samples, Fig.E8. It is thought that the tendency at higher temperatures to reach apparent steady state at lower strains may be related to the considerable amount of dynamic recrystallization. The few samples which were Gd^{+3} doped did not appear qualitatively different in the tendency for dynamic recrystallization.

At $T \gtrsim 0.8 T_m$ samples became opaque after forging. This is thought to be the result of CaO formation on cooling as a result of O contamination. As a result of the extensive recrystallization at high temperature no attempt was made to eliminate this problem.

E.4.5. Thermal Shock

One of the problems which is likely to be encountered in materials which have poor thermal conductivity coupled with large thermal contraction is quench cracking. Unoriented samples which were forged and hot ejected tended to crack. There appeared to be a temperature range ($\sim 0.68\ T_m$ - $\sim 0.81\ T_m$) over which samples did not crack due to hot ejection. In light of the variability between <100> and <111> in their tendency to crack during polishing we suspect that this may have been caused by orientation variations.

Figure E7. Recrystallized grains in CaF_2 sample forged at 0.79 T_m (1018°C).

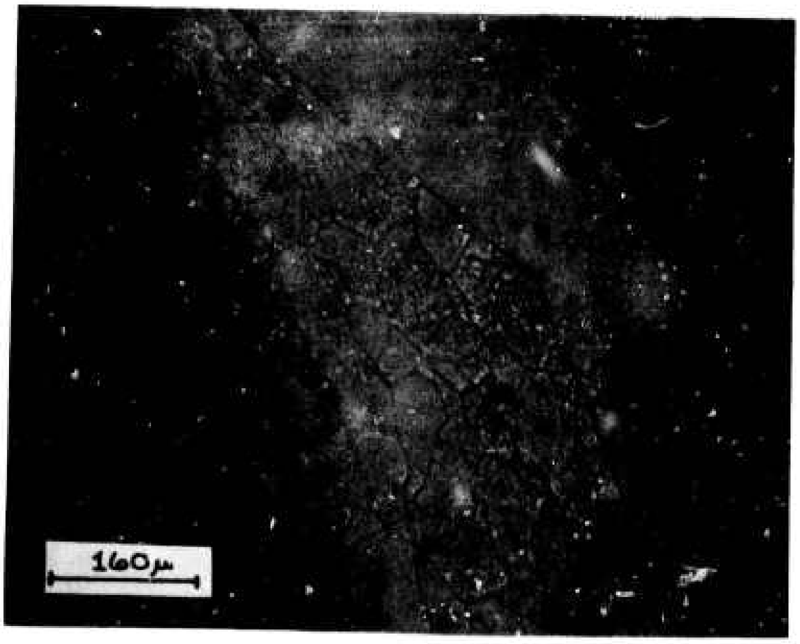

Figure E8. Sample forged at 0.79 T_m (1018°C) showing well developed subgrains only near the sample surface.

E.5. References:

Blum, W. (1973) data in Streb, G. and Reppich, B. (1973), Phys. Stat. Sol. (2), 16, 493.

H.K. Bowen, et al. (1976), Research on Materials for High Power Laser Windows, Semi-Annual Technical Report - No. 2, RADC-TR-76-348.

H.K. Bowen, et al, (1977), Research on Materials for High Power Laser Windows, Semi-Annual Technical Report - No. 3, RADC-TR-77-227.

P.M. Burke, (1968), "High Temperature Creep of Polycrystalline Sodium Chloride", Ph.D Thesis, Stanford Univ.

R.M. Cannon, et al. (1976), "Fabrication and Properties of Laser Window Materials" in Laser Induced Damage in Optical Materials: 1976, ed., A.J. Glass and A.H. Guenther, NBS Special Publication 462.

S.A. Kulin, P.P. Neshe, and K. Keder, (1974) "Development of Polycrystalline Alkali Halides by Strain Recrystallization for Use as High Energy Infrared Laser Windows", Technical Report AFML-TR-74-17., Man Labs., Inc.

J.P. Poirier, (1972), Phil. Mag. <u>26</u>, 713.

F. Schuh, W. Blum, and B. Illschner, (1970), Proc. of Brit. Ceram. Soc., No. 15, 143.

M.F. Yan, R.M. Cannon, H.K. Bowen and R.L. Coble (1975a), "Grain Boundaries and Grain Boundary Mobility in Hot Forged Alkali Halides", in Deformation of Ceramic Materials, ed., R.E. Tressler and R.C. Bradt, Plenum Press, N.Y., p. 549.

M.F. Yan, R.M. Cannon and H.K. Bowen (1975b), "Substructure Formation in Hot Forged KCl and KBr", in N.J. Grant, et al., Research on Materials for High Power Laser Windows, AFCL-TR-76-0027.

F. Transmission Electron Microscopy of CaF_2

F.1. Introduction

An investigation to characterize the microstructure developed during hot forging of single crystal CaF_2 has been accomplished using transmission electron microscopy. Single crystal CaF_2 samples hot forged at temperatures of 590, 702, 817, and 907°C were examined in the transmission electron microscope using a double-tilt,liquid-helium cold stage.

F.2. Experimental Procedure

Hot forged CaF_2 specimens were cut to approximately 500 μ thick slices using a string saw. The cutting solution is comprised of SiC powder, glycerin and water, and the string saw wire is 375 μ in diameter. The 500 μ thick specimens were then mounted on a "polishing jig" using a low melting point wax and polished on 500 grit emery paper. After polishing, the specimens were approximately 375 μ in thickness. The slices of CaF_2 were next cut, either using the string saw or a surgical blade, to a size that will fit into a 2.3mm specimen holder. These "2.3 mm diameter" by 375 μ thick specimens were then chemically jet thinned for transmission electron microscopy.

Chemically jet thinning CaF_2 for transmission electron microscopy is a difficult process. This arises for two reasons. First, because CaF_2 is transparent, conventional means for detecting the appearance of a hole in the specimen during the jet thinning process cannot be employed; and second, because CaF_2 polishes (etches) nonuniformly.

Several solutions have been tried as possible candidates for the jet chemical thinning process.[1] The chemical solution which has yielded the most uniform polish of any tried to date is given below.

Chemical Polishing Solution at 70°C
400 ml H_2O
100 ml HCl
70 gm $AlCl_3$
70 gm NH_4Cl

Thin foils are made using a dual jet thinner. The specimen is observed during the thinning process with a light microscope. Transmitted light is used to illuminate the specimen surface. When the light is properly aligned, and "reflected" light is used to observe the specimen, "fine" structure on the surface of the specimen may be observed. When a hole appears it is observable; but generally not until it has become 0.5 to 1 mm in diameter. Due to the size of the hole, a major portion of the thin area is lost, making the transmission electron microscopy more difficult.

Before a specimen is placed in the electron microscope, it is coated with a thin layer of carbon. The carbon is applied by vapor deposition and prevents specimen charging.

TEM of CaF_2 at room temperature is precluded by interference from radiation damage from the electron beam[1]. Thus TEM observations were made below 60°K using a liquid-helium cold stage developed under the previous contract.[2]

F.3. Results and Discussion

The results obtained from the observation of the deformation structures of hot forged CaF_2 will be divided between an analysis of the sub-grain boundaries and the relation of the sub-grains to the observed macroscopic behavior.

F.3.1. The Sub-Grain Boundary Structure

Observations of the microstructure resulting from hot forging has led to the characterization of two types of sub-grain boundaries (SGB's). The types of SGB's developed during the forging process are dependent upon forging temperature (flow stress) and are classified as equilibrium or nonequilibrium boundaries. The characterization of the two types of boundaries has been done by considering the defect comprising the SGB structure. These are:

(1) Intrinsic sub-grain boundary dislocations which are a requirement of the boundary geometry and are associated with equilibrium SGB's.

(2) Extrinsic sub-grain boundary dislocations which are those dislocations resulting from the accommodation of matrix dislocations into the boundary and are not a requirement of boundary geometry but may decrease the energy of the system while increasing the energy of the boundary.

Figure F.1. presents a series of micrographs typical of the sub-grain boundaries observed after forging at 590°C. Some sub-grain boundaries are highly disordered and appear to have a nonequilibrium structure, Figure F.1a, b. Evidence of the interaction of extrinsic dislocations with those of the boundary is seen in Figure F.1a and b. At A extrinsic (matrix) dislocations are interacting with the boundary but are not accommodated into the boundary. These disordered boundaries should have stress fields of significant proportion and may affect the deformation behavior. In addition to the highly disordered sub-grain boundaries, several twist, Figure F.1c, and tilt boundaries were observed; however, the majority of the observed boundaries were highly disordered. The twist boundary of Figure F.1c consists of intrinsic dislocations and is highly equilibrated. Further evidence of a nonequilibrium microstructure was manifest by a high matrix dislocation density. The matrix dislocations generally existed in gross tangles and were extensive in nature.

The effect of increasing the forging temperature from 590°C to 702°C may be seen in Figure F.2. The boundaries

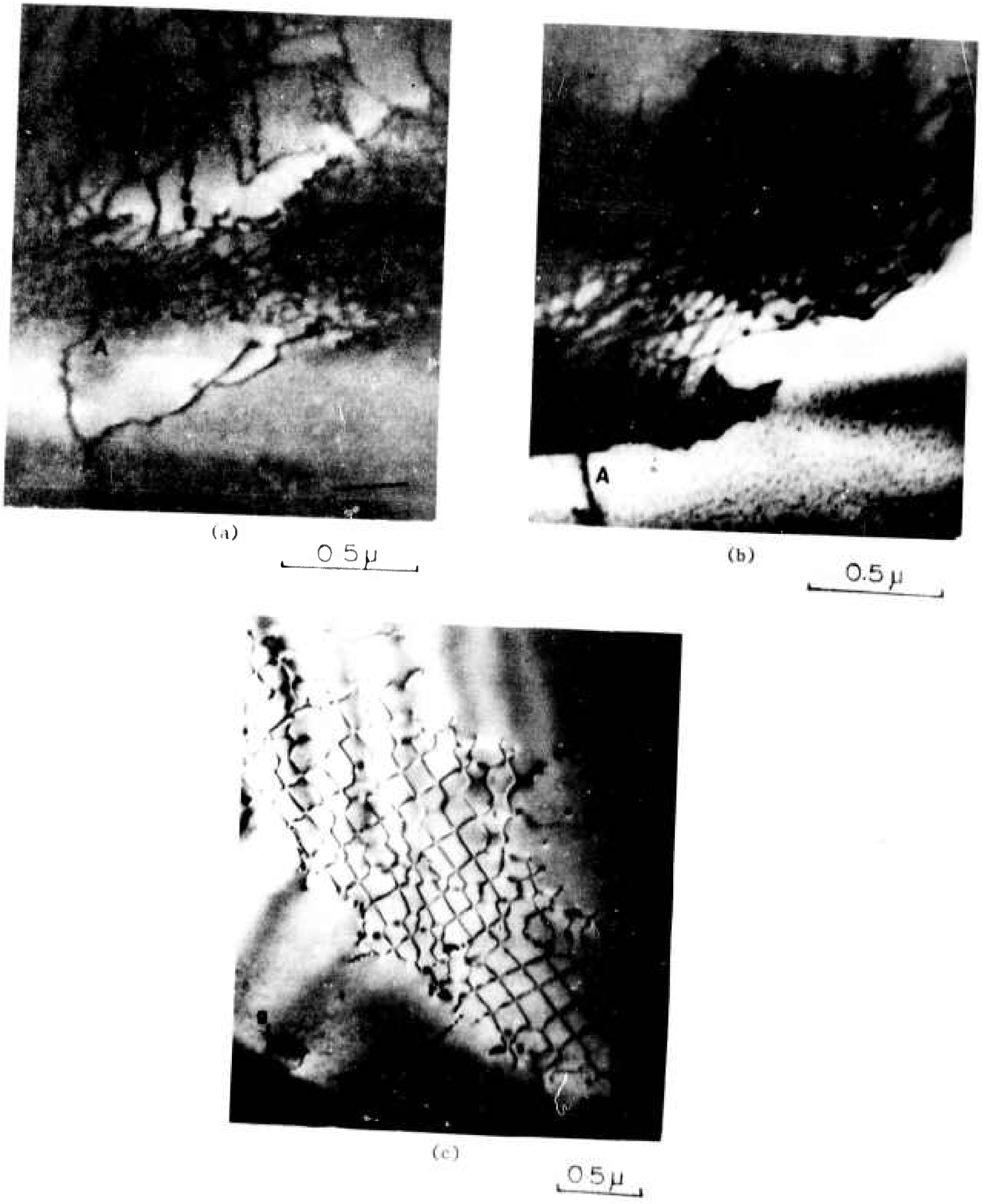

(a)

(b)

(c)

Figure F.1. TEM micrographs of sub-grain boundaries produced from hot forging at 590°C; (a) g = (022), (b) g = (022), (c) g = (111).

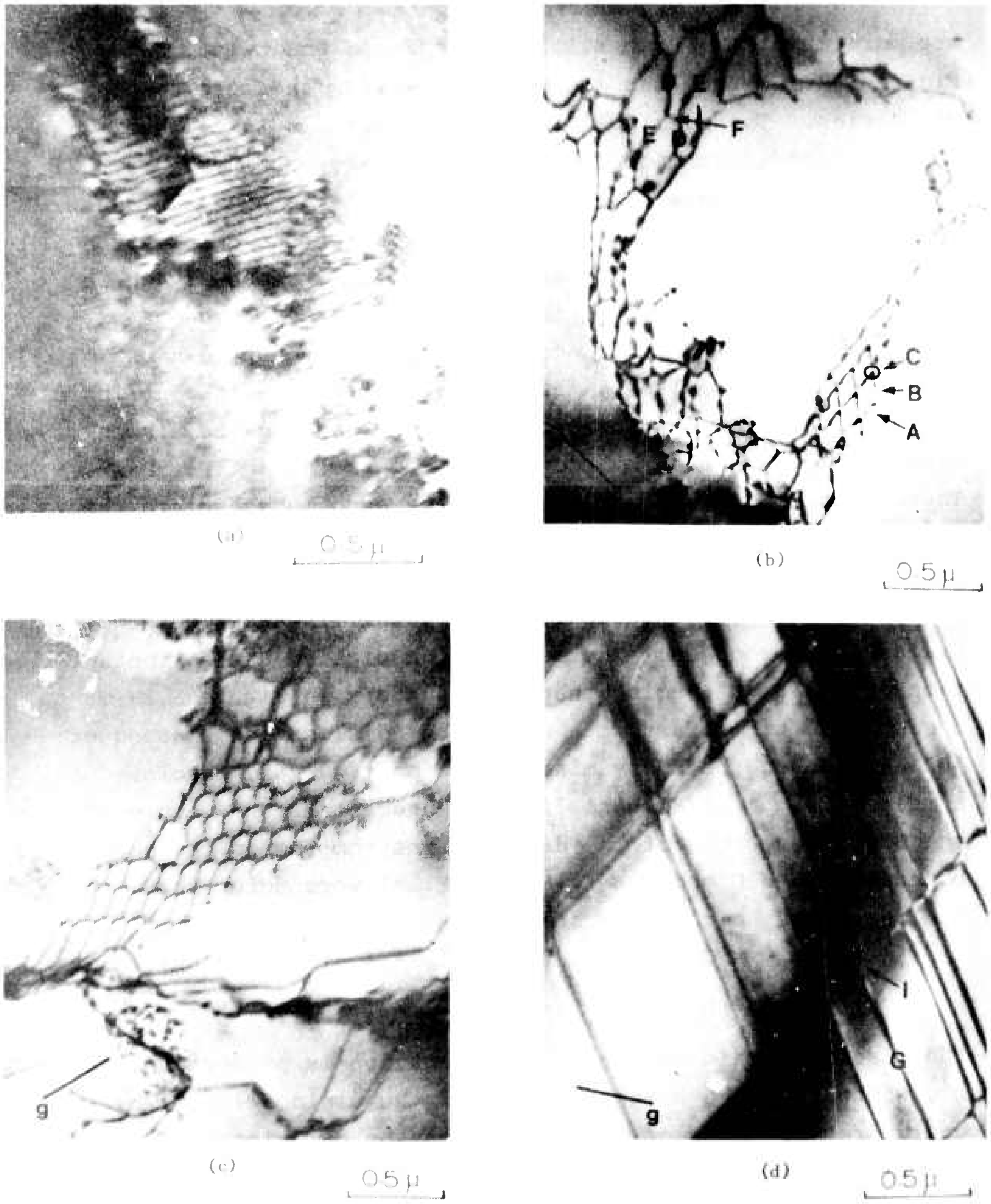

Figure F.2. TEM micorgraphs of sub-grain boundaries produced from hot forging at 702°C; (a-d) g = (022).

are more ordered. Both tilt, Figure F.2a, and twist, Figure F.2c, boundaries are seen as well as the more complex boundaries. The matrix dislocation density is lower than that at 590°C. The more ordered boundaries, as in Figure F.2a and F.2c should have short-range stress fields and should not be capable of initiating slip, but may alter the deformation behavior. Figure F.2a presents a simple tilt boundary where the intrinsic dislocations are easily discerned. The presence of extrinsic dislocations in the boundary can be seen directly and also by the discontinuities in the intrinsic dislocations (the extrinsic dislocations causing the discontinuities may be seen by using other operating reflections). These extrinsic dislocations have been accommodated into the boundary. In an effort to determine the misorientation between the two grains in Figure F.2a, an electron diffraction experiment measuring the shift in Kikuchi lines between two grains was performed. The measurement yielded a misorientation of 0.36°. Assuming that the boundary in Figure F.2a is a simple tilt boundary with a measured dislocation spacing of 500 Å, then the boundary misorientation is 0.46°, in close agreement with the Kikuchi line measurements. The nature of the Burgers vectors of the dislocations comprising the subboundaries A-B-C and D-E-F (Figure F.2b) were determined. The reactions which occur are:

(1) A + B = C $\qquad \frac{1}{2}[10\bar{1}] + \frac{1}{2}[101] \rightarrow [100)$

(2) E + F = D $\qquad \frac{1}{2}[10\bar{1}] + \frac{1}{2}[011] \rightarrow \frac{1}{2}[110]$

The elastic strain energy of a dislocation is proportional to b^2, where b is the Burgers vector of the dislocation. The energy requirements of (1) and (2) may be calculated using the b^2 criteria to determine if these reactions are energetically favorable. Reaction (2) is clearly favorable, while the energy of the reactants and products of (1) are equal. Closer attention must be given to the exact nature of the dislocations. The Burgers vector of A and B are inclined by approximately 45° and 30° to their dislocation lines, respectively, while that of C is nearly parallel. Thus, A and B are mixed, i.e., part edge and part screw while C is almost pure screw. Since the energy of an edge dislocation ($\alpha \frac{b^2}{1-\nu}$) is greater than that of a screw dislocation ($\alpha\ b^2$), any reaction where the reactants have a significant edge component and the product is primarily screw will be favorable. This is the case in reaction (2), and the reaction is favorable. Figure F2d is a boundary which lies nearly parallel to the foil surface. The dislocation reaction which occurs is

$$(3)\quad G + H = I \qquad\qquad \frac{1}{2}\,[101] + \frac{1}{2}\,[\bar{1}01] = [001]$$

Applying the b^2 criteria shows that the elastic strain energy of the reactants and product dislocations are equal. The Burgers vector of G is inclined 30° to the dislocation line. Dislocation H is pure edge and the Burgers vector of the product of the reaction, I, is inclined 45° to the dislocation line. Since the product dislocation is mixed, the energy of each dislocation must be calculated [using equation (1) below] to determine if the reaction is favorable.[3]

$$E = \frac{\mu b^2}{4\pi}\left[\frac{\sin^2\theta}{1-\nu} + \cos^2\theta\right] \ln \frac{\alpha R}{b} \qquad (F.1)$$

where μ is the shear modulus, α a constant, R the radial distance from the dislocation core, θ the angle between the dislocation line and the Burgers vector, and ν Poisson's ratio.

The reaction is favorable, however, only by the ratio of $\frac{E\ \text{products}}{E\ \text{reactants}} = \frac{1-\nu}{1}$. The fact that the reaction is not overly favorable may be evidenced by the observed constricted length of the product dislocation.

The SGB's developed during hot forging at 817°C are presented in Figure F.3. These boundaries are highly ordered and have become equilibrated. The matrix dislocation density is lower than that at 590°C and 702°C. The boundaries should have short-range stress fields. Figure F.3a is a compound boundary made up of twist and tilt components; F.3b shows the intersection of two highly ordered twist boundaries. The

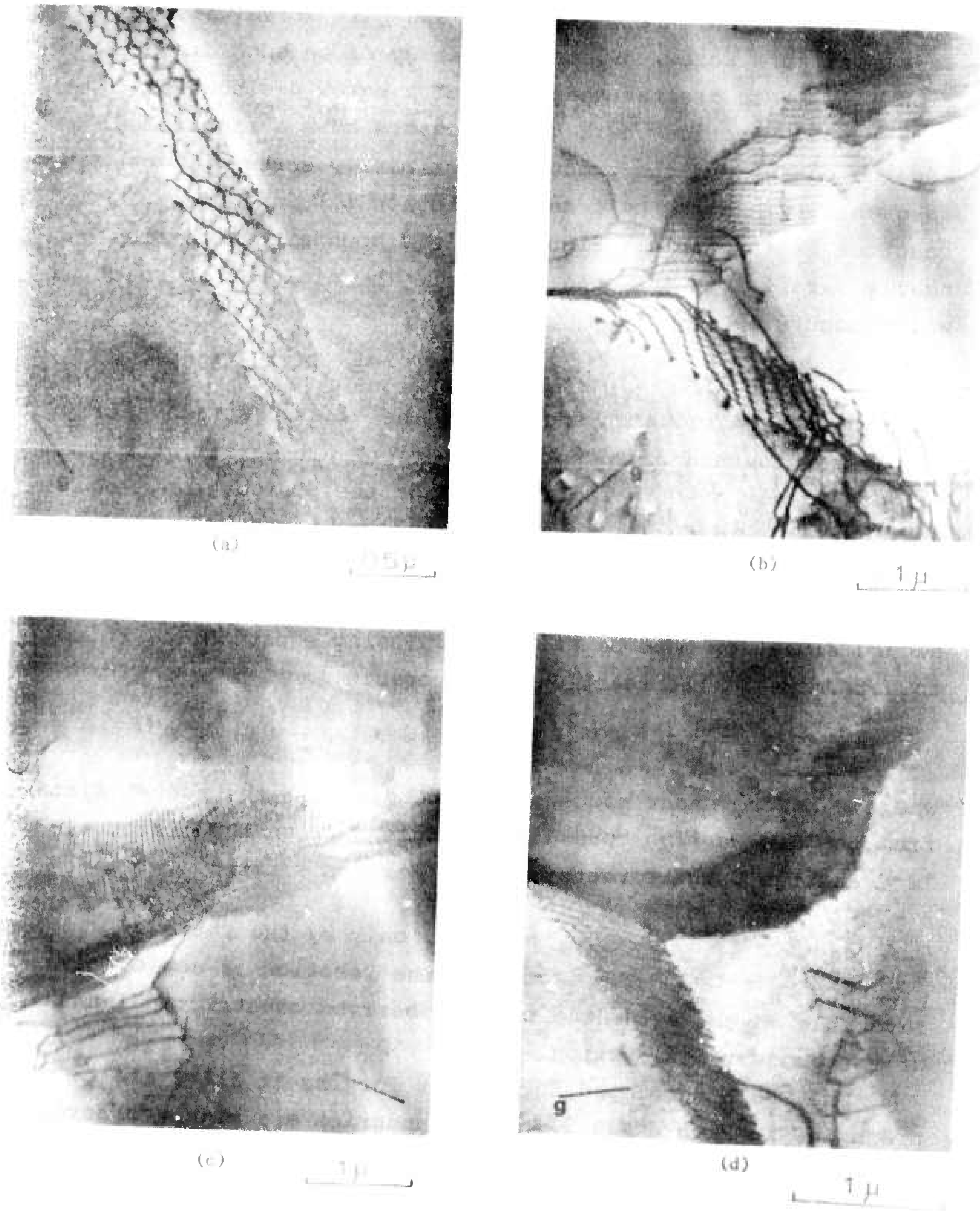
(a) (b) (c) (d)

Figure F.3. TEM micrographs of sub-grain boundaries produced from hot forging at 817°C; (a-d) g = (022).

upper boundary has extrinsic dislocations which have intersected the boundary although there does not appear to be any interaction with the boundary. Figure F.3c and F.3d also show highly ordered subboundaries produced from the hot forging.

The SGB's observed after hot forging at 907°C are presented in Figure F.4. Nearly all the boundaries observed at 907°C consisted entirely of intrinsic dislocations and were highly ordered. The density of extrinsic dislocations was very low, indicating that these dislocations were either annihilated by interactions within the grains or accommodated in the SBG's. The SGB in Figure F.4b is composed of a highly ordered structure with a number of boundary defects, labeled A. These defects may be either extrinsic dislocations or grain boundary ledges. The misorientation of the SGB in Figure F.4b was found to be ∿ 1° by measuring spot splitting in the electron diffraction pattern. The apparent migration of extrinsic dislocations to a SGB is shown in Figure F.4d. These dislocations are being accommodated into the boundary at the expense of increasing both the angle and energy of the boundary while decreasing the energy of the system. The accommodation of these extrinsic dislocations into the boundary may be rate a controlling mechanism in the overall recrystallization process; but more importantly this may be a mechanism by which a "high" angle grain boundary is created. This boundary could then produce abnormal or secondary grain growth.

The effect of increasing the forging temperature from 590°C to 907°C on the observed microstructure may be summarized as follows:

(1) The matrix dislocation density decreases.

(2) The SGB's become increasingly ordered.

(3) There appears to be increased interaction of extrinsic dislocations with the boundary.

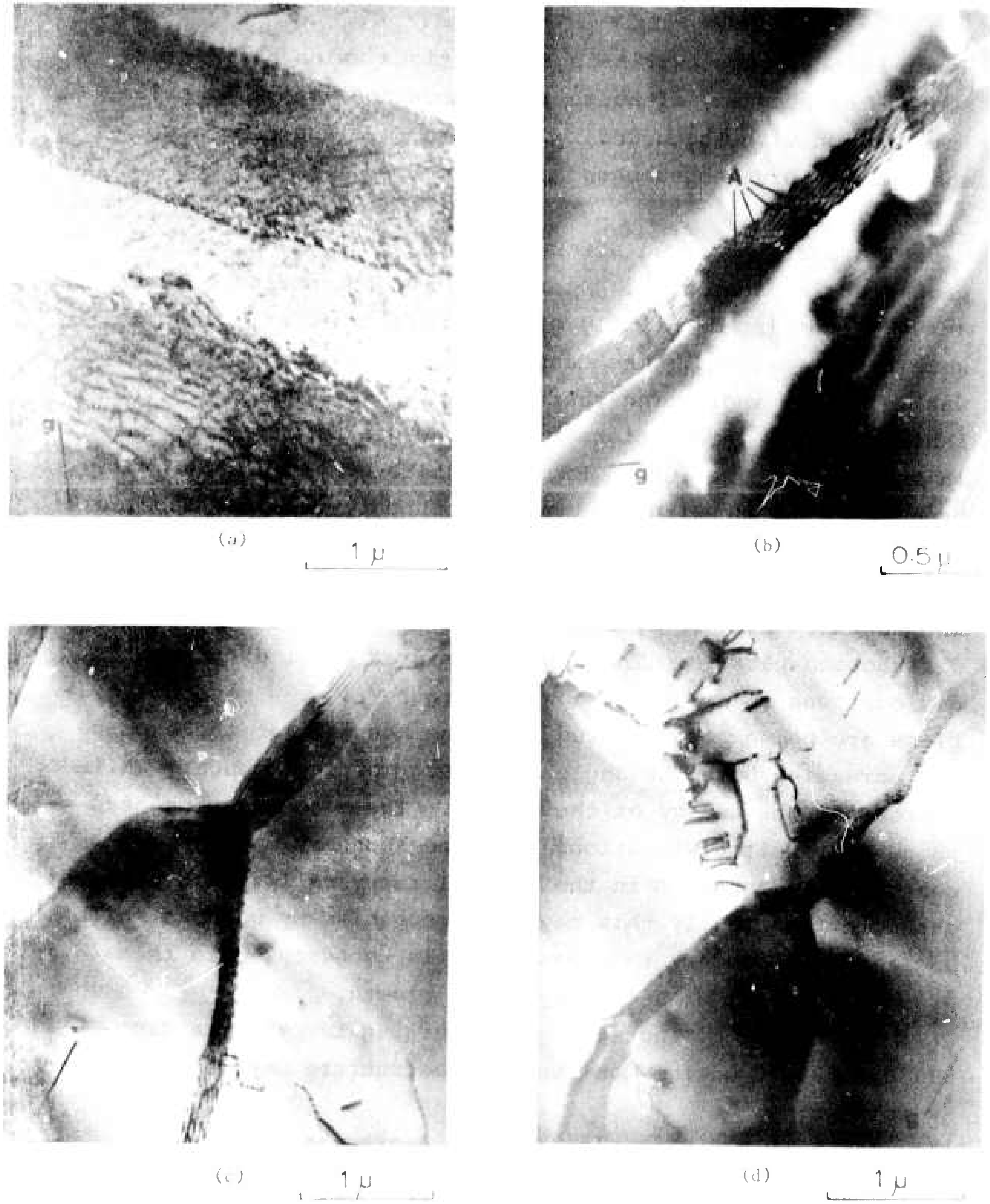

Figure F.4. TEM micrographs of sub-grain boundaries produced from hot forging at 907°C; (a) g = (022), (b) g = (022), (c) g = (111), (d) g = (111).

F.3.2. The Relation of Sub-Grain Structure to Observed Macroscopic Behavior

The previous sections have considered the effect of flow stress or forging temperature on the type of sub-grain boundary developed during hot forging of single crystal calcium fluoride to compressive strains of approximately 50%. In this section, the results of sub-grain size observations and calculations made with the aid of transmission electron microscopy are presented.

Micrographs typical of those used in determining sub-grain size are presented in Figures F.5 and F.6. Figure F.5 shows a variety of sub-grain boundary structures. There appears to be a duplex sub-grain boundary structure present. Within a more well defined and ordered subboundary are several lower dislocation density, less ordered subboundaries. The larger, more ordered subboundary has dimensions of ∿ 20-30 μm in diameter, whereas the less ordered subboundaries are ∿ 4-6 μm in size. Although Figure F.5 clearly suggests a duplex sub-grain boundary structure it is not typical of that which is generally observed. Figure F.6 shows sub-grain boundary structures more typical of the subboundaries observed as a result of forging at temperatures of 590, 702, 795, and 907°C. The boundary structure is much more uniform although there is still a suggestion of a duplex sub-grain boundary structure. However, any suggestion of a duplex structure disappears at the highest forging temperatures.

Table F.1 below presents a compilation of the sub-grain boundary calculations made on specimens hot forged at 590, 702, 795, and 907°C.

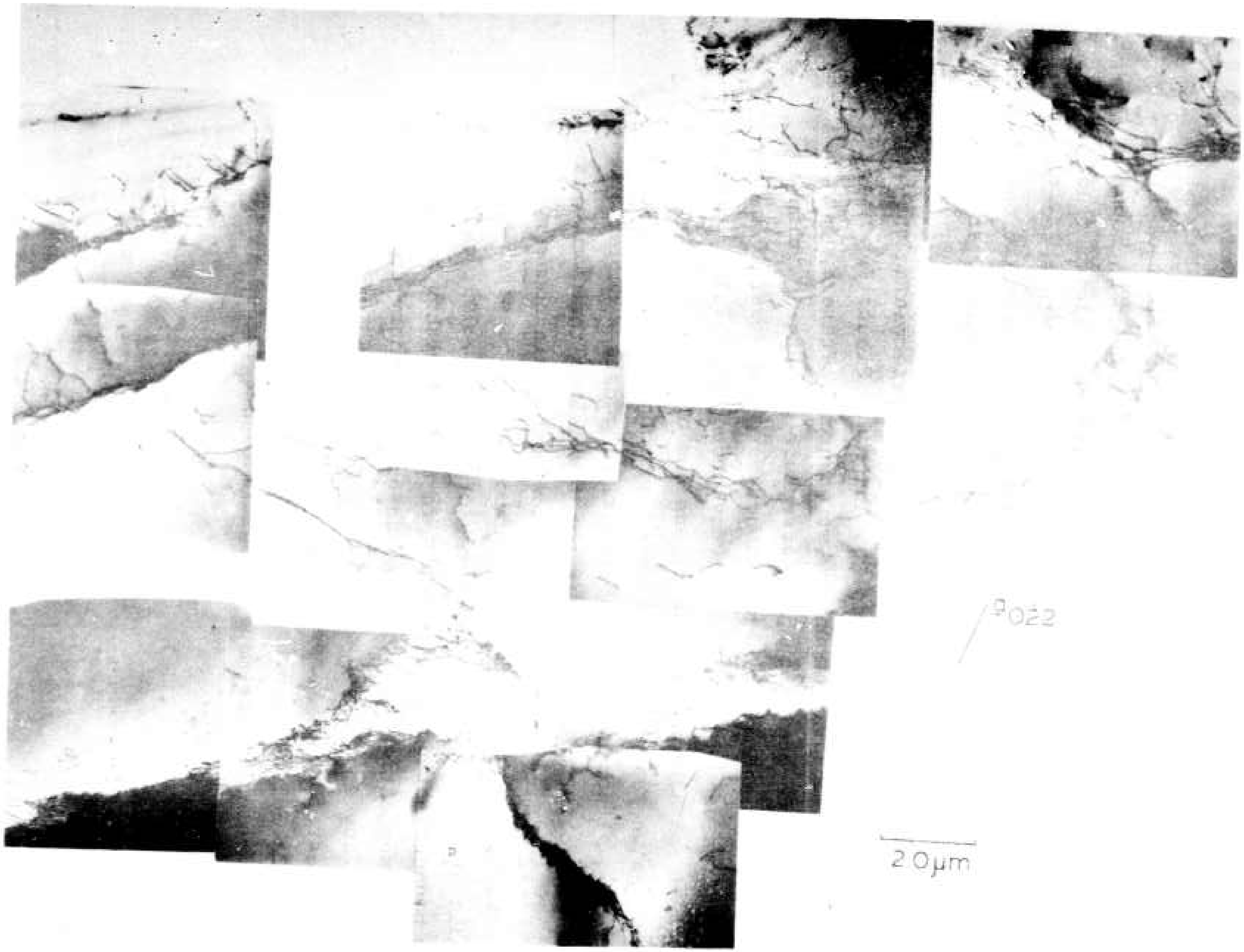

Figure F.5. Transmission electron micrograph of the microstructure developed from forging at 590°C.

Figure F.6. Transmission electron micrograph of the microstructure developed from forging at 590°C.

Table F.1

Temp (°C)	d (μm)	σ (psi)
590	5.41; 3.69	5300
702	4.79; 5.54	4000
795	6.63; 5.54	3300
907	6.82	2560

A plot (Figure F.7 of ln σ (flow stress) versus ln $\bar{d}$ (sub-grain size) demonstrates the power law dependence of flow stress on sub-grain size. A least squares analysis of the points plotted in Figure F.7 yields the linear ln-ln relationship presented in Equation (F.2)

$$\ln \sigma = -1.027 \ln d + 9.978 \qquad (F.2)$$

Equation (F.2) can be converted to the power law dependence of Equation (F.3).

$$\sigma = 2.155 \times 10^{4} d^{-1.027} \qquad (F.3)$$

Compilation of available data in metallic materials[4], e.g. Cu, Al, Fe and Fe + 0.007% C, demonstrates that the flow stress is inversely proportional to the subgrain or cell size. Similar results are seen in KCl[5], and KBr[6].

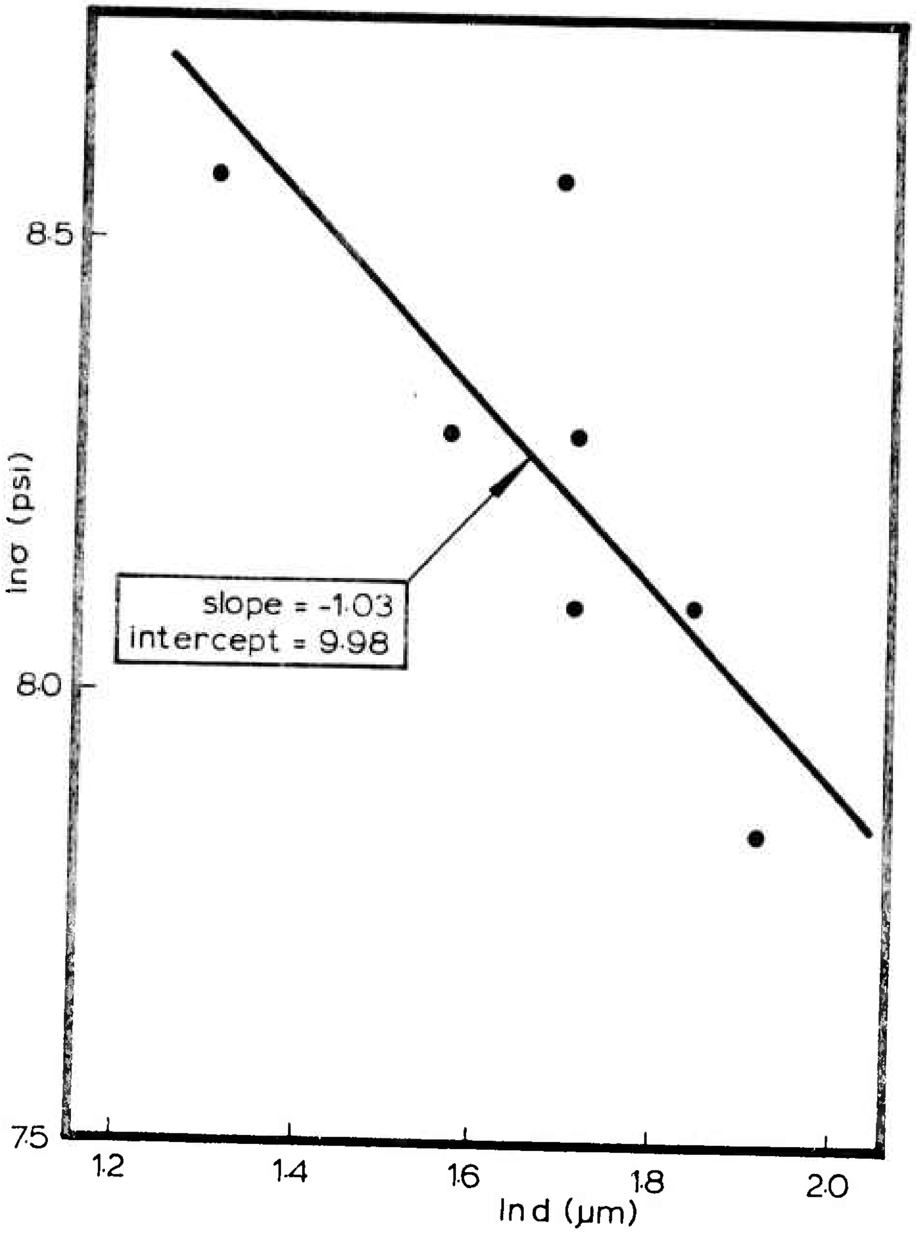

Figure F.7. Plot of ln (flow stress) as a function of ln (sub-grain size).

F.4. References

1. H.K. Bowen, et al, Research on Materials for High Power Laser Windows, Semi-Annual Technical Report No. 2, RADC-TR-76-348, (1976).

2. J.B. VanderSande, "Transmission Electron Microscopy of Alkali Halides", in N.J. Grant et al., Research on Materials for High Power Laser Windows, AFCRL-TR-76-0027, (1975).

3. A.H. Cottrell, Dislocations and Plastic Flow in Crystals Clarendon Press, Oxford U., p. 51, (1965).

4. M.R. Staker and D.L. Holt, Acta. Met., 20, 569, (1972).

5. M.F. Yan, et al, "Grain Boundaries and Grain Boundary Mobility in Hot Forged Alkali Halides", in Deformation of Ceramic Materials", ed. R.C. Bradt and R.E. Tressler, Plenum Press, N.Y., 549, (1975).

6. M.F. Yan, R.M. Cannon, and H.K. Bowen, "Substructure Formation in Hot Forged KCl and KBr", in ref 2.

G. PRINCIPAL STRESS EFFECTS ON BRITTLE CRACK STATISTICS

G.1 INTRODUCTION

Ideally, the initiation of a micro-crack will not immediately lead to macroscopic cracking, even in brittle material. For this to be true, the first micro-crack must be stabilized by friction, plastic flow, or inhomogeneities. Only after there are a number of micro-cracks will they localize to form a macrocrack and limit the load to a maximum. Calculating the progress of micro-cracking towards the configuration giving maximum load then involves repeated stress analysis of the developing micro-crack distribution, as well as the statistics of the strengths of the elements that are about to break. This problem has been treated numerically and analytically by McClintock and Zaverl (1974), with the following general assumptions:

a) A two-dimensional array of regular hexagonal grains.

b) Grain boundary strengths against micro-crack nucleation or propagation from an adjoining grain that vary according to an extreme-value distribution.

c) Homogeneous elastic constants.

d) No dynamic effects.

e) No plastic flow.

f) Biaxial applied tension.

The last restriction is relaxed here so as to find the effects of changing the ratio of the applied tensile stress components, while still maintaining enough tension to avoid the effects of crack closure and friction. While these models are still far from representing actual brittle materials such as rocks and ceramics, it is hoped that they provide a worth-while improvement in insight over previous approximations that consider the effects of statistics without the micro-stress analysis, or stress analysis of regular arrays of micro-cracks.

G.2 STATISTICAL DISTRIBUTION OF GRAIN BOUNDARY STRENGTH

The grain boundary strengths are taken to follow an extreme-value distribution of the second kind, with the distribution of strengths increasing as some power m of the amount by which the local normal stress on the center of the grain boundary exceeds some lower limit of strength S_L. More specifically, the probability that the strength S of a grain boundary lies below S_1 is given in terms of the parameters S_L, S_0, and m by

$$p(S<S_1) = 1 - \exp\left[-\left(\frac{S_1-S_L}{S_0-S_L}\right)^m\right] . \qquad (G.1)$$

Then fracture nucleates at the center of a grain segment when the normal stress σ_{nn} reaches a critical value

$$\sigma_{nn} = S_1 \ . \tag{G.2}$$

For a review of the derivation, and tables of mean and standard deviation in terms of part size and the parameters, see for example McClintock and Zaverl (1977). In general, one might expect the shear as well as the normal component of stress to affect fracture of a grain boundary, but any such shear effects will be neglected here.

In the presence of an adjacent crack, a grain boundary segment may still crack by nucleation, as described above, or it may crack by propagation. In this latter case, the resistance to cracking will be described by the singularity of normal stress along the grain boundary. This singularity of normal stress is related to the stress intensity factor at the crack tip and the orientation θ of the grain boundary relative to the crack. To eliminate the repetitious π we follow Sih and Liebowitz (1968) and define the stress intensity in terms of crack half-length c and the applied normal stress at infinity S such that

$$k_1 \equiv \left(\sigma_{\theta\theta}\right)_{\theta=0} \sqrt{2r} = S\sqrt{c} \ . \tag{G.3}$$

(The more familiar K_I is

$$K_I \equiv k_1 \sqrt{\pi} .) \qquad (G.4)$$

Then the intensity of normal stress on a boundary at an angle θ to the crack from Sih and Liebowitz (1968) is

$$k_\theta \equiv \sigma_{\theta\theta} \sqrt{2r} = k_1 \; (1/2)(1 + \cos\theta)(\cos\theta/2) \; . \qquad (G.5)$$

The critical value of this normal boundary intensity factor is again assumed to have an extreme-value distribution of the second kind, so that the probability of its value being less than some particular value $k_{\theta 1}$ is

$$p \; (k_\theta < k_{\theta 1}) = 1 - \exp \left[- \left(\frac{k_{\theta 1} - k_{\theta L}}{k_{\theta 0} - k_{\theta L}} \right)^{m_k} \right] . \qquad (G.6)$$

For insight, the statistical parameters $k_{\theta L}$ and $k_{\theta 0}$ may be normalized in terms of the grain boundary half length c_1 , conversion factors $f_{k\theta L}$ and $f_{k\theta 0}$, and the corresponding parameters for crack nucleation:

$$k_{\theta L} \equiv f_{k\theta L} \; S_L \sqrt{c_1} \; , \quad k_{\theta 0} = f_{k\theta 0} \; S_0 \sqrt{c_1} \; . \qquad (G.7)$$

Then if propagation is viewed as nucleation by the normal stress S at a radial distance δ/c_1 from the crack tip,

$$S_L = k_{\theta L}/\sqrt{2\delta} = f_{k\theta L} \; S_L \sqrt{c_1/2\delta} \; , \text{ or } f_{k\theta L} = \sqrt{2\delta/c_1} \; , \qquad (G.8)$$

and similarly for $f_{k\theta 0}$.

G.3 NUMERICAL MODEL

A numerical model was used to suggest assumptions for and to test an analytical model.

The numerical model is a form of boundary integral method in which the traction-free cracks are modeled by dislocation arrays simultaneously chosen to cancel the effects of the applied stress. For simplicity, each crack is approximately modeled by one dislocation pair, so the number of degrees of freedom is just the current number of crack segments. Once the necessary dislocation strengths have been found for any given crack configuration, the stress is calculated at each grain boundary, and the stress intensities are found at each crack tip. The weakest element relative to its applied stress is then found, assumed to be cracked, and the calculation is repeated. Fracture is determined by the weakest segment relative to the current stress on it, or if a crack tip is more critical, by the lowest segment toughness relative to the current local intensity of normal stress across a grain boundary. After the most critical segment is found, it is assumed cracked. Then a new elastic solution is calculated, a new most critical segment is found, and so on.

Some typical results are shown in Figs. G.1 and G.2. The cracked segments are numbered in order of cracking. Those that cracked after a maximum load had been attained are denoted by dashed lines. Two different orientations were considered for the hexagonal array relative to the direction x_1 of the maximum principal component of applied stress, S_1 . In the "vertex" orientation, one of the vertices of the hexagons is in the direction of maximum principal stress component; in the "face" orientation one of the faces of the hexagon is in that direction.

With the vertex orientation of Fig. G.1, the cracks tend to form along the set of zig-zag lines at ± 60° to the maximum principal stress direction. Under combined stress, it is then reasonable to build an analytical model on this pattern, taking into account the combined effect of the two applied stress components on the normal stress required to initiate these 60° cracks, and the critical normal grain boundary intensity, k_θ , required to propagate them.

For the face orientation of Fig. G.2, as the transverse stress is reduced the cracks tend to form along the 90° segments rather than on those at 30° to the maximum principal stress direction. Here the model must be more complex. First, the critical event seems to be not the

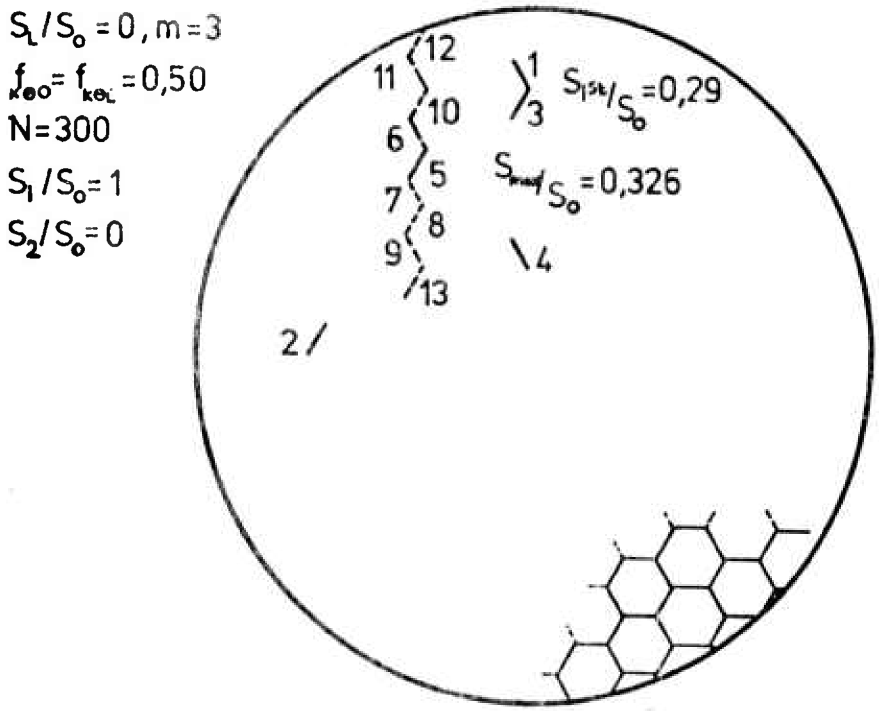

Fig. G.1 Sample cracking pattern for a vertex orientation.

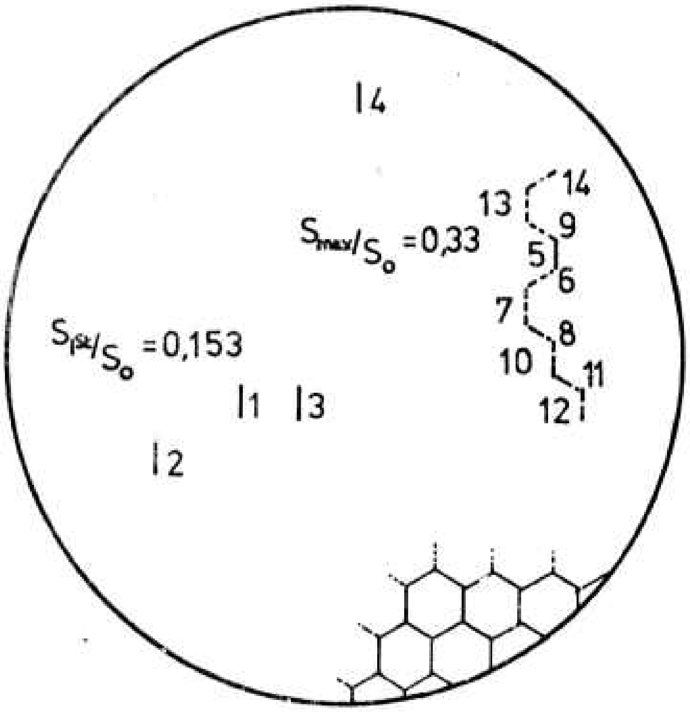

Fig. G.2 Sample cracking pattern for a face orientation.

formation of the normal cracks, so much as the subsequent cracking of the 30° cracks. These latter are thus taken to be the unit building blocks out of which an approximate statistical theory for macro-cracking will be built. Further discussion of the results from the numerical theory will be deferred until the analytical model has been developed for comparison.

G.4 ANALYTICAL MODEL

The essence of the analytical models is to estimate the maximum strength by first finding the density of unit cracks as a function of applied stress level. The probability of aggregations of length 2c of these cracks is then estimated. When the crack lengths and applied stresses are high enough to cause crack extension even with median strengths at the crack tip, a maximum strength is assumed to have been attained.

Vertex Orientation

For the vertex orientation, the cracking is observed to be predominantly in the directions at ± 60° to the direction of maximum tensile stress. For nucleation, the normal stress on these segments is found by Mohr's circle from the maximum and minimum principal stress components to be

$$\sigma_{\theta\theta} = 3S_1/4 + S_2/4 \quad . \qquad \text{(G.9)}$$

The fraction of ± 60° boundaries that are cracked at principal applied stress components S_1 and S_2 is now found by substituting back into Eq. G.1, and noting that segments of this orientation comprise 2/3 of the total number of grain segments:

$$p = 1 - \exp\left[-\left(\frac{(3S_1+S_2)/4-S_L}{S_0 - S_L}\right)^m\right] \quad . \tag{G.10}$$

The total number of cracked grains in a part of size N is

$$N_t = (2/3)\ N\ p \quad . \tag{G.11}$$

With this fraction of cracked grains, we ask the probability that a contiguous chain of N_c has formed. Following McClintock (1974), approximate the actual conditions by a linear array of (2/3) N grain segments of which the fraction p are cracked. The longest contiguous crack which has a probability Φ of forming is approximately

$$N_c = \frac{\ell n\left(\dfrac{(2/3)\ N\sqrt{p}}{(.5-1/\ell n(p))(-\ell n(1-\Phi))}\right)}{-\ell n\ (p)} \quad . \tag{G.12}$$

The strength of the crack of length N_c is estimated from fracture mechanics as the applied stress required to crack the next segment ahead, assuming no other cracks in the neighborhood of the tip. (This is an overestimate if any neighboring cracks lie ahead of the crack, but an underestimate if any such cracks lie off to the side of the tip, tending to shield it as a plastic zone would.) Furthermore, assume the average direction of the crack is normal to the maximum principal applied stress S_1 and the length is the projected length of the segments, $2c_1 \cos 30°$. Then

$$k_{1c} = S_1\sqrt{(N_c\ 2c_1\ \cos\ 30°)/2}\ . \tag{G.13}$$

For a long crack, k_{1c} is found by the lower of the two median strengths for nucleation and propagation. Approximating the prior zig-zag crack segments by a straight line as shown in Fig. G.3, the normal grain boundary intensity, for propagation, is reached when

$$k_\theta = k_{1c}\ \Big((1 + \cos\ 30°)(\cos\ 15°)/2\Big) = 0.901\ k_{1c}\ . \tag{G.14}$$

For a median value of the normal grain boundary intensity and noting that there are two possible crack sites, one at each crack tip, from Eqs. G.6 and G.7, and combining Eqs. G.13 and G.14,

$$0.5 = 1 - \exp\left[-2\left(\frac{0.901\ S_1\sqrt{N_c \cos\ 30° c_1} - f_{k\theta L}\sqrt{c_1}}{f_{k\theta 0}S_0\sqrt{c_1} - f_{k\theta L}S_L\sqrt{c_1}}\right)^m\right]\ . \tag{G.15}$$

If the next segment cracks by nucleation, use Eq. G.1 for the distribution of strengths and find the stress on the next grain from the stress intensity factor:

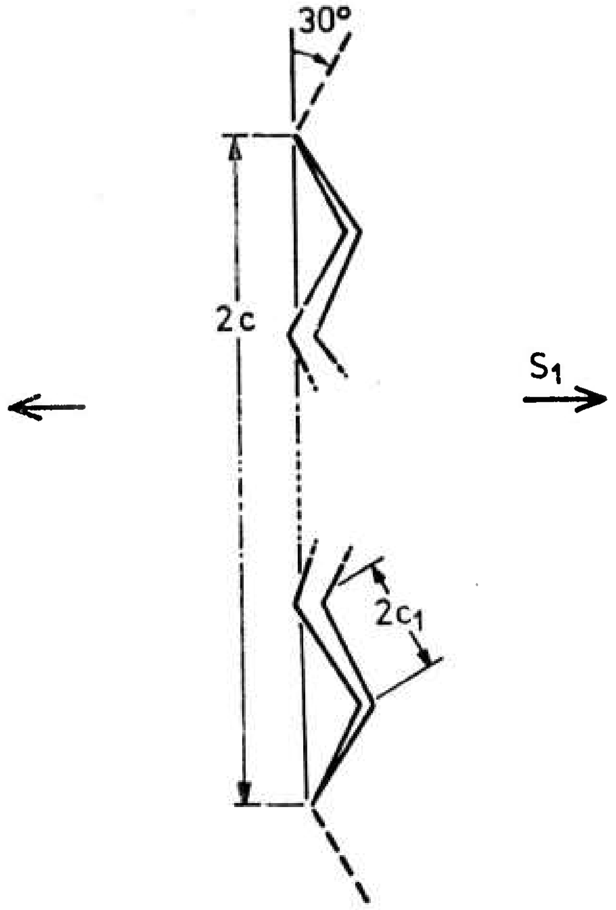

Fig. G.3 Approximating the stress intensity with applied stress in the vertex direction.

$$\sigma_{\theta\theta} = k_{1c} \Big((1 + \cos 30°)(\cos 15°)/2\Big)/\sqrt{2c_1} = 0.901 k_{1c}/\sqrt{2c_1}. \quad \text{(G.16)}$$

Combining Eqs. G.1, G.13, and G.16,

$$0.5 = 1 - \exp\left[-2\left(\frac{0.901\ S_1\sqrt{.5N_c}\cos 30° - S_L}{S_0 - S_L}\right)^m\right]. \quad \text{(G.17)}$$

Since we assume k_θ and $\sigma_{\theta\theta}$ to be calculated from the same random sample, the choice between crack growth by propagation and re-nucleation, Eqs. G.15 and G.17, is set by the parameters $f_{k\theta L}$, $f_{k\theta 0}$, S_L, and S_0. The maximum stress is now the value of S_1 (for a given S_2/S_1) found by eliminating p and N_c from Eqs. G.10, G.12, and G.15 or G.17.

Face Orientation

For the face orientation, the boundaries normal to the principal stress direction crack relatively easily. The critical events are cracking of the oblique boundaries, at ± 30° to the maximum tensile direction. As shown in Fig. G.4, these oblique cracks may form after either or both of their neighbors. First consider their formation by propagation. If the interaction of the two normal cracks is neglected, the grain boundary intensity is set purely by S_1, and does not depend on whether one or both neighbors is cracked. The probability of an oblique crack

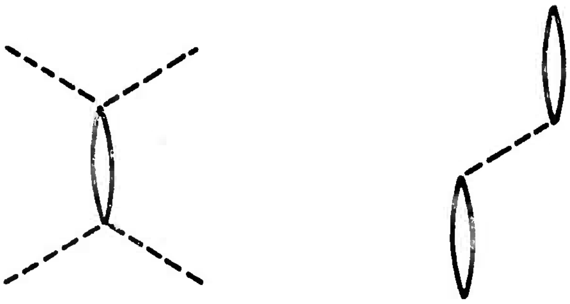

Fig. G.4 Forming oblique cracks with applied stress normal to a face.

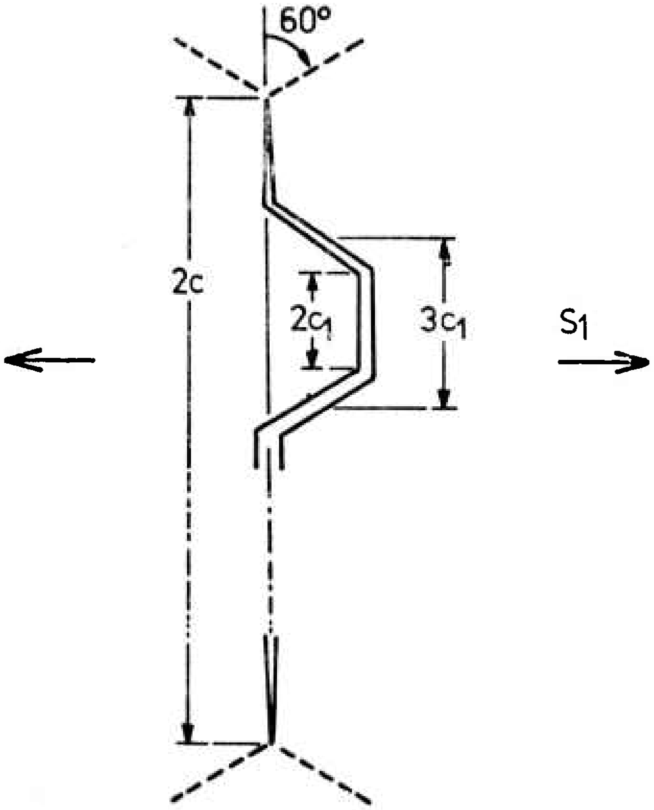

Fig. G.5 Approximating the stress intensity with applied stress normal to a face.

is then the sum of the probabilities that either neighbor or both are cracked, times the probability of cracking of the oblique crack given the cracked neighbors: $p_{\theta/n}$. Denoting the probability of a crack nucleating at a neighbor by p_n , the probability that an oblique boundary is cracked is

$$p = \left(2p_n \ (1-p_n) + p_n{}^2\right) p_{\theta/n} \quad . \tag{G.18}$$

The probability of a crack nucleating on a normal boundary is found from Eq. G.1:

$$p_n = 1 - \exp\left[-\left(\frac{S_1 - S_L}{S_0 - S_L}\right)^m\right] . \tag{G.19}$$

The probability of propagation of the oblique segment from a normal boundary is now found, noting there are four possible crack sites, two at each tip, from an equation for the grain boundary intensity in terms of the applied stress intensity factor and the orientation, and the distribution function for the grain boundary intensity:

$$k_\theta = k_1 \ (1 + \cos 60°)(\cos 30°)/2 = 0.649 \ k_1 \ , \tag{G.20}$$

$$p_{\theta/n} = 1 - \exp\left[-4\left(\frac{0.649 \ S_1 \sqrt{c_1} - f_{k\theta L} \ S_L\sqrt{c_1}}{f_{k\theta 0} \ S_0\sqrt{c_1} - f_{k\theta L} \ S_L\sqrt{c_1}}\right)^m\right] . \tag{G.21}$$

If the oblique crack forms by re-nucleation, the stress at its center will be influenced by the two adjacent cracks. Taking the stress field around a crack of finite length from Green and Zerna (1963) we find for one neighboring normal crack,

$$\sigma_{\theta\theta} = 0.301\ S_1 + 0.75\ S_2\ , \tag{G.22}$$

whereas for two cracks, with only one possible cracking site, allowing 30% interaction effects,

$$\sigma_{\theta\theta} = 0.370\ S_1 + 0.75\ S_2\ . \tag{G.23}$$

Accordingly,

$$p_{\theta/n} = 1 - \exp\left[-4\left(\frac{0.301\ S_1 + 0.75\ S_2 - S_L}{S_0 - S_L}\right)^m\right] \tag{G.24}$$

and

$$p_{\theta/2n} = 1 - \exp\left[-\left(\frac{0.370\ S_1 + 0.75\ S_2 - S_L}{S_0 - S_L}\right)^m\right]\ . \tag{G.25}$$

Eqs. G.24 and G.25 give the fraction of cracked grain boundary segments according to

$$p = 2p_n(1 - p_n)p_{\theta/n} + p_n^2\ p_{\theta/2n}\ . \tag{G.26}$$

The probability of forming a crack of N_c contiguous units, counting the projected distance between oblique cracks as one unit, is found as before from Eq. G.12.

The strength of a crack of length N_c is found by first finding the stress intensity due to a chain of cracks with projected length $3c_1$ per oblique crack, as shown in Fig. G.5. Then

$$k_{1c} = S_1 \sqrt{N_c \ (3c_1)/2} \ . \qquad \text{(G.27)}$$

Next, the value of k_{1c} for propagation is approximated as shown in Fig. G.5:

$$k_\theta = k_{1c} \left((1 + \cos 60°)(\cos 30°)/2\right) = 0.649 \ k_{1c} \ . \qquad \text{(G.28)}$$

For a median value of this normal grain boundary intensity with four possible crack sites,

$$0.5 = 1 - \exp \left[-4 \left(\frac{0.649 \ S_1\sqrt{N_c(3c_1/2)} \ - \ f_{k\theta L}\sqrt{c_1}}{f_{k\theta 0} \ S_0\sqrt{c_1} \ - \ f_{k\theta L} \ S_L\sqrt{c_1}} \right)^m \right] \ . \qquad \text{(G.29)}$$

If the next segment cracks by nucleation, use Eq. G.1 for the distribution of strengths and find the stress in the next grain from the stress intensity factor:

$$\sigma_{\theta\theta} = k_{1c} \left((1 + \cos 60°)(\cos 15°)/2\right) / \sqrt{2c_1} =$$

$$= 0.649 \ k_{1c}/\sqrt{2c_1} \ . \qquad \text{(G.30)}$$

The median strength against nucleation is found from

$$0.5 = 1 - \exp\left[-4\left(\frac{0.649\ S_1\sqrt{N_c(3/4)} - S_L}{S_0 - S_L}\right)^m\right] . \qquad \text{(G.31)}$$

Since again k_θ and $\sigma_{\theta\theta}$ are assumed to be determinate functions of the same grain boundary strength, the choice between nucleation and propagation, Eqs. G.29 and G.31, is governed by the parameters $f_{k\theta L}$, $f_{k\theta 0}$, S_L , S_0 , and S_2/S_1 . The maximum stress is now the value of S_1 (for the given S_2/S_1) found by eliminating p and N_c from Eqs. G.12 and G.18, G.19, G.21, and G.29 for propagation, or G.19, G.24, G.25, G.26 and G.31 for nucleation.

G.5 FORMATION OF THE FIRST CRACK

The first crack is especially susceptible to the toe of the distribution function, and to variables in the forming processes which give rise to it. Nonetheless, it is of interest to get some idea of the increase in stress between the first nucleation of cracks and the final instability, since this indicates the warning signals, such as acoustic emission, which might be detected prior to fracture.

The probability of first fracture is best found from the product of the probabilities that no fractures are found on any of the families of grain boundaries having a specific orientation relative to the direction of maximum principal stress.

Vertex Orientation

In a total of N grain boundaries, 2N/3 have an orientation of ± 60° to the direction of maximum principal stress. The normal stress on them is found from Mohr's circle:

$$\sigma_{\theta\theta} = 3S_1/4 + S_2/4 \quad . \qquad \text{(G.32)}$$

There are also N/3 segments normal to the second principal stress component, for which

$$\sigma_{\theta\theta} = S_2 \quad . \qquad \text{(G.33)}$$

The probability of first fracture at maximum principal stress S_1 and secondary principal stress $S_2 = C\ S_1$ is the complement of the probability of no fracture on either of these families of planes:

$$\Phi = 1 - \exp\left[-\frac{N}{3}\left(2(S_1(3 + C)/4)^m + (C\ S_1)^m\right)\right] \quad . \qquad (C>0) \quad \text{(G.34)}$$

Face Orientation

For the face orientation, there are N/3 segments subject to a normal stress of S_1 and 2N/3 segments subject to a normal stress of

$$\sigma_{\theta\theta} = S_1(1 + 3C)/4 \ . \qquad (G.35)$$

Introducing these stress components into the extreme value distribution we get the probability of first fracture:

$$\Phi = 1 - \exp\left[-\frac{N}{3}\left(S_1^m + 2\left(S_1(1 + 3C)/4\right)^m\right)\right], \ (C>-1/3) \ . \qquad (G.36)$$

With either orientation, the stress level S_1 for a given probability of fracture Φ and stress ratio $C = S_2/S_1$ can be found by solving Eq. G.34 or G.36.

G.6 DISCUSSION OF RESULTS

To illustrate the above equations, they were evaluated for the following values of the parameters:

$S_L = 0$, $S_0 = 1$

$f_{k\theta 0} = f_{k\theta L} = 0.50$

$m = 3, 10$

$N = 10 - 100,000$

$\Phi = 0.50$.

Figures G.6 and G.7 show the size effect for two different variabilities (m = 3, 10) and for uniaxial applied stress. Qualitatively, the curves are similar to those obtained earlier by McClintock and Zaverl (1977) for biaxial stress,

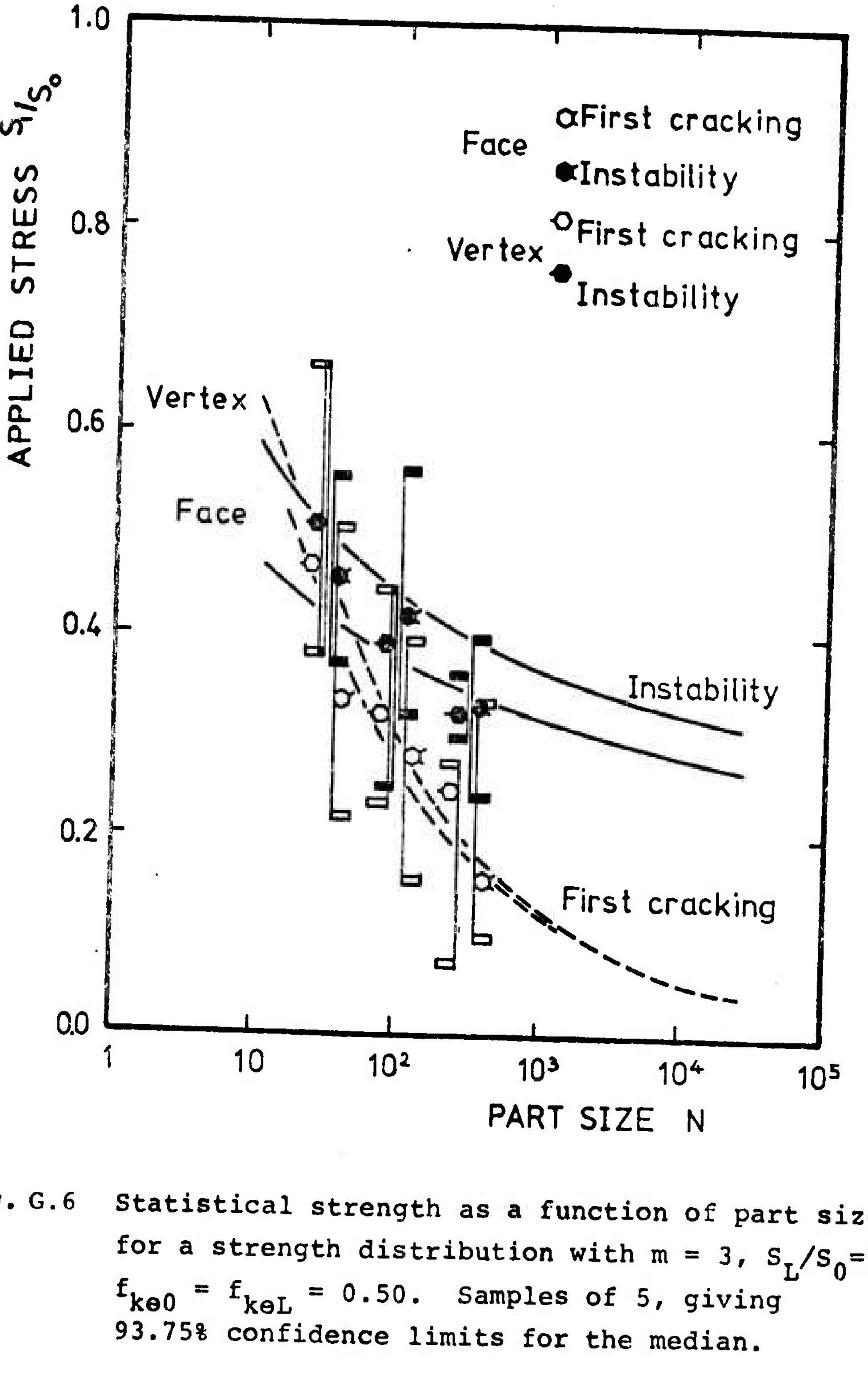

Fig. G.6 Statistical strength as a function of part size for a strength distribution with m = 3, $S_L/S_0=0$, $f_{ke0} = f_{keL} = 0.50$. Samples of 5, giving 93.75% confidence limits for the median.

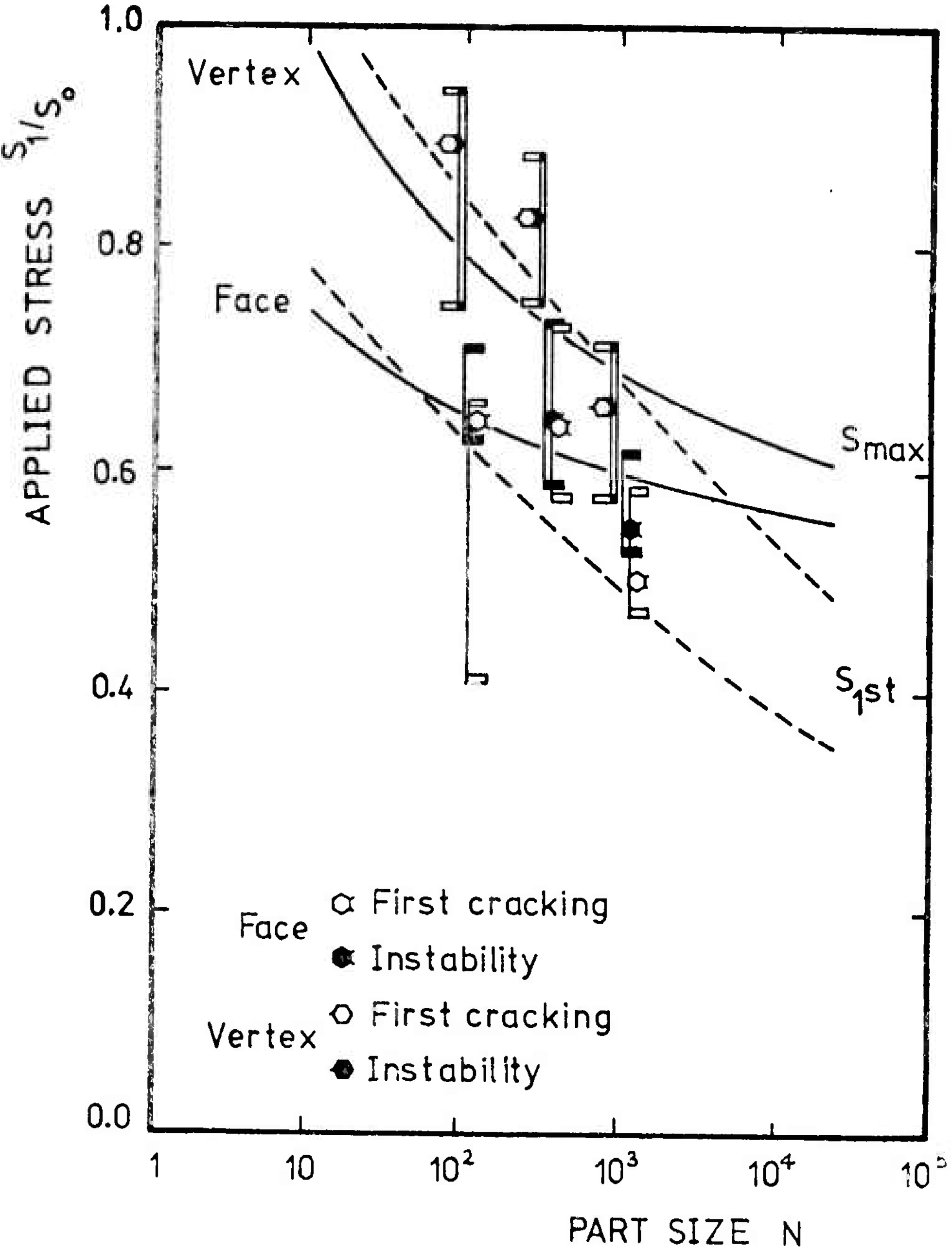

Fig. G.7 Statistical strength as a function of part size for a strength distribution with m = 10, $S_L/S_0 = 0$, $f_{ke0} = f_{KeL} = 0.50$.

but there is a smaller stress range between crack initiation and instability. Again an extreme-value distribution, valid for first fracture, would be a poor descriptor of maximum strength.

The fracture loci are shown in Fig. G.8 for an exponent m = 3 and a part size of N = 100 grain boundary segments. Note that there is an increase of the order of 50% in the stress for first cracking on going from biaxial to uniaxial applied stress. Crack closure begins at a transverse compressive stress of about half the tensile stress.

The numerical results are in reasonably good agreement with the analytical model although there is a slight discrepancy due to neglecting any interaction effects in calculating the density p of unit cracks in the analytical formulations. Larger numbers of boundaries would have to be studied to show whether the localization of cracking around a crack tip as it formed would tend to promote cracking along the line of the crack, or inhibit it by branch cracking that reduces the local stress concentration.

More accurate modeling should be done when specific data on flaw distributions are available for cases of practical interest. Modeling of compression cracks would require a computer program that would treat crack closure and friction.

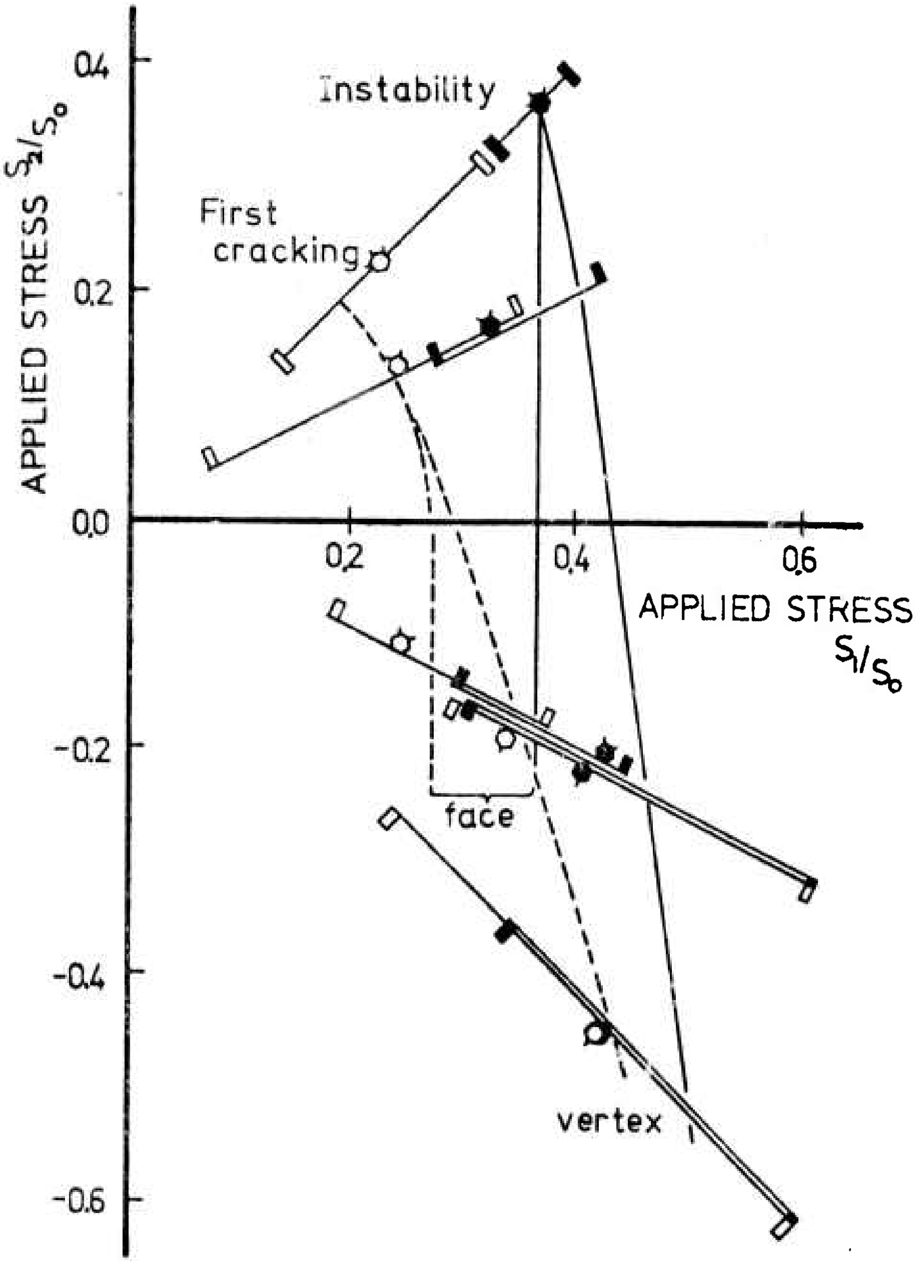

Fig. G.8 Principal stress fracture loci for first cracking and instability for an extreme-value distribution with $m = 3$, $S_L/S_0 = 0$, $f_{ke0} = f_{keL} = 0.50$, part size $N = 100$.

G.7 REFERENCES

Green, A. E. and Zerna, W., (1963), Theoretical Elasticity, 1st ed., reprinted 1963, Oxford, 279.

McClintock, F. A., (1974), "Statistics of Brittle Fracture," Fracture Mechanics of Ceramics, Vol. I, R. C. Bradt, D. P. H. Hasselman, F. F. Lange, eds., Plenum Press, New York, 93-114.

McClintock, F. A. and Zaverl, F. Jr., (1974), "Statistical Crack Mechanics: Brittle Initiation and Growth," Proc. 11th Ann. Meeting of Soc. of Eng. Sci., 6-7.

McClintock, F. A. and Zaverl, F., Jr., (1977), "An Analysis of the Mechanics and Statistics of Brittle Crack Initiation," to appear in Int. J. of Fracture.

Sih, G. C. and Liebowitz, H., (1968), "Mathematical Theories of Brittle Fracture," Fracture: An Advanced Treatise, Vol. II, H. Liebowitz, ed., Academic Press, New York, 67-190.

H. THE EFFECTS OF SURFACE INITIATED FRACTURE ON BRITTLE CRACK STATISTICS

H.1 INTRODUCTION

The problem of calculating the progress of micro-cracking in brittle materials towards the configuration giving maximum load, by repeated stress analysis of the developing micro-crack distribution, has been treated numerically by McClintock and Zaverl (1975). They considered grain boundary cracking in a two-dimensional array of regular hexagon grains embedded within an infinite body. However, brittle materials often fracture by the propagation of surface cracks, whether they are initiated at sub-critical stress levels or are pre-existing. With this in mind the numerical model is extended, using near surface dislocation dipoles, to study the effects on brittle crack statistics of surface or near surface initiated fracture.

H.2 A NUMERICAL MODEL FOR SURFACE INITIATED FRACTURE

The above numerical model of the mechanics of brittle crack initiation within an infinite medium is a form of boundary integral method. Crack segments are approximately modeled by one dislocation pair, by inserting a relative displacement dart D^m across the m^{th} segment, see(Fig. H.1.) The number of degrees of freedom is then just the current number of crack segments. The dart is defined as the Burger's vector at the second end of the segment. The resulting traction t^μ on the μ^{th} segment due to the m^{th} cracked segment is given by the influence coefficient $T^{\mu m}$, which is analagous with a Green's function (see for example, Hildebrand, 1952). Accounting for the applied stress at infinity $t^{\infty\mu}$ gives the traction t^μ as

$$t^\mu = T^{\mu m} D^m + t^{\infty\mu} \quad . \qquad (H.1)$$

All segments are assigned traction free, so the darts must be chosen to cancel the effects of the applied stress. Having solved for all darts, the stress can be found anywhere in the body by superimposing the stress fields of all cracked segments. The stress is calculated at each grain boundary and the stress intensities are found at each crack tip. Grain boundary strengths and toughnesses are assumed to follow an extreme value distribution. Fracture is determined by the weakest segment relative to the current stress on it, or if a crack tip is more critical, by the lowest segment toughness relative to the current local intensity of normal stress across a grain boundary. After the most critical segment is found, it is assumed cracked. Then a new

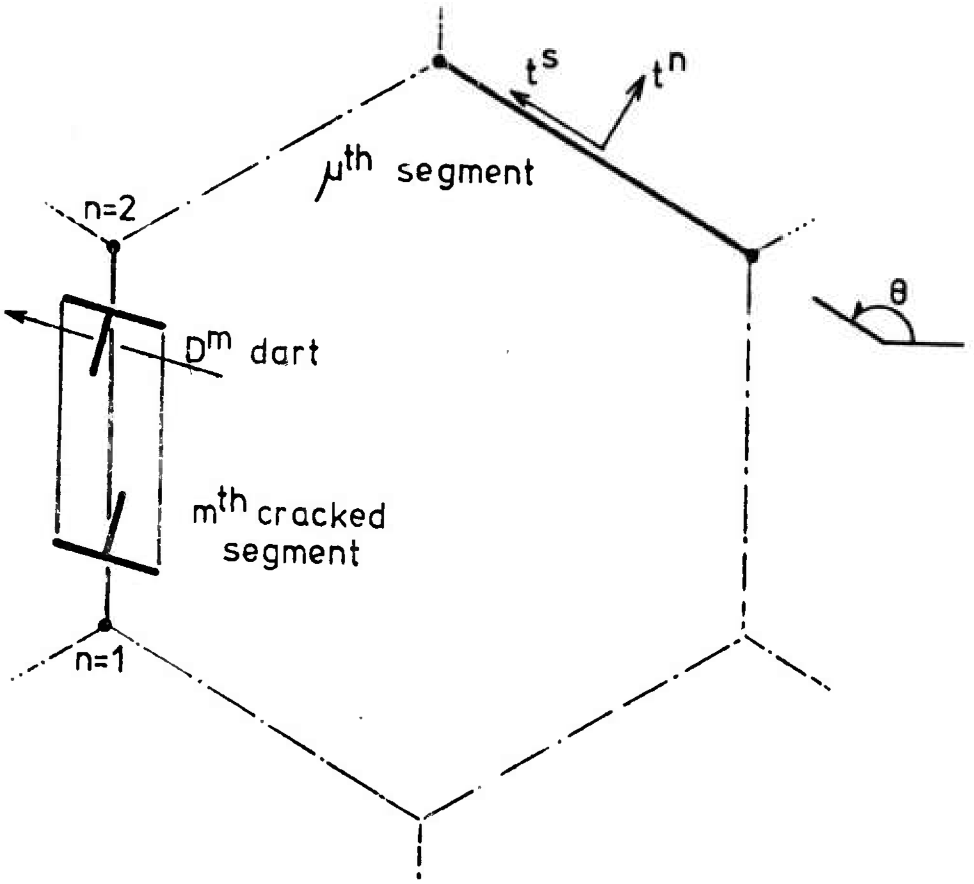

Fig. H.1 The m^{th} cracked segment, modeled as a dislocation dipole, and the resulting traction on the μ^{th} segment.

elastic solution is calculated, a new most critical segment is found, and so on.

A model of surface brittle crack initiation requires the normal and shear stresses at the free surface to be zero. This condition is satisfied by using the stress field of a dislocation near a free surface as given by Head (1953). The equations giving the components of stress at a point (x,y) for the more general case of a dislocation at (x_n, y_n) near an x-axis free surface are given in Appendix H.1. These equations, with f, g and h defined in Appendix H.1 for components of the Burger's vector b_x parallel to and b_y normal to the free surface, take the abbreviated form

$$\begin{aligned} \sigma_{xx} &= f_x\, b_x + f_y\, b_y \\ \sigma_{yy} &= g_x\, b_x + g_y\, b_y \\ \sigma_{xy} &= h_x\, b_x + h_y\, b_y \quad . \end{aligned} \tag{H.2}$$

The mean and deviatoric stress components at z (=x+iy) due to a dislocation at z_n are, in complex form, given by

$$\begin{aligned} \sigma_m &= \frac{\sigma_{xx}+\sigma_{yy}}{2} = \frac{(f_x+g_x)b_x+(f_y+g_y)b_y}{2} \\ \sigma_d &= \frac{(\sigma_{xx}-\sigma_{yy})}{2}+i\sigma_{xy} = \frac{(f_x-g_x)b_x+(f_y-g_y)b_y}{2}+i(h_x b_x+h_y b_y) \quad . \end{aligned} \tag{H.3}$$

The deviatoric part of the stress referred to the normal and shear component along a segment Δz^{μ} at θ to the x-axis, using Mohr circle for the complex plane, is given by:

$$\sigma_{d'} = \sigma_d \; e^{-2i(\theta-\pi/2)} = \sigma_d \left(- \frac{\overline{\Delta z^{\mu}}}{\Delta z^{\mu}} \right) . \qquad (H.4)$$

Giving the components of stress in n,s coordinates as

$$\begin{aligned} \sigma_{nn} &= \sigma_m + R\ell\,(\sigma_{d'}) \\ \sigma_{ss} &= \sigma_m - R\ell\,(\sigma_{d'}) \\ \sigma_{ns} &= Im(\sigma_{d'}) \end{aligned} \qquad (H.5)$$

The traction t^{μ} on the μ^{th} segment due to the m^{th} cracked segment in n,s components, and accounting for the Burger's vector at each end of the dart, is given, after some manipulation of Eqs. H.3 to H.5, by

$$\begin{aligned} t^{\mu} = t_n^{\mu} + it_s^{\mu} &= \left(\sum_{m=1}^{m_{mx}} T_1^{\mu m} D^m + T_2^{\mu m}\,\overline{D^m} \right) \\ &\quad + \sigma_m^{\infty} + \sigma_d^{\infty} \left(- \frac{\overline{\Delta z}}{\Delta z} \right) \end{aligned} \qquad (H.6)$$

where the influence coefficients are:

$$T_1^{\mu m} = \sum_{n=1}^{2} \frac{1}{4} \frac{db^n}{dD^m} \Bigg[(f_x+g_x) - i(f_y+g_y) - \Big((f_x-g_x) - i(f_y-g_y)\Big) \frac{\overline{\Delta z}}{\Delta z} - i2(h_x-ih_y) \frac{\overline{\Delta z}}{\Delta z} \Bigg]$$

$$T_2^{\mu m} = \sum_{n=1}^{2} \frac{1}{4} \frac{db^n}{dD^m} \Bigg[(f_x+g_x) + i(f_y+g_y) - \Big((f_x-g_x) + i(f_y-g_y)\Big) \frac{\overline{\Delta z}}{\Delta z} - i2(h_x+ih_y) \frac{\overline{\Delta z}}{\Delta z} \Bigg]. \tag{H .7}$$

The Burger's vectors are related to the darts through the parameter db^n/dD^m which takes on a value of -1 for n=1 and +1 for n=2.

The influence coefficients of Eq. H.7 are now used in the Brittle Statistics Program BRTST3 (McClintock and Zaverl, 1975) to find the Burger's vectors for a given crack distribution and then Eqs. H.3 are used to find the stress for next cracking.

To minimize the errors in modeling a surface crack by a relative displacement dart its ends are recessed in from the ends of the segment by a fraction $\Delta z^n/\Delta z^m$ of the segment length. The accuracy of the model compared with theoretical and the optimum value of $\Delta z^n/\Delta z^m$ to choose are considered in detail in Appendix H.2. For a value of 0.10 an error of less than 10% was achieved in the mid-segment stresses on neighboring segments and those far from the crack tip. The computed intensity would be low by a factor of 20% . However, this can be compensated for by adjustment of the computational parameter that relates intensities to the grain boundary strengths. Furthermore, the requirements of a stress-free surface are satisfied. Also, if the crack is away from the surface by a distance very much greater than its length, the computed stress field becomes that of an embedded crack within an infinite medium.

The computed effects on the statistics of brittle materials for surface or near surface fracture are discussed after the analytical theory is extended, for comparison, in the next section.

H.3 ANALYTICAL MODEL

The extension to study surface effects of the analytical formulation of Section G.4 is straight-forward. As before the models estimate the maximum strength by finding the density of unit cracks as a function of the applied stress. The probability of aggregation of these cracks is estimated. The maximum strength being achieved when crack length and stresses are sufficiently high to cause crack propagation even with median strengths at the crack tip.

The density p of unit cracks under a given applied stress and corresponding longest contiguous chain of N_c, having probability Φ of forming, are unaffected by the surface. However, the intensities due to surface cracks and the number of possible cracking sites at each tip are different from cracks embedded within the material and with this in mind, the models are extended.

Vertex Orientation

A surface crack, for this orientation, is shown in Fig. H.2, comprising of N_c cracked grains. The average direction of the crack is assumed normal to the applied stress S_1 and has a projected length of $N_c\ 2c_1 \cos 30°$. The intensity of the crack shown, estimated from fracture mechanics (Wigglesworth,1957), is

$$k_{1c} = 1.12\ S_1 \sqrt{2c_1 N_c \cos 30°} \quad . \qquad \text{(H.8)}$$

The normal grain boundary intensity k_θ, for propagation of the crack, is reached when

$$k_\theta = k_{1c} \left((1+\cos 30°)(\cos 15°)/2 \right) = 0.901\ k_{1c} \quad . \qquad \text{(H.9)}$$

For a median value of intensity, noting that there is only

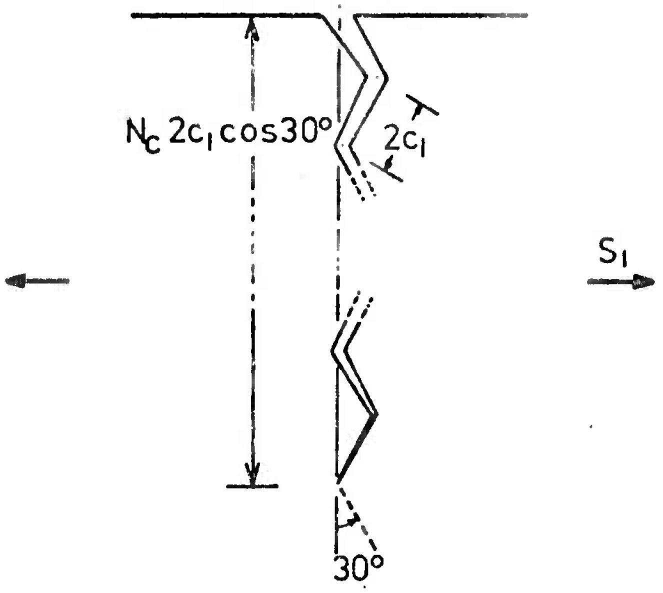

Fig. H.2 Approximating the stress intensity with applied stress for a surface crack in the vertex orientation.

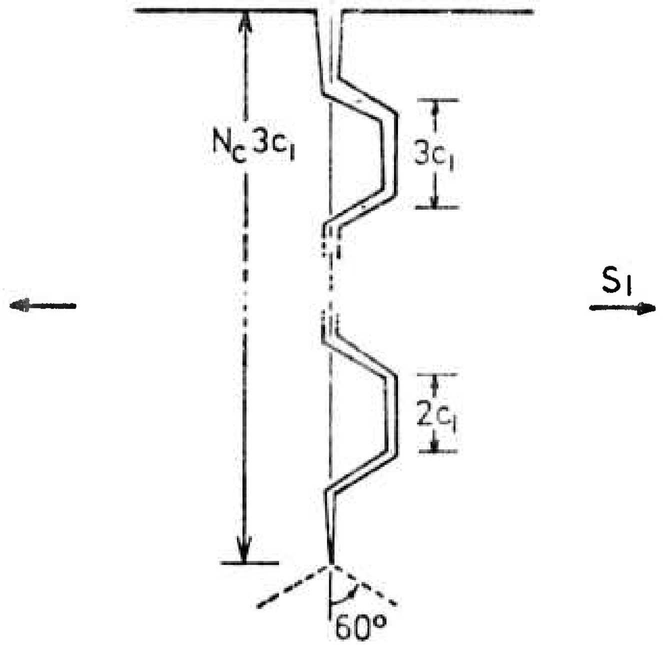

Fig. H.3 Approximating the stress intensity with applied stress for a surface crack in the face orientation.

one possible cracking site at the tip of a surface crack, propagation occurs when

$$0.5 = 1 - \exp\left[-\left(\frac{0.901 \times 1.12\ S_1 \sqrt{2c_1 N_c \cos 30^\circ} - f_{k\theta L} S_L \sqrt{c_1}}{f_{k\theta 0} S_0 \sqrt{c_1} - f_{k\theta L} S_L \sqrt{c_1}}\right)^m\right] . \quad (H.10)$$

For the next segment to crack by nucleation the midsegment stress on the next grain from the normal grain boundary intensity is

$$\sigma_{\theta\theta} = k_\theta / \sqrt{2c_1} \quad . \qquad (H.11)$$

So for a median strength of the next grain, crack growth by renucleation occurs when

$$0.5 = 1 - \exp\left[-\left(\frac{0.901 \times 1.12\ S_1 \sqrt{\quad N_c \cos 30^\circ} - S_L}{S_0 - S_L}\right)^m\right] . \quad (H.12)$$

The maximum stress is obtained as in Section G.4 but using Eqs. H.10 instead of G.15 and H.12 instead of G.17 for crack growth by propagation and renucleation respectively.

Face Orientation

For this orientation the projected crack length is $3c_1N_c$ as shown in Fig. H.3. The corresponding value of normal grain boundary intensity is then

$$k_\theta = \left((1+\cos 60^\circ)(\cos 30^\circ)/2\right) k_{1c} = 0.649\text{x}1.12\ S_1 \sqrt{3c_1N_c}\ . \quad \text{(H.13)}$$

In this case there are two possible cracking sites at the tip of a surface crack. For a median intensity k_θ, propagation occurs when

$$0.5 = 1 - \exp\left[-2\left(\frac{0.649\text{x}1.12\ S_1 \sqrt{3c_1N_c} - f_{k\theta L}S_L\sqrt{c_1}}{f_{k\theta 0}S_0\sqrt{c_1} - f_{k\theta L}S_L\sqrt{c_1}}\right)^m\right]. \quad \text{(H.14)}$$

For a median strength of the next grain crack growth by renucleation occurs when

$$0.5 = 1 - \exp\left[-2\left(\frac{0.649\text{x}1.12\ S_1\sqrt{3/2\ N_c} - S_L}{S_0 - S_L}\right)^m\right] . \quad \text{(H.15)}$$

The maximum stress is obtained as in Section G.4 but using Eqs. H.14 instead of G.29 and H.15 instead of G,31 for crack growth by propagation and renucleation respectively.

H.4 DISCUSSION OF RESULTS

Part sizes up to 1000 grain segments were studied using the numerical model for two different variabilities (m=3,10). The results are shown for the two grain orientations in Figs. H.4 and H.5 and are in fairly good agreement with the values predicted by the analytical

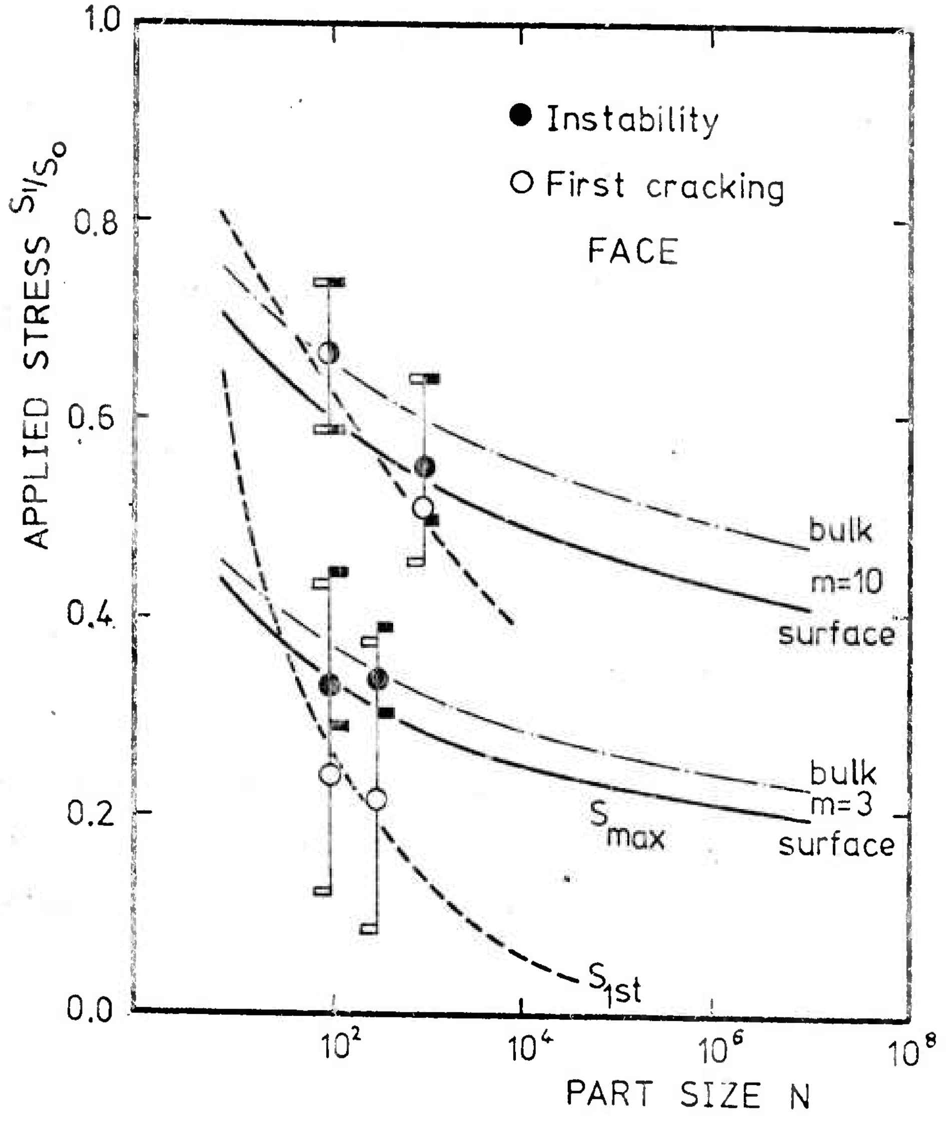

Fig. H.4 Statistical strength for the face orientation as a function of part size for surface initiated fracture. Strength distributions of m = 3 and 10 with $S_L/S_0 = 0$. Samples of 5, giving 93.75% confidence limits for the median.

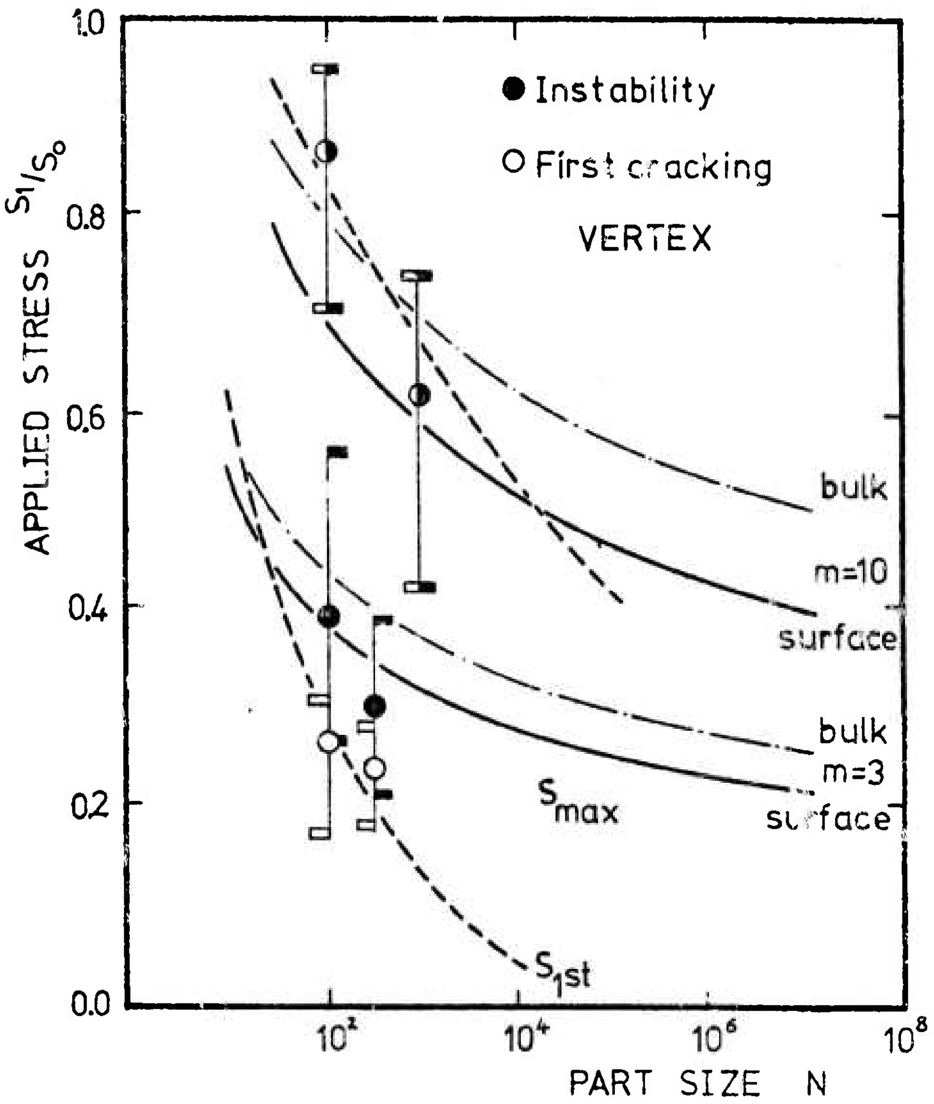

Fig. H.5 Statistical strength for the vertex orientation as a function of part size for surface initiated fracture. Strength distributions of m = 3 and 10 with $S_L/S_0 = 0$.

models. Maximum strengths for surface initiated fracture are 10-20%, depending on orientation and variability, below those for embedded fracture. Consequently, first cracking governs fracture for part sizes larger than embedded fracture, but such part sizes are still small compared with even laboratory size test specimens. The relatively small drop in maximum strengths suggests that the statistical treatment of brittle materials is somewhat independent of whether fracture is initiated in the bulk or at the surface of the material as long as the relevant distribution of grain boundary strengths is used.

APPENDIX H.I. STRESS FIELD OF A DISLOCATION NEAR A FREE SURFACE

The numerical surface model, developed in Section II, requires the normal and shear stresses at the free surface to be zero. This requirement is satisfied by using the stress field, as derived by Head (1953), of a dislocation near a free surface. These equations describing the stresses at a point (x,y) for the more general case of a dislocation at (x_n,y_n) near an x-axis free surface are given below.

For a Burger's vector b_x parallel to the free surface:

$$\sigma_{xx} = b_x \left[E' \left(- v\left(\frac{v^2+3u^2}{(v^2+u^2)^2}\right) + w\left(\frac{w^2+3u^2}{(w^2+u^2)^2}\right) + 2y_n\left(\frac{vw^3-6ywu^2+u^4}{(w^2+u^2)^3}\right)\right)\right] \qquad (\text{H.I.1})$$

$$\sigma_{yy} = b_x \left[E' \left(- v\left(\frac{v^2-u^2}{(v^2+u^2)^2}\right) + w\left(\frac{w^2-u^2}{(w^2+u^2)^2}\right) - 2y_n\left(\frac{(3y+y_n)w^3-6ywu^2-u^4}{(w^2+u^2)^3}\right)\right)\right] \qquad (\text{H.I.2})$$

$$\sigma_{xy} = b_x\left[E'u \left(- \left(\frac{v^2-u^2}{(v^2+u^2)^2} \right) + \left(\frac{w^2-u^2}{(w^2+u^2)^2} \right) - 4y_n y \left(\frac{3w^2-u^2}{(w^2+u^2)^3} \right) \right) \right] \quad . \qquad \text{(H.I.3)}$$

where $u = x-x_n$, $v = y-y_n$, $w = y+y_n$ and for plane strain with Young's modulus E and Poisson's ratio ν

$$E' = \frac{E}{4\pi(1-\nu^2)} \quad . \qquad \text{(H.I.4)}$$

For a Burger's vector b_y, perpendicular to the free surface,

$$\sigma_{xx} = b_y\left[E'u \left(- \left(\frac{v^2-u^2}{(v^2+u^2)^2} \right) + \left(\frac{w^2-u^2}{(w^2+u^2)^2} \right) - 4y_n \left(\frac{(2y_n-y)w^2+(3y+2y_n)u^2}{(w^2+u^2)^3} \right) \right) \right] \qquad \text{(H.I.5)}$$

$$\sigma_{yy} = b_y\left[E'u \left(\left(\frac{3v^2+u^2}{(v^2+u^2)^2} \right) - \left(\frac{3w^2+u^2}{(w^2+u^2)^2} \right) - 12yy_n \left(\frac{w^2-u^2}{(w^2+u^2)^3} \right) \right) \right] \qquad \text{(H.I.6)}$$

$$\sigma_{xy} = b_y \left[E' \left(- v \left(\frac{v^2-u^2}{(v^2+u^2)^2} \right) + w \left(\frac{w^2-u^2}{(w^2+u^2)^2} \right) - \right. \right.$$

$$\left. \left. - 2y_n \left(\frac{-vw^3+6ywu^2-u^4}{(w^2+u^2)^3} \right) \right) \right] . \qquad \text{(H.I.7)}$$

The above equations for σ_{xx}, σ_{yy} and σ_{xy} have been written so that the first term corresponds to the stress field of a dislocation with Burger's vector b, and the second term to the field of a dislocation with Burger's vector $-b$ at the image point $(x_n, -y_n)$. It can be seen that the stress distribution is not just the superposition of the stress fields of the dislocation and an image but the third term in each of the above equations is necessary to give the required zero normal stress on the boundary.

The above Eqs. H.I.1 to H.1.3 and Eqs. H.1.4 to H.I.7 may be superimposed for a dislocation having components of Burger's vector b_x and b_y and for convenience are written in abbreviated form as

$$\sigma_{xx} = b_x f_x + b_y f_y$$

$$\sigma_{yy} = b_x g_x + b_y g_y$$

$$\sigma_{xy} = b_x h_x + b_y h_y \quad . \qquad \text{(H.I.8)}$$

APPENDIX H.II. ACCURACY OF THE SURFACE MODEL

In this Section the accuracy achieved in modelling surface cracks by dislocation dipoles is considered by comparing computed values of stresses and intensities with the theoretical.

A crack of length Δz^m is modelled as a near surface dislocation dipole, by inserting a relative displacement dart D, with ends recessed an amount Δz^n, as shown in Fig.H.II.1 Then the opening mode stress σ_{dip} at y, found from Eq.H.I.1, is

$$\sigma_{dip}=E'D\left[\frac{2(\Delta z^m-\Delta z^n)}{y^2-(\Delta z^m-\Delta z^n)^2}-\frac{2(\Delta z^m-\Delta z^n)(y-(\Delta z^m-\Delta z^n))}{(y+(\Delta z^m-\Delta z^n))^3}\right.$$
$$\left.-\frac{2\Delta z^n}{y^2-(\Delta z^n)^2}+\frac{2\Delta z^n(y-\Delta z^n)}{(y+\Delta z^n)^3}\right] \qquad \text{(H.II.1)}$$

For convenience Eq.H.II.1 is written as

$$\sigma_{dip}=E'D\,F(y,\Delta z^m,\Delta z^n)\ . \qquad \text{(H.II.2)}$$

The midsegment stress due to the dipole must cancel the applied stress σ_∞ so that

$$\sigma_\infty=\left(\sigma_{dip}\right)_{y=0.5\Delta z^m}=E'D\,F(y=0.5\Delta z^m)\ . \qquad \text{(H.II.3)}$$

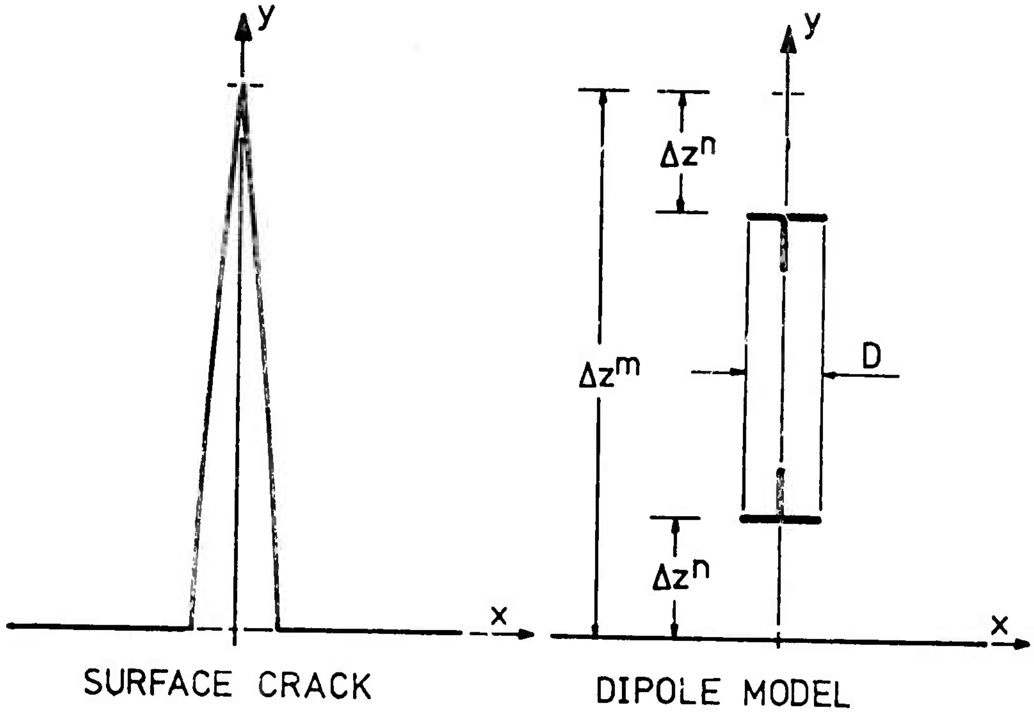

Figure H. II. 1 Surface crack and the corresponding dislocation dipole model.

Solving for the dart D in Eq. H.II.3 gives

$$D = \frac{\sigma_\infty}{E' \; F(y=0.5\Delta z^m)} \quad . \qquad \text{(H.II.4)}$$

Adding in the applied stress at infinity, the total computed opening mode stress σ_{comp} at y is found from Eqs. H.II.2 and H.II.4

$$\sigma_{comp} = \sigma_\infty \left(\frac{F(y, \Delta z^m, \Delta z^n)}{F(y=0.5\Delta z^m)} + 1 \right) . \qquad \text{(H.II.5)}$$

Stress at a Crack Half-length ahead of the Crack Tip

Evaluation of the series solution derived by Wigglesworth (1957), gives the opening mode stress σ_{theo} at a distance $0.5\Delta z^m$ $(y=1.5\Delta z^m)$ ahead of a surface crack as

$$\sigma_{theo} = 1.378 \; \sigma_\infty \quad . \qquad \text{(H.II.6)}$$

The ratio of the computed stress given by the dipole model to the theoretical at a crack half-length ahead of the crack tip, from Eqs. H.II.5 and H.II.6 is then

$$\frac{\sigma_{comp}}{\sigma_{theo}} = \frac{1}{1.378} \left(\frac{F(y=1.5\Delta z^m)}{F(y=0.5\Delta z^m)} + 1 \right) . \qquad \text{(H.II.7)}$$

Eq. H.II.7 is plotted in Fig. H.II.2 for different values of $\Delta z^n/\Delta z^m$.

Stress at Large Distance from the Crack Tip

The theoretical opening mode stress given by Wigglesworth (1957) ahead of a surface crack, length Δz^m, at large distance from the crack tip, approaches the value given by Green and Zerna (1963) for an embedded crack, length $2\Delta z^m$, and is

$$\sigma_{theo} = \sigma_\infty \left(\frac{y}{(y^2 - (\Delta z^m)^2)^{1/2}} \right) \quad . \qquad \text{(H.II.8)}$$

Subtracting out the applied stress, the ratio of computed stress to theoretical, from Eqs. H.II.5 and H.II.8 at large distance from the crack tip is then

$$\left(\frac{\sigma_{comp} - \sigma_\infty}{\sigma_{theo} - \sigma_\infty} \right) = \frac{F(y,\ z^m,\ z^n)}{F(y=0.5\ z^m)} \; \frac{1}{\left[\frac{y}{(y^2 - (\Delta z^m)^2)^{1/2}} - 1 \right]} \quad . \qquad \text{(H.II.9)}$$

The error in computed stresses for $y >> \Delta z^m$ is given by Eq. H.II.9 and is plotted in Fig. H.II.3.

Intensities of the Dipole Model

The theoretical opening mode intensity k_{theo} of a surface crack is given by Wigglesworth (1957) as

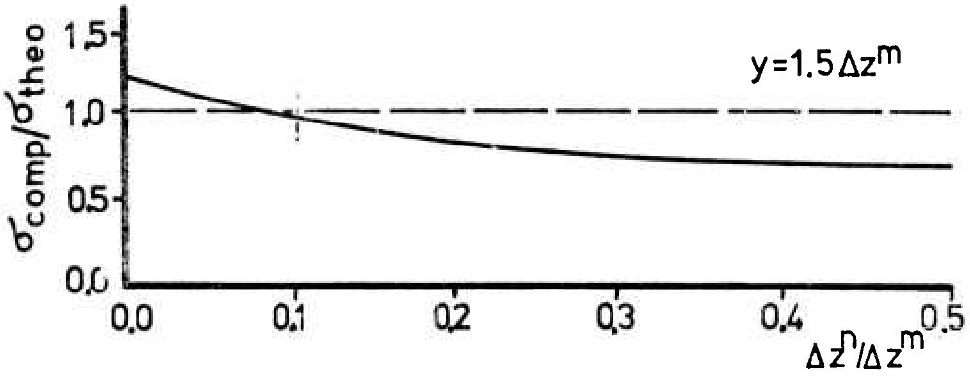

Fig. HII.2 Ratio of the computed stress to theoretical at a half segment length ahead of the crack tip.

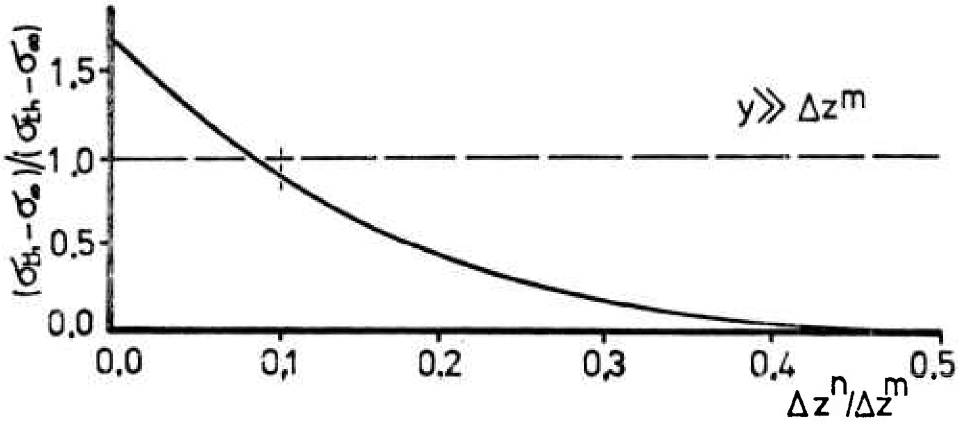

Fig. HII.3 Ratio of the computed stress to theoretical far from the crack tip.

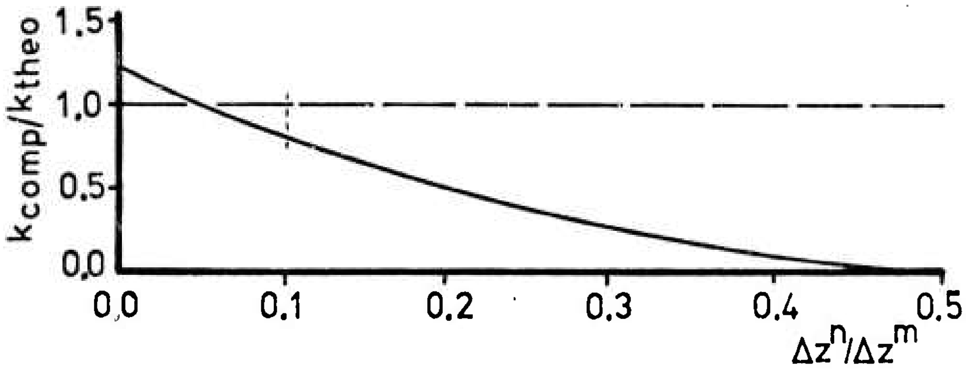

Fig. HII.4 Ratio of the computed intensity to theoretical.

$$k_{theo} = 1.12\ \sigma_{\infty}\sqrt{\Delta z^m} \quad . \qquad \text{(H.II.10)}$$

The intensity k_1 found from the crack opening displacement 2u at a distance δr from the tip, given by Rice (1972), for plane strain is

$$k_1 = \frac{\pi E'}{\sqrt{2\delta r}}\ (2u) \quad . \qquad \text{(H.II.11)}$$

The computed intensity k_{comp} is found from Eq. H.II.11 by approximating the opening displacement by the dart at a crack half-length back from the tip. Dividing Eq. H.II.11 by Eq. H.II.10, and substituting Eq. H.II.4 for the dart, gives the ratio of computed intensity to theoretical:

$$\frac{k_{comp}}{k_{theo}} = \frac{\pi}{1.12\Delta z^m\ F(y=0.5\Delta z^m)} \quad . \qquad \text{(H.II.12)}$$

The error in computed intensities is given by Eq. H.II.12 and is plotted in Fig. H.II.4.

Discussion of the Numerical Surface Model

Figs. H.II.2, H.II.3, and H.II.4 compare the computed values of stresses and intensities with theoretical for different values of $\Delta z^n/\Delta z^m$. For a value of 0.10, an error of less than 10% was found in the midsegment stresses on neighboring segments and those at 'infinity'. The computed intensity would be low by a factor of 20%. However this can be compensated for by adjustment of the computational parameter that relates intensities with the grain boundary strengths. Note that for an embedded crack the optimum value of $\Delta z^n/\Delta z^m$ to choose is 0.14.

H.5 REFERENCES

Green, A. E. and Zerna, W., (1963), Theoretical Elasticity, 1st ed., reprinted 1963, Oxford, 279.

Head, A. K., (1953), "Edge Dislocations in Inhomogeneous Media," Proc. Phys. Soc. Lond., 796-799.

Hildebrand, F. B., (1952), Methods of Applied Mathematics, Prentice-Hall, New York, 228-246.

McClintock, F. A., Zaverl, F., Jr., and R. A. Walter, (1975), "A Computer Model of the Mechanics and Statistics of Brittle Crack Initiation," in manuscript.

Rice, J. R., (1968), "Mathematical Analysis in the Mechanics of Fracture," Fracture, An Advanced Treatise, Vol. II, H. Liebowitz, ed., Academic Press, New York, 191-311.

Wigglesworth, L. A., (1957), "Stress Distribution in a Notched Plate," Mathematika, Vol. 5, London, 67.

I. STRENGTH DISTRIBUTION FROM EXPERIMENTAL DATA

I.1 INTRODUCTION

Accurate strength distribution curves assist the designer in predicting the behavior of brittle components. They can also give insight into ways in which manufacturing techniques can be altered to improve the ultimate performance of the finished product.

The flaw density distributions of brittle materials can be obtained from many different kinds of tests, such as the hardness indentation test and the three or four point bend test. Recently, growing interest in acoustic emission has led to the suggestion that strength distribution can also be obtained by acoustic emission.

I.2 FLAW DISTRIBUTION FROM HARDNESS INDENTATION

State of the Art

Hardness indentation, especially spherical indentation (also known as Hertzian indentation), has been favored by many researchers in their investigations of brittle materials. Because of its ease of application, and because only a small area of the specimen is affected, numerous data can be obtained within a short period of time.

Many workers (Argon, 1959, Sucov, 1962, Oh and Finnie, 1967, Tsai and Kolsky, 1967, Hamilton and Rawson, 1970, and Poloniecki and Wilshaw, 1971) have attempted to calculate the flaw distribution curves from the experimental data, but their methods were either too complicated or of an empirical nature.

Earlier in this research, Matthews, McClintock, and Shack (1976) developed a simple and straight-forward method which made use of only the fracture load from either the three point bend test or the spherical indentation test. In the spherical indentation test, if the specimen with elastic properties E_1 and ν_1, is indented with a sphere of radius R and with elastic properties E_2 and ν_2, the contact radius a which is a function of the applied load P, is

$$a(P) = \left[\frac{3PR}{4}\left(\frac{1-\nu_1^{\,2}}{E_1} + \frac{1-\nu_2^{\,2}}{E_2}\right)\right]^{\frac{1}{2}} . \qquad (I.1)$$

Outside the contact circle $r = a$ the radial stress σ_{rr} at the surface is tensile:

$$\sigma_{rr} = \frac{1 - 2\nu_1}{2\pi} \frac{P}{r^2} \qquad (r \geq a) . \qquad (I.2)$$

The maximum tensile stress σ_m is at the contact circle:

$$\sigma_m = \frac{1 - 2\nu_1}{2\pi} \frac{P}{a^2} . \qquad (I.3)$$

If the flaw density $g(\sigma)$ is defined such that $g(\sigma)\, d\sigma$ is the number of flaws per unit area of strength between σ and $\sigma + d\sigma$, and if the probability of failure for a stress less than

σ_m is $\Phi(\sigma_m)$, then, for the spherical indentation test,

$$g(\sigma_m) = \frac{\sigma_m}{\pi a^2}\left\{\frac{\Phi''(\sigma_m)[1-\Phi(\sigma_m)]+[\Phi'(\sigma_m)]^2}{[1-\Phi(\sigma_m)]^2}\right\} . \qquad (I.4)$$

$\Phi(\sigma_m)$ can be ordered from the experimental data, and by differentiating it twice, $g(\sigma_m)$ is obtained.

In order to record the load at which ring cracking starts, the indented area must be observed continuously during the test. If the specimen is transparent (e.g. glass), observation can be made with an optical microscope from the side or the bottom of the specimen. If the specimen is opaque (e.g. silicon nitride), Evans and Wilshaw (1976) suggested that the initiation of cracks can be detected by acoustic emission. The following alternate method was proposed by Lawn (1968). With the maximum load as variable, a systematic series of indentations was performed. The specimen was then viewed to find out which indentations had produced ring cracks. The critical fracture load could be determined to within about 5%.

Mathews et al applied their analysis to the test results of Argon, Hori, and Orowan (1960) to obtain the flaw density curves. Their method has also been applied successfully by Evans and Wilshaw (1977). Evans and Jones (1977) have even extended their analysis to the tensile test, the four point bend test, the expanded ring test, and the concentric ring test.

The Friction Effect with Spherical Indenter

It was pointed out by Rawson (1977) that the analysis of Matthews et al overlooked the frictional forces at the interface between the indenter and the substrate, when these components have different elastic properties. These forces will change the stress distribution on the surface of the specimen, and the apparent flaw density curve will be affected. Johnson, O'Connor, and Woodward (1973) have calculated the stress distribution for two extreme cases of complete slip and no slip. In reality, the indenter will slip in an annulus, the exact size and location of which depends on the elastic properties and the friction coefficient. The maximum stress when a rigid ball is indented on a less rigid surface (e.g. steel indenter on glass surface) occurs not at the contact circle as predicted by the Hertzian theory, but at a short distance outside it. Thus, the ring crack should start outside the contact circle. This finding is in qualitative agreement with the experimental results of Argon et al (1960) as well as that of other workers, although some of the observed effect is associated with the statistical variability of fracture (Oh and Finnie, 1970, Hamilton and Rawson, 1970).

Johnson et al have prepared two curves which are reproduced here in Figs. I.1 and I.2. From these two curves, once the constant κ in terms of the elastic properties:

$$\kappa = \frac{\dfrac{(1+\nu_1)(1-2\nu_1)}{E_1} - \dfrac{(1+\nu_2)(1-2\nu_2)}{E_2}}{\dfrac{1-\nu_1^2}{E_1} + \dfrac{1-\nu_2^2}{E_2}} \qquad (I.5)$$

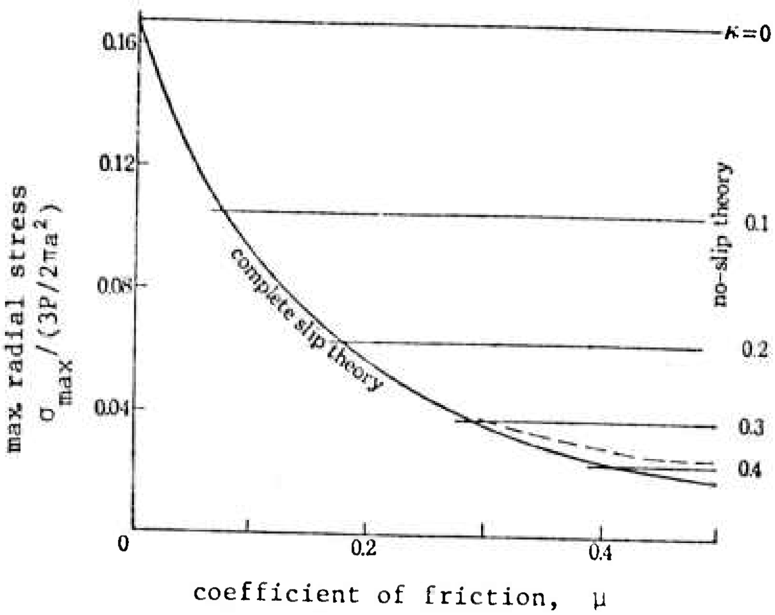

Fig. I.1 Maximum values of the radial tensile stress (a) as a function of κ (no-slip theory) and (b) as a function of μ (complete slip theory). An estimated curve (chain line) is interploated between the complete slip theory and no-slip theory for κ = 0.4.

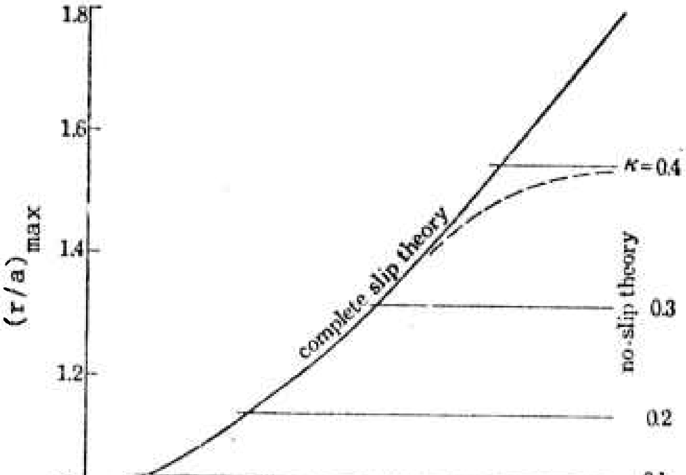

Fig. I.2 Position of the maximum radial tensile stress (a) as a function of κ (no-slip theory) and (b) as a function of μ (complete slip theory). An estimated curve (chain line) is interpolated for κ = 0.4.

and the friction coefficient μ are known, a reasonable interpolation between the complete slip theory and the no slip theory is possible. For example, with a steel indenter and a clean glass surface, Johnson et al measured an initial friction coefficient of only 0.12, and assuming $E_{steel} = 2.07 \times 10^5 MN/m^2$, $E_{glass} = 6.90 \times 10^4 MN/m^2$, $\nu_{steel} = 0.30$, $\nu_{glass} = 0.25$, κ is 0.364. From Figs. I.1 and I.2, it can be said that the complete slip theory would be a better approximation. The stress distribution assuming complete slip is plotted in Fig. I.3.

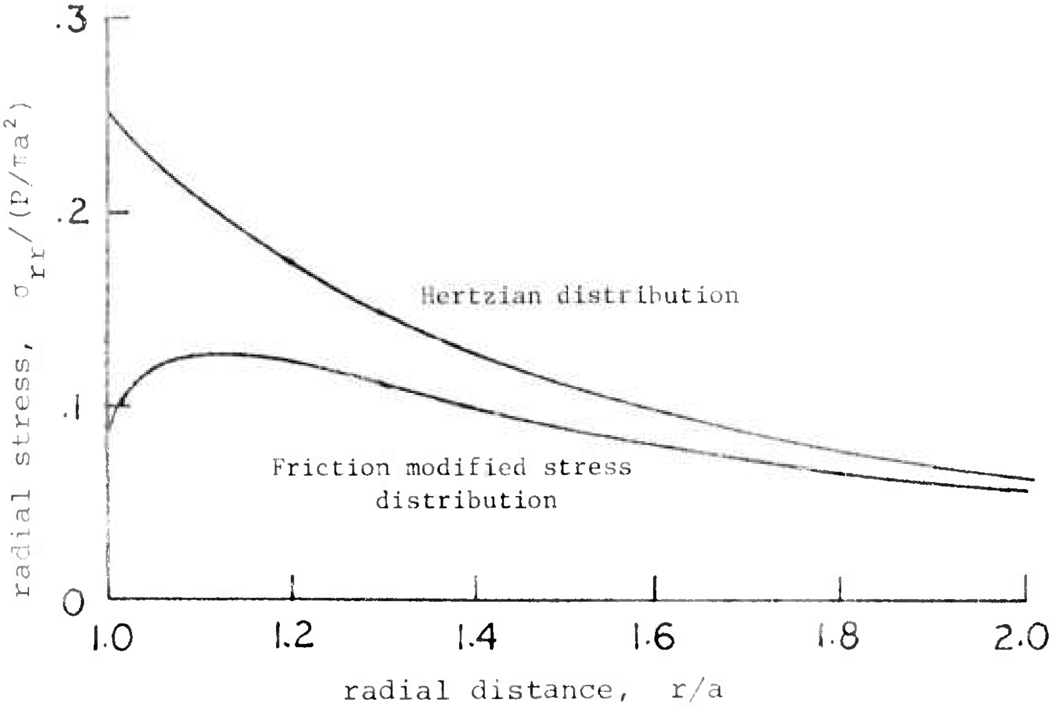

Fig. I.3. Surface radial stress distribution of steel ball indenting on glass specimen. (a) Hertzian distribution, friction neglected. (b) Friction modified stress distribution assuming complete slip, $\kappa = 0.364$, and $\mu = 0.12$.

The maximum tensile stress is located around $r/a = 1.12$.

To minimize the friction effect, the indenter and the specimen should have similar elastic properties, or the interface should be lubricated with high pressure greases such as those that contain graphite, molybdenum disulphide, or fatty acids. On the other hand, the analysis developed by Matthews et al would be much more useful if it could be modified to account for the friction by assuming a stress distribution that reached a maximum at $r = r_m (r_m > a)$. Such work is being carried out as part of a subsequent project.

Plane Strain Cylindrical Indentation including Friction

Although a spherical indenter is ideal for studying surface flaws in brittle materials, a different shape of indenter would be needed to study sub-surface flaws. Such an indenter should give no stress on the specimen surface so that fracture will not originate at the surface. A cylindrical indenter with its axis parallel to the surface (Fig. I.4) does not generate any stress

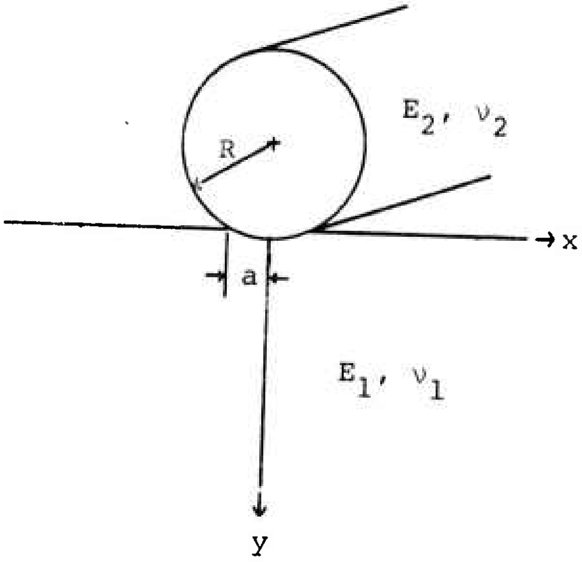

Fig. I.4. Plane strain cylindrical indentation.

on the surface outside the contact area and produce only compressive stresses in the interior. A cylindrical indenter is also useful in modelling the contact between a car wheel and a rail, or between a roller bearing and the inner or outer ring.

The elastic stress distribution of plane strain cylindrical indentation can be found in McClintock (1977) or Poritsky (1950) in complex form:

$$\frac{\sigma_{xx} + \sigma_{yy}}{2} = \frac{2P}{\pi a} \operatorname{Im} \left[\frac{z}{a} + \sqrt{\left(\frac{z}{a}\right)^2 - 1} \right]^{-1} . \qquad (I.6)$$

$$\frac{\sigma_{xx} - \sigma_{yy}}{2} - i\,\sigma_{xy} = -\frac{2P}{\pi a} \left[\frac{y/a}{\frac{z}{a} + \sqrt{\left(\frac{z}{a}\right)^2 - 1}} \right] \left[\frac{1}{\sqrt{\left(\frac{z}{a}\right)^2 - 1}} \right] \qquad (I.7)$$

where $z = x + iy$,

and a = contact half-width

$$= \left[\frac{4PR}{\pi} \left(\frac{1 - \nu_1^{\,2}}{E_1} + \frac{1 - \nu_2^{\,2}}{E_2} \right) \right]^{\frac{1}{2}} \qquad (I.8)$$

When a brittle material is under biaxial stresses, Griffith (1924) showed that when the smaller stress σ_2 is in the range $-3\sigma_t \leq \sigma_2 \leq \sigma_1$, fracture takes place when the algebraically larger stress σ_1 reaches the tensile strength σ_t of the material. When σ_2 is in the range $\sigma_2 < -3\sigma_t$, fracture takes place when

$$(\sigma_1 - \sigma_2)^2 + 8\sigma_t(\sigma_1 + \sigma_2) = 0 \qquad \text{(I.9)}$$

Solving for σ_t ,

$$\sigma_t = -\frac{(\sigma_1 - \sigma_2)^2}{8(\sigma_1 + \sigma_2)} \qquad \text{(I.10)}$$

With the principal stresses σ_1 and σ_2 calculated from the stress distribution functions (Eqs. I.6 and I.7), the maximum value for σ_t is found to occur along the axis at a depth of $y/a = 1.25$. McClintock and Walsh (1962) modified Griffith's criterion by considering the effect of crack closure with friction. If σ_c is the normal stress to close a crack, and μ is the coefficient of friction, they showed that the condition for fracture after the cracks have closed is

$$\mu\,(\sigma_2 + \sigma_1 - 2\sigma_c) + (\sigma_1 - \sigma_2)\sqrt{1 + \mu^2} = 4\,\sigma_t\sqrt{1 - \frac{\sigma_c}{\sigma_t}} \,. \qquad \text{(I.11)}$$

By assuming that the first crack caused instability, they were able to fit past experimental data well with values of μ of 1.0, and σ_c of $-3\sigma_t$. Using these values, the maximum value of σ_t is found to be along the axis at $y/a = 2.05$. Therefore, either the Griffith's criterion or the modified criterion predicts fracture in compression to start along the axis in the interior of the specimen.

Plane strain cylindrical tests were performed by Thomas and Hoersch (1930) who tested on steel plates, and Kolsky (1952) who tested on both glass and "Perspex" (polymethylmethacrylate). Kolsky, using steel indenters of radius of curvature of 12 inches, found that the glass specimens fractured along the outer edges of the area of contact. A similar problem of compressing glass cylinders between two steel plates was investigated by Hooper (1971). Hondros (1959) showed that both principal stresses become compressive in the loading zones, with a surface value equal to the applied normal stress. The maximum tensile stress occurs at the center of the cylinder. Therefore, fracture is expected to initiate from the center of the cylinder. However, Hooper (1971) found from experiments that fracture started from the surface of the cylinder.

Hooper suggested that the frictional forces at the interface due to the mismatch of elastic properties induced tensile stresses at the edges of the contact zone. He solved the surface stress distribution for two extreme cases of complete slip and complete adhesion, but his results are too lengthy to be included here. Applying his equations to the problem of a glass surface indented with a steel cylinder, it can be shown that tensile stresses exist at the edges of the contact zone. He attempted to reduce the friction effect by applying high pressure lubricants. He observed that the failure load using dry platens was approximately 35% higher than that obtained using greased platens, a result which is in general agreement with the theory.

Hooper also suggested that since a cylinder has a finite length, the stress distribution is actually three-dimensional, and the plane strain distribution is not adequate to describe the problem. The solution for the elliptical pressure distribution in an elastic half-space due to a rectangular contact area was given by Kunert (1961). His analysis predicted the existence of tensile stresses along the edges of the contact zone if the length of the cylinder is less than approximately 40 times the contact half-width.

I.3 STRENGTH DISTRIBUTIONS FROM ACOUSTIC EMISSION

Acoustic Emission and Brittle Materials

Acoustic emissions are the stress waves originating from strain energy release as a result of various physical and structural changes within the material caused by the applied stress.

The strain energy released in the formation or growth of micro-cracks prior to maximum load, observed, for example, by Evans (1974), is thought to be the cause of acoustic emission in many polycrystalline ceramics and possibly other materials that exhibit barely any dislocation motion at room temperature. Also, as would be expected, no acoustic emission is observed from amorphous brittle materials, except at the onset of catastrophic failure (Noone, 1973). Others, such as Graham and Alers (1973), have observed a relationship between detected acoustical events and fractured grains and for Lucalox found a one-to-one correspondence. Noone (1973) in the same material similiarly attributed a single acoustical event with the parting of two grain surfaces.

The above strongly suggests that for many brittle materials any detected acoustic emission is due to the formation of stable micro-cracks and not due to other mechanisms such as dislocation motion.

Obtaining the Statistical Parameters

The formation of stable micro-cracks at stresses below the ultimate fracture load suggests that the general method of McClintock and Zaverl (1976) can be used to obtain the statistical parameters m, S_0 and S_L that govern crack initiation in grain boundaries, idealized as an extreme value distribution of the third asymptotic kind.

The approach to be taken is similiar to the analysis of Evans et al (1974). However, it is shown here that the number of micro-cracks is largely a function of the applied stress level and that time-dependent effects are usually only of minor importance. The acoustic emission data of Evans et al (1974) is shown in Fig. I.5 plotted in terms of 'count-rate' against applied stress for polycrystalline alumina ('Lucalox') for a test conducted at constant stress rate $\dot{S}$. From the data, with r the gradient of the straight line, the count-rate $\frac{dn}{dt}$ is given in terms of the stress S and constant C_s by

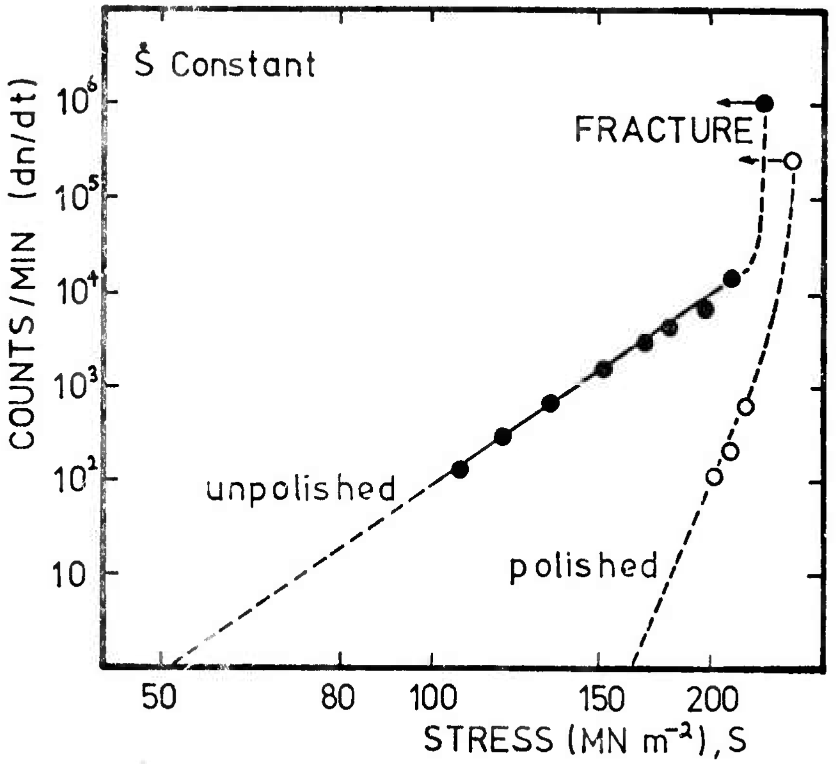

Fig. I.5 Acoustic emission count rate against applied stress for Lucalox by Evans, Russel and Linzer, (1974).

$$\log\left(\frac{dn}{dt}\frac{C_s}{\dot{S}}\right) = r \log S - r \log C_s . \qquad (I.12)$$

The observations of Graham and Alers (1973) and Noone (1973) suggest that the number of counts n is related to the number of micro-cracks N_t in terms of a constant D so that

$$\frac{dn}{dt} = D\frac{dN_t}{dt} = D\dot{S}\frac{dN_t}{dS} . \qquad (I.13)$$

It turns out that the slight stress dependence of D, as proposed by Tetelman (1973), affects the calculated number of micro-cracks by only 10 - 20%, and may be neglected. Combining Eqs. I.12 and I.13 leads to

$$\frac{dN_t}{dS} = \frac{1}{C_s D}\left(\frac{S}{C_s}\right)^r . \qquad (I.14)$$

Integrating Eq. I.14, taking the lower limit as zero gives

$$N_t = \frac{1}{D(r+1)}\left(\frac{S}{C_s}\right)^{r+1} \qquad (I.15)$$

The analytical theory of McClintock and Zaverl (1975) given an equation of similiar form for $S_L = 0$ and part-size N grain boundary segments,

$$N_t = N\left(\frac{S}{S_0}\right)^m . \qquad (I.16)$$

From Eqs. I.15 and I.16 the extreme value exponent m is

$$m = r+1$$

and the parameter S_0 is

$$S_0 = C_s \left(N(r+1)D \right)^{1/(r+1)}$$

For the unpolished specimen $m \doteq 7$. The effect of polishing was to significantly reduce the amount of acoustic activity as well as increasing m to about 25 . This suggests that many of the low strength grains, damaged during manufacturing and machining, have been removed from the surface by polishing. Removal of the low strength cracks during polishing would account for the low acoustic activity from optically finished samples of zinc selenide as observed by Evans (1976). In fact the amount of precursor acoustic emission, being first detected at 90% of the fracture stress, was of such small size that application of the above method was not possible. It is recommended that numerical modelling of unpolished surfaces be carried out using the surface model, as described in Chapter 3, with prexisting cracks.

I.4 REFERENCES

Argon, A. S., (1959), "Surface Cracks on Glass," Proc. R. Soc. Lond, A250. 482-492.

Argon, A. S., Hori, Y., and Orowan, E., (1960), "Indentation Strength of Glass," J. Am. Ceramic Soc., 43, 86-96.

Evans, A. G. and Jones, R. L., (1977), "Evaluation of a Fundamental Approach for the Statistical Analysis of Fracture," submitted to J. Am. Ceramic Soc.

Evans, A. G., Linzer M., and Russel, L. R., (1974), "Acoustic Emission and Crack Propagation in Polycrystalline Alumina," Mat. Sci. & Eng., 15, 253-261.

Evans, A. G. and Nadler, H., (1976), "An Acoustic Emission Study of the Fracture of Zinc Selenide," Mat. Sci. & Eng., 22, 7 - 14.

Evans, A.G. and Wilshaw, T. R., (1976), "Quasi-static Solid Particle Damage in Brittle Solids - I. Observations, Analysis, and Implications," Acta Met., 24, 939 - 956.

Evans, A. G. and Wilshaw, T. R., (1977), "Dynamic Solid Particle Damage in Brittle Materials: An Appraisal," J. Mat. Sci. 12, 97.

Graham, L. J. and Alers, G. A., (1973), "Microstructural Aspects of Acoustic Emission Generation in Ceramics," Fracture Mech. of Ceramics, Vol. 1, R. C. Bradt, D.P.H. Hasselman, and F. F. Lange, eds., Plenum Press, New York, 175-188.

Griffith, A. A., (1924), "The Theory of Rupture," Proc. 1st Intl. Congress of Appl. Mech., J. Waltman, Jr., ed., Delft, Holland, 55-63.

Hamilton, B., and Rawson, H., (1970), "The Determination of the Flaw Distributions on Various Glass Surfaces from Hertz Fracture Experiments," J. Mech. Phys. Solids, 18, 127.

Hondros, G., (1954), "The Evaluation of Poisson's Ratio and the Modulus of Materials of a Low Tensile Resistence by the Brazilian (Indirect Tensile) Test with Particular Reference to Concrete," Aust. J. Appl. Sci., 10, 243-268.

Hooper, J. A., (1971), "The Failure of Glass Cylinders in Diametral Compressions," J. Mech. Phys. Solids, 19, 179-200.

Johnson, K. L., O'Connor, J. J., and Woodward, A. C., (1973), "The Effect of the Indenter Elasticity on the Hertzian Fracture of Brittle Materials," Proc. R. Soc. Lond., A 334, 95-117.

Kolsky, H., (1952) "A Photoelastic Investigation of the Hardness of Plastics and Glass," J. Soc. Glass Technology, 36, 56-64.

Kunert, K., (1961), "Spannungsverteilung im Halbraum bei Elliptischer Flächenpressungsverteilung über einer Rechteckigen Druckfläche," Forsch. Geb. IngWes., 27, 165-174.

Lawn, B. R., (1968), "Hertzian Fracture in Single Crystals with the Diamond Structure," J. Appl. Phys., 39, 4828.

Matthews, J. R., McClintock, F. A., and Shack, W. J., (1976), "Statistical Determination of Surface Flaw Density in Brittle Materials", J. Am. Ceramic Soc., 59, 304-308.

McClintock, F. A., (1977), "Plastic Flow Around a Crack under Friction and Combined Stress," Proc. 4th Intl. Conference on Fracture, Vol. 4, D.M.R. Taplin, ed., Waterloo, Canada, 49-64.

McClintock, F. A., and Walsh, J. B., (1962), "Friction on Griffith Cracks in Rocks under Pressure," Proc. 4th U.S. Natl. Cong. Appl. Mech., Vol. 2, 1015 - 1022.

McClintock, F. A., Zaverl, F. Jr., and Walter, R. A., (1975), "A Computer Model of the Mechanics and Statistics of Brittle Crack Initiation," in manuscript.

McClintock, F. A. and Zaverl, F., Jr., (1977), "An Analysis of the Mechanics and Statistics of Brittle Crack Initiation," to appear in Int. J. of Fracture.

Noone, M. J., and Mehan, R. L., (1973), "Observation of Crack Propagation in Polycrystalline Ceramics and its Relationship to Acoustic Emissions," Fracture Mechanics of Ceramics, Vol. I, R. C. Bradt, ed., Plenum Press, New York, 201-230.

Oh, H. L., and Finnie, I., (1967), "The Ring Cracking of Glass by Spherical Indenters," J. Mech. Phys. Solids, 15, 401.

Oh, H. L., and Finnie, I., (1970), "On the Location of Fracture in Brittle Solids - I. due to Static Loading," Int. J. Fracture Mech., 6, 287.

Poloniecki, T. D., and Wilshaw, T. R., (1971), "Determination of Surface Crack Size Densities in Glass," Nature: Phy. Sci., 229, 226-227.

Poritsky, H., (1950), "Stresses and Deflections of Cylindrical Bodies in Contact with Application to Contact of Gears and of Locomotive Wheels," J. Appl. Mech., 17, 191.

Rawson, H., (1977), "Comments on 'Statistical Determination of Surface Flaw Density in Brittle Materials'," to appear in J. Am. Ceramic Soc.

Sucov, E. W., (1962), "New Statistical Treatment of Ball Indentation Data to Determine Distribution of Flaws in Glass," J. Am. Ceramic Soc., 45, 214.

Tetelman, A. S. and Evans, A. G., (1973), "Failure Prediction Using Fracture Mechanics and Acoustic Emission," Fracture Mechanics of Ceramics, Vol. II, R. C. Bradt, ed., Plenum Press, New York, 895-924.

Thomas, H. R. and Hoersch, V. A., (1930), "Stresses Due to the Pressure of One Elastic Solid Upon Another," U. Ill. Eng. Exp. Station Bulletin, No. 212.

Tsai, Y. M., and Kolsky, H., (1967), "A Theoretical and Experimental Investigation of the Flaw Distribution on Glas Surfaces," J. Mech. Phys. Solids, 15, 29.

J. FLAW DETECTION BY SCATTERED LIGHT

J.1 INTRODUCTION

A flaw detection technique is useful when fracture occurs through the propagation of preexisting cracks. Attempts can then be made to detect these cracks at test stresses low enough to avoid premature component failure.

It was shown by McClintock and Hahn (1975) that an impractical number of tests would be necessary to accurately determine the tail of the flaw distribution curve, where low strength cracks cause failure to occur well below the mean strength. Consequently, failure rate predictions cannot be made using empirical strength distribution curves. A method of non-destructive evaluation of laser windows is required which will increase confidence in reliability estimates without impairing the serviceability of the inspected component. The possibility of using the scattering of light from cracks is explored by dark field viewing of pre-cracked glass test specimens.

J.2 THEORETICAL ANALYSIS

In order to evaluate a possible flaw detection technique the sizes of typical strength impairing cracks must be found. The length 2c of cracks in brittle laser window materials can be obtained from the fracture toughness K_{Ic} and the nominal critical fracture strength σ_c,

$$K_{Ic} = \sigma_c\sqrt{\pi c} \quad . \tag{J.1}$$

The corresponding total crack opening displacement $2u_y$ of an internal crack under a test stress σ_t is given for plane strain by Green and Zerna (1973) in terms of the distance x from the center of the crack, Poisson's ratio ν , and the shear modulus G by

$$2u_y = \frac{2\sigma_t\ (1-\nu)}{G}(c^2-x^2)^{1/2} \quad . \tag{J.2}$$

For example, in zinc selenide with $K_{Ic} = 0.75$ MN/m$^{3/2}$ (McClintock and Hahn, 1975) a crack causing failure at 6500 psi would have a half-length of 90 μm and a maximum center opening, at a third of the fracture stress, of 0.08 μm. Equation J.2 is plotted in Fig. J.1 showing the maximum crack opening displacemtns of cracks of different strengths under different test loads that would be expected in zinc selenide. A flaw detection technique must be capable of detecting cracks of magnitude which

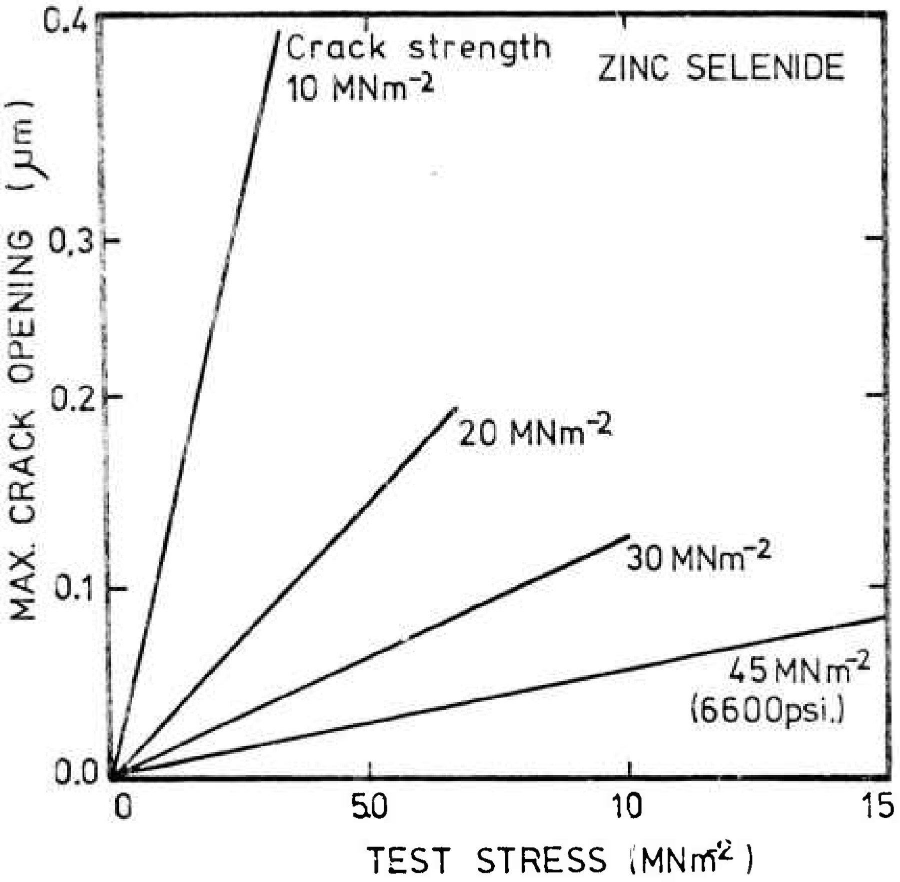

Fig. J.1 Predicted maximum openings of cracks having different strengths under different test loads for zinc selenide.

are deemed critical, typically with openings between 0.02 μm and 0.10 μm depending on the material, in order to be applied to such high strength laser windows.

For scattering a surface crack can be considered to be equivalent to a thin gap between two homogeneous media. Bloembergen (1975) showed that, for cracks with openings small compared with the wavelength λ of the electromagnetic radiation passing through the material having refractive index n, fraction of scattered light I_s emitted for normal incidence is given by

$$I_s = \left(\frac{\pi(n^2-1)}{n}\right)^2 \left(\frac{2u_y}{\lambda}\right)^2 \quad . \qquad (J.3)$$

Such scattering of light from cracks suggests a possible method of detecting the more open low strength cracks and even the shorter cracks in higher strength laser windows.

Applying a small load, of say 10 to 30% of the design stress, will tend to open any preexisting surface microcracks, which might be closed or disguised by smearing-over due to polishing. If light, or whatever short wavelength electromagnetic radiation can be transmitted, is directed through the edge of the window running parallel with and immediately below the surface in tension, any cracks present could be located by the scattered radiation.

J.3 EXPERIMENTAL OBSERVATION AND DISCUSSION

The light scattered from precracked glass test specimens, whilst under under carbon-arc illumination, was viewed against a dark field. The precise crack opening was subsequently established using a scanning electron microscope. Cracks with openings of about 0.1 μm and greater have been observed by this method. Visual detection of any scattered light was found to be the most effective, whereas photographic detection using high speed, 3000 ASA, film required exposure times of about 120 secs.

Minimum observed crack openings are between one and five times greater than maximum openings of typical median strength impairing flaws under loading of 10-30% of the design stress. However, the depths of such flaws would be only about a tenth of the cracks viewed in glass. Furthermore, some laser window materials, zinc selenide for example, are only transparent to wavelengths longer than visible. Consequently, scattered intensities from cracks in such high strength material would be reduced by a factor of about 50 for calcium fluoride to about 1000 for zinc selenide.

It is concluded that until scattered intensities can be increased or detection methods improved, proof testing must be used to increase brittle structure reliability. However, a scattered light technique could prove useful in detecting the critical, but relatively rare, low strength cracks responsible for the uncertainty in the tail of experimentally determined strength distribution curves. It is therefore recommended that further tests be carried out on the optically transparent brittle laser window materials, to establish the extent to which such cracks can be detected.

J.4 REFERENCES

Bloembergen, N., (1975), Private Communication.

Green, A. E., and Zerna, W., (1963), Theoretical Elasticity, 1st ed., reprinted 1963, Oxford, 279.

McClintock, F. A., and Hahn, W., (1975), "Design of Brittle Components Using Flaw Analysis," in N.J. Grant et al, Research on Materials for High Power Laser Windows, Final Technical Report, AFCRL-TR-76-0027.

K. SUMMARY

The space charge theory for ionic materials has been modified to include a secondary interaction force between an aliovalent ion and a grain boundary or surface which acts in addition to the usual electrostatic interaction forces. In a purely ionic system such a force would likely arise from an ion size misfit, i.e., a strain energy which is relieved near the boundary. The space charge problem has been reformulated to include such a force. Numerical solutions show that the electrostatic field and the distribution of solute ions and defects near the boundary are substantially modified by the coupling of the two interactions through the required satisfaction of Poisson's equation by all charged species. Solutions were also obtained for the case of two solute ions with different strain interaction forces. The distributions of the two ions are found to be interdependent.

Boundary mobility calculations were performed taking the secondary interaction and the modifying effect on the space charge cloud into account. Because of uncertainty about the form of the strain field and the velocity dependence of the electrostatic field the resulting calculations have more uncertainties than do the calculations for the purely electrostatic case. Nevertheless some interesting results are indicated. The mobility is affected most strongly at temperatures near the isoelectric temperature. Here the strain interactions induce much stronger electrostatic forces than would otherwise exist. These are apparently helpful in preventing breakaway of the boundary from the solute could. The theory predicts that the effectiveness of divalent solutes in inhibiting boundary motion should increase in the order of Ba^{+2}, Sr^{+2}, to Ca^{+2}.

In many cases it is physically possible for a boundary to breakaway from its solute cloud and move at the much higher intrinsic mobility. At intermediate driving forces this apparently happens by a spatial fluctuation of the boundary which induces a nonuniform distribution of solute along the boundary. The more rapidly moving parts of the boundary accelerate and shed the solute cloud. This breakaway region can spread laterally and carry the entire boundary into the high velocity mode. Such rapidly moving boundaries can then cause much faster recrystallization or discontinuous grain growth. Thus, breakaway of a boundary from the solute cloud can be an important step in controlling recrystallization in forged materials as well as in preventing discontinuous grain growth and pore entrapment during sintering of oxides. A nonlinear perturbation analysis was used to indicate the conditions under which such breakaway can occur.

For typical oxides four possible mechanisms may control the grain boundary mobility. These are the intrinsic mobility, solute drag, pore or particle drag, and liquid phase control. These have been evaluated to consider the relative importance and possible mechanisms for transitions among the regimes suggested. The particular mechanism controlling the mobility can affect the kinetics of grain growth and the resulting grain morphologies. A survey of the data for many ceramics indicates qualitative agreement with theory.

Single crystals of CaF_2 were hot forged at temperatures between 0.46 (475°C) and 0.92 (1230°C) of the melting point. The flow stress temperature curve was found to have a mild orientation dependence for $T \leq 0.65\ T_m$ with $\sigma_{<100>} > \sigma_{<110>} > \sigma_{<111>}$. The subcell size was found to be inversely proportional to the forging stress. At $T \geq 0.65\ T_m$ recrystallization occurred during forging. The nature of the microstructure developed depends upon the crystal orientation. In general <100> crystals have more uniform, equiaxed subgrains, compared to <111> crystals which tended to be more nonuniform with elongated subgrains. At lower temperatures the microstructures were less uniform, especially in the <111> crystals in which deformation bands were common. Crystals forged in the <100> direction showed less tendency to crack during forging or cooling than <111> crystals.

At lower temperatures the subgrain boundaries are less well knit and contain considerable excess or extrinsic dislocations. At higher forging temperatures the subgrain boundaries become equilibrated and there are fewer if any extrinsic dislocations found within them. The specific dislocation reactions involved in sub-boundary equilibration were identified. The misorientation angles of the sub-boundaries are of the order of a degree although there is an indication of a bimodal distribution in which lower angle subcells form within higher angle subgrains.

Models were developed for calculating the effects of microcracking and microcrack coalescence on fracture behavior and statistics. The problem is to determine the maximum stress at which catastrophic crack propogation occurs in a body containing a distribution of subcritical flaws. From the models the stresses for first cracking and for failure were determined.

The effects of principal stress ratio on brittle crack statistics were studied for homogeneous arrays of regular hexagons, having grain boundary strengths corresponding to an extreme-value distribution. In a numerical model, the cracks were simulated by dislocation pairs, chosen to satisfy the stress-free conditions on each cracked grain segment. Cracking was assumed to occur in the grain boundary with the lowest strength relative to the local stress or stress intensity factor on it due to the applied stress acting through the current crack pattern. An analytic approximation was developed, based on the density of grains cracked so far.

and the probability that they would aggregate into a crack of critical length under the current applied stress.

For a typical strength distribution, the stress at first cracking rises by 50% in going from biaxial to uniaxial applied stress. The maximum stress shows less size effect than predicted from extreme-value statistics, and a somewhat smaller rise in strength in going from biaxial to uniaxial stress. Crack closure and friction begin at a compressive stress of about half the applied tensile stress.

The problem of calculating the progress of micro-cracking in brittle materials towards the configuration giving maximum load, by repeated stress analysis of the developing micro-crack distribution, had been treated initially by considering grain boundary cracking in a two-dimensional array of regular hexagon grains embedded within an infinite body. Since brittle materials often fracture by the propagation of surface cracks, the numerical model was extended, using near surface dislocation dipoles, to study the effects on brittle crack statistics of surface or near surface initiated fracture.

Part sizes up to 1000 grain segments were studied using the numerical model for two different variabilities. It was found that the maximum strengths for surface initiated fracture are 10-20%, depending on orientation and variability, below those for embedded fracture. The relatively small drop in maximum strengths suggest that the statistical treatment of brittle materials is somewhat independent of whether fracture is initiated in the bulk or at the surface of the material as long as the relevant distribution of grain boundary strengths is used.

The method of determining the flaw density distributions of brittle materials from hardness indentation was summarized. The method, developed earlier in this project, neglected the interfacial friction between the indenter and the specimen surface. Thus, the apparent strength calculated was too high. It was suggested that the effect of friction could be included in the analysis by modifying the stress distribution function.

A plane strain cylindrical indenter was proposed for studying sub-surface flaws. Such an indenter gives no stress on the specimen surface and only compressive stress in the interior. Friction again influences the location of maximum stress.

The possibility of determining strength distributions from acoustic emission was studied. Acoustic emissions were used to obtain the statistical parameters that govern crack initiation in grain boundaries, idealized as an extreme value distribution of the third asymptotic kind. It is found that polishing significantly reduces the amount of acoustic activity as well as increasing the value of the statistical parameter m.

A flaw detection technique must be capable of detecting cracks of magnitude which are deemed critical, typically with openings between 0.02μm and 0.10μm depending on the material. The possibility of using the scattering of light from cracks was explored by dark field viewing of pre-cracked glass test specimens. Cracks with openings of about 0.10μm and greater have been observed. Therefore, until scattered intensities can be increased or detection methods improved, proof testing must be used to increased brittle structure reliability.

L. RESULTANT PUBLICATIONS AND THESES:

L.1. Publications

1. R. M. Cannon, "Impurity Segregation on Mobility of Grain Boundaries in Ceramics", presented at Gordon Research Conference on Solid State Studies in Ceramics, Wolfeboro, New Hampshire, August, 1975.

2. R. M. Cannon, M. F. Yan and H. K. Bowen, "Substructure Formation During Halide Processing", in Proceedings of the Fifth Conference on Infrared Laser Window Materials, eds., C. R. Andrews and C. L. Strecker, ARPA, February, 1976.

3. R. M. Cannon, et al., "Fabrication and Properties of Laser Window Materials", in Laser Induced Damage in Optical Materials:1976, NBS Special Publication 462, ed., A. J. Glass and A. H. Guenther, December, 1976.

4. F. A. McClintock and H. J. Mayson, "Principal Stress Effect on Brittle Crack Statistics", in The Effects of Voids on Material Deformation, Appl. Mech. Div. Vol. 16, ed., S. C. Cowin and M. M. Carroll, A.S.M.E., New York, 1976, 31-45.

5. M. F. Yan, R. M. Cannon and H. K. Bowen, "Grain Boundary Migration in Ceramics", in Ceramic Microstructures-76, ed., R. M. Fulrath and J. A. Pask, Westview Press, Boulder, Colorado, 1977.

6. R.M. Cannon, "Boundary Migration and Grain Growth: Effects of Solutes, Space charges, Pores, and Particles, presented at Gordon Research Conference on Solid State Studies in Ceramics, Tilton, New Hampshire, August 1977.

L.2. Theses

1. M. F. Yan, "Grain Boundary Mobility of KCl", Sc.D., Materials Science and Engineering, February, 1976.

2. A. M. Glaeser, "Microstructure Development in CaF_2", S.B., Materials Science and Engineering, June, 1976.

3. H. J. Mayson, "Brittle Crack Statistics and the Detection of Flaws", S.M. Mechanical Engineering, August, 1976.

4. W.M. Sherry, "The Deformation Behavior of Single Crystal Calcium Floride, PhD, Materials Science and Engineering, expected February, 1978, (partially supported).